2022

Dynamic characterization of multi-scale analytes by real time interferometric imaging

https://hdl.handle.net/2144/44707

Boston University

BOSTON UNIVERSITY

COLLEGE OF ENGINEERING

Dissertation

DYNAMIC CHARACTERIZATION OF MULTI-SCALE ANALYTES BY REAL TIME INTERFEROMETRIC IMAGING

by

ELISA CHIODI

B.S., University of Milano-Bicocca, 2016
M.S., University of Milano-Bicocca, 2017

Submitted in partial fulfillment of the
requirements for the degree of
Doctor of Philosophy

2022

Approved by

First Reader

M. Selim Ünlü, PhD
Distinguished Professor of Engineering
Professor of Electrical and Computer Engineering
Professor of Materials Science and Engineering
Professor of Biomedical Engineering
Professor of Physics

Second Reader

Anna K. Swan, PhD
Associate Professor of Electrical and Computer Engineering
Associate Professor of Materials Science and Engineering
Associate Professor of Physics

Third Reader

Irving J. Bigio, PhD
Professor of Biomedical Engineering
Professor of Electrical and Computer Engineering
Professor of Physics
Professor of Medicine

Fourth Reader

Marcella Chiari, PhD
Research Director
Institute of Chemical Sciences and Technologies Giulio Natta (SCITEC)
National Research Council of Italy
Milan, Italy

Alla mia nonna Maria,
Mia luce di speranza anche nei giorni più bui.

Acknowledgments

This Ph.D. program has been one of the biggest adventures of my life. I will be forever grateful to everyone who has supported me throughout this journey. I would like to start by thanking Professor M. Selim Ünlü for being an amazing mentor, always present, always happy to entertain stimulating discussions, to give guidance and constructive criticism. Thank you for believing in me as a scientist and as a person, and for teaching me to always embrace curiosity.

Further, I would like to express my gratitude to my committee members, Professor Anna K. Swan, Professor Irving J. Bigio, and Dr. Marcella Chiari, for their invaluable advice and contribution to my work. Particularly, I would like to thank Dr. Marcella Chiari for her continuous mentorship and support, and for contributing to my personal growth as a researcher. I am also grateful to the whole SCITEC-CNR group, for the great collaborations we shared.

I am truly grateful to all the scientists that have worked alongside me in the OCN group. Thank you for helping me explore all the aspects of the fascinating research behind the IRIS. In particular, I would like to thank Dr. Allison Marn, for our teamwork, the productive discussions over coffee (hot or iced, but mostly iced), and the long days and nights spent in the lab. I would not have made it without you. I am also incredibly grateful to Dr. Fulya Ekiz Kanik, Dr. Nese Lortlar Ünlü, Dr. Ayca Yalcin Ozkumur, Matthew Geib, Dr. Negin Zaraee, Dr. Celalettin Yurdakul, Iris Celebi, Mete Aslan and Dr. Monireh Bakhshpour. Thank you for being there to help whenever I needed, and for being awesome colleagues and friends.

Outside of the scientific world, many other people have supported me on this journey. To my parents, Marzia and Stefano: thank you for being the best family I could ever ask for, for your endless love and care, and for all your material and psychological support. To my grandmother Luisa, thank you for calling me every week just to make sure I was doing well and to remind me to eat (especially my veggies). You are always in my heart and on my mind. To my dear aunt Monica, you are an amazing, sweet and loving soul. Thank you for all the messages, all the smiles you put on my face throughout these years. To all my aunts, uncles and cousins: I have felt every ounce of your love and support everyday, even when it was hard to get in touch.

I also feel so blessed and grateful for the extraordinary people that are my close friends. To my best friend Arianna, you are and will always be one of the most important people in my life. I am absolutely certain that you will be by my side on every crucial moment in my life, as you are now. Thank you for the four-hour phone calls and the flights you have boarded to see me, even if just for a few days. To Alessandra, Diego, Marzia: thank you for being with me through thick and thin, for constantly checking in on me, but most importantly for understanding that life can sometimes separate you from the people in your heart, but if you truly care you're never apart. To all of the amazing friends I made here in Boston, especially Valentina, Nadine, Cansu, Marjaneh and Michela: thank you for being an incredible support system, my home away from home. With your presence, I knew I was never alone on this side of the planet, and I feel so lucky to have you in my life.

And last but not least, I am so, so grateful to have my wonderful fiancé Jamir by my side. You are the most brilliant, charming, loving person I have ever met. You inspire me everyday, and I could always feel your love and support, even when we were an ocean apart. Meeting you has changed my life, for the better, and I cannot wait to see what the future has in store for us.

On to the next adventure!

Eli

DYNAMIC CHARACTERIZATION OF MULTI-SCALE ANALYTES BY REAL TIME INTERFEROMETRIC IMAGING

ELISA CHIODI

Boston University, College of Engineering, 2022

Major Professor: M. Selim Ünlü, PhD
Distinguished Professor of Engineering
Professor of Electrical and Computer Engineering
Professor of Materials Science and Engineering
Professor of Biomedical Engineering
Professor of Physics

ABSTRACT

In the past decade, the field of biosensing has experienced an incredible pace of development, due to the compelling need for accurate and reliable tools for characterization of biomolecular kinetics. Specifically, label-free kinetic measurements are the most direct method for studying molecular binding, for example to establish the efficacy of drug-receptor interactions. For this reason, researchers in the pharmaceutical industry rely heavily on label-free detection for drug and antibody screening. Meanwhile, in the biosafety industry and healthcare, there is great demand for screening tools that can target biothreats, in order to accurately recognize the presence of toxins and pathogens with high sensitivity in diverse samples, such as bodily fluids, food and drinking water. This research topic has become particularly relevant during the recent pandemic, where vaccine development was carried out side by side with quantification and characterization of single viral particles. Here, we introduce a versatile biosensing platform capable of characterizing virtually any type of target compound, down to the single molecule level. For this work, we have improved the Interferometric Reflectance Imaging Sensor (IRIS) to perform accurate measurements of the binding kinetics of analytes ranging in molecular weight from less than 1kDa (small molecules) to more than 1MDa (biological nanoparticles). For the first time, we demonstrate multiplexed kinetic binding characterization of small molecules to surface immobilized antibody probes, as well as detection and phenotyping of large and complex analytes, on the same platform.

The IRIS platform utilizes the optical interference signal produced by thinly layered substrates in order to precisely measure the thickness of a transparent film atop a silicon chip. In the context of this work, dynamic characterization of a wide range of biomolecular and nanoparticle targets was made possible by a multidimensional optimization, in order to improve both the sensitivity and the dynamic range of the instrument. Analysis of low molecular weight compounds required a significant increase in signal to noise ratio, which was achieved through averaging, as well as complete elimination of background solution effects ('bulk effect'). Additionally, the best surface chemistry for each application was identified by a new technique which consists of immobilizing capture probes on a multiplexed array of active polymers functionalized on the same sensor surface, allowing for simultaneous side-by-side comparison of their performance. Surface chemistry plays a huge role in kinetic measurements, in terms of probe functionality, steric hindrance, charge distribution and diffusion effects.

Finally, imaging optics, illumination wavelength, and thickness of the silicon dioxide film were optimized to perform detection and phenotyping of large analytes, such as extracellular vesicles (EVs) and antibody-conjugated gold nanoparticles (mAb-GNPs). Results obtained from numerical simulations allowed for selection of the best experimental parameters for each application. Experimentally, mAb-GNPs were utilized to produce a real-time sandwich lateral flow assay. In this context, we demonstrated how the improved IRIS platform can bridge the gap between single-particle detection ('digital' configuration) and bulk reflectance measurements ('analog' configuration), creating a new 'hybrid' system (h-IRIS), which only requires minimal hardware adjustments to easily switch from one modality to the other. This brought a substantial improvement in sensitivity, improving the limit of detection by three orders of magnitude and enabling single-molecule level measurements. Finally, future system optimization ideas are presented to achieve even higher accuracy and further extend the range of target analytes.

Contents

List of Tables

List of Figures

List of Abbreviations

BBB	....	Blood-brain barrier
BLI	....	Bio-Lateral Interferometry
BNP	....	Biological nanoparticle
BP	....	Biological particle
BSA	....	Bovine serum albumin
CM	....	Carboxymethyl
CMOS	....	Complementary metal-oxide-semiconductor
DBCO	....	Dibenzocyclooctyne group
DMA	....	N, N-dimethylacrylamide
DMSO	....	Dymethyl sulfoxide
ELISA	....	Enzyme-linked immunoassay
EPDMA	....	ethylene propylene diene monomer
EV	....	Extracellular vesicles
FOV	....	Field of view
FPS	....	Frames per second
FWC	....	Full well capacity
GNP	....	Gold nanoparticle
IgG	....	Immunoglobulin
HBV	....	Hepatitis B viral infection
h-IRIS	....	Hybrid Interferometric Reflectance Imaging Sensor
IRIS	....	Interferometric Reflectance Imaging Sensor
LED	....	Light-emitting diode
LFA	....	Lateral Flow Assay
LMW	....	Low molecular weight
LOD	....	Limit of detection
mAb-GNP	....	Monoclonal antibody-gold nanoparticle complex
MAPS	....	3-(Trimethoxysilyl)propyl methacrylate
MW	....	Molecular weight
NA	....	Numerical aperture

NAS	....	N-Acryloyloxysuccinimide
OPD	....	Optical path difference
PBS	....	Phosphate buffer saline
PE	....	Plasmon excitation
POC	....	Point-of-care
PPM	....	Post-polymerization modification
PSF	....	Point spread function
SAV	....	Streptavidin
SEV	....	Small extracellular vesicle
SMs	....	Small molecules
SNR	....	Signal-to-noise ratio
SPR	....	Surface Plasmon Resonance
SPRi	....	Surface Plasmon Resonance Imaging
Std	....	Standard
SVM	....	Silicon Valley Microelectronics
TIR	....	Total internal reflection

Chapter 1

Introduction

1.1 Measuring molecular affinity: the importance of kinetics

Molecular interactions shape the world around us. In nature, almost all biological functions involved in the process of life are regulated by interactions between molecules, primarily receptors, proteins, enzymes and nucleic acids. Petsko and Yates brilliantly summarized this concept as: *nothing happens in biology unless something binds to something else* (Petsko and Yates, 2011). Inside both prokaryotic and eukaryotic cells, molecular reactions are carried out in order to perform gene replication, protein synthesis, pathway signaling and regulation of immune responses (Friedl et al., 2005). All these processes are extremely diverse, in timescale, purpose and produced effect, and can sometimes involve more than one consecutive step, generating complex molecular systems. In general, biomolecular interactions span a broad range of timescales, varying over more than ten orders of magnitude (Clerc et al., 2021; Elber, 2005). Very fast molecular reactions include, for example, the R to T transition of hemoglobin (Elber, 2005), which is in the order of microseconds, while the dissociation of high affinity compounds is a slow process, lasting for multiple hours.

In order to understand and investigate the complex working principle of the human body, it is therefore essential to study it at the molecular level. Generally, a system which is capable of measuring the strength of a molecular reaction is referred to as a *biosensor*. Biosensors are incredibly valuable in the field of molecular development, and a large deal of effort has been devoted in the past decade to develop robust, reliable and highly sensitive instruments for biochemical investigation.

Biosensors are usually composed of a *bioreceptor*, or *ligand*, which is the recognition element responsible for interacting with the target molecule (the *analyte*), and a transduction mechanism, which is a property of the system that can be monitored and is altered when the reaction takes place, enabling the measurement of binding events. For the sake of this discussion, the focus will be on optical biosensors, where an optical property of the transducer, such as its refractive index, is modified by the occurrence of the binding reaction, and the biorecognition element is immobilized on the surface of the sensor (Peltomaa et al., 2018). In the field of optical biosensing, some technologies have been developed which succeed in visualizing molecular reactions in real-time, providing an estimation of how fast and how strongly the target analyte and the ligand interact with each other. These real-time measurements are usually referred to as *kinetic* measurements, since their goal is to assess the kinetic, or dynamic, parameters of an interaction.

The strength of a molecular reaction is defined as *molecular affinity*, and its determination provides an estimation of how likely the two molecules are to interact with each other, as well as how strongly they resist being separated. As a matter of fact, the kinetics of a reaction is measured by testing the behavior of the molecules in two consecutive phases: the *association* phase, that is, the two molecules are introduced to each other and are allowed to react and bind; and the *dissociation* phase, where one of the two agents is removed from the solution and the rate at which they 'dissociate' or 'debind' from each other is measured. As mentioned above, the molecule that is introduced and then removed is referred to as the analyte, while its binding partner, the bioreceptor, is the ligand. The rate of association, or binding, is defined as the *on-rate* (k_{ON}) of the reaction, while the dissociation rate is referred to as the *off-rate* (k_{OFF}). If the two agents A and B interact in a 1:1 fashion, the reaction can be described by the simple symbolic equation:

$$A + B \underset{k_{OFF}}{\overset{k_{ON}}{\rightleftharpoons}} AB \tag{1.1}$$

Where A is the analyte and B the ligand. In order to describe the kinetics of the reaction, differential equations can be written which define the rate of formation of the complex AB, as well as the dissociation after analyte A is removed:

$$\begin{cases} \dfrac{d[AB]}{dt} = k_{ON}[A][B] - k_{OFF}[AB] & t_0 < t < t_1 \\ \dfrac{d[AB]}{dt} = -k_{OFF}[A][B] & t > t_1 \end{cases} \tag{1.2}$$

Where $[A]$, $[B]$, $[AB]$ are the molar concentrations of the two molecules separately and as a complex, respectively, t_0 is the injection time of the analyte and t_1 is the start time of the wash, that is, the removal of the free analyte. In order for the reaction to be detected on a sensor, the binding of the analyte molecules to the ligands needs to generate a signal. The differential equations above can therefore be written as a signal increment in time:

$$\frac{dS}{dt} = k_{ON}C(S_{max} - S) - k_{OFF}S \tag{1.3}$$

Where C is the molar concentration of the analyte, which is assumed to be constant in time, and S_{max} is the maximum reachable signal, defined as the signal measured when all ligand binding sites are occupied. Reactions are usually allowed to reach equilibrium during the association phase, the condition where the number of analyte molecules binding and debinding is equal, creating a steady state. This leads to the following analytical solution of Equation 1.2:

$$S(t) = \begin{cases} 0 & 0 < t < t_0 \\ S_{eq}(1 - e^{-(k_{ON}C - k_{OFF})(t-t_0)}) & t_0 < t < t_1 \\ S_{eq}(e^{-k_{OFF}(t-t_1)}) & t > t_1 \end{cases} \tag{1.4}$$

This is the referred to as the Langmuir thermodynamic model, and solving for S_{eq} leads to an isotherm of the form:

$$S_{eq} = \frac{S_{max}}{1 + \frac{K_D}{C}} \tag{1.5}$$

where $K_D = k_{OFF}/k_{ON}$ represents the dissociation constant, also defined as the *equilibrium constant*. Most kinetic sensors consider K_D as the ultimate value to be measured in order to establish the affinity of the reaction.

Unless otherwise specified, this is the model that will be utilized to fit most binding data presented in this dissertation. As mentioned above, it describes a 1:1 interaction, assuming one analyte molecule should only interact with one ligand molecule. Other types of interactions include bivalency (2:1) and multivalency (N:1) (Schasfoort, 2017).

As mentioned above, most researchers believe the equilibrium constant K_D to be a good description of the affinity of a reaction, thus not necessarily requiring kinetic measurements. Indeed, by measuring the equilibrium binding signal reached at several analyte concentrations, K_D can be mapped as an isotherm (Equation 1.5). That can be true in some cases, however, end-point measurements, or equilibrium measurements, provide a 'frozen' view of the molecular complex, ignoring the dynamic nature of the association-dissociation reaction. For this reason, kinetic measurements generally have significant advantages over equilibrium measurements. For example, if the reaction rate is not limited by diffusion or analyte molecules' availability, measuring a single binding curve at one analyte concentration point is enough to establish association and dissociation rates, from which K_D can be derived. This is beneficial in terms of sample preservation, as well as rapid generation of results, leading to cost- and time-effective experiments.

Furthermore, some reactions can be characterized by complex dynamics, such as cooperative binding (De Lean and Rodbard, 1979), and biphasic binding (Needham, 2019; Karanicolas and Brooks, 2004) which are difficult to identify when performing end point measurements. Finally, most equilibrium measurements such as fluorescence microarrays or enzyme-linked immunoassays (ELISA), require labeling of the target molecules, a procedure that can be challenging as it will be described in the following section.

1.1.1 Probing in the dark: label-free measurements

Label-free detection is the concept of detecting the presence of a microscopic object on the surface of a sensor without the aid of a label. The *target* compound, usually a molecule or a biological nanoparticle, is captured by the surface through affinity interactions. In order to achieve that, the sensor's surface is functionalized with specific biorecognizing elements, which in this discussion will be referred to as *probes* or, as mentioned above, *ligands.* Probes are generally antibodies, but sometimes oligonucleotides, receptors or enzymes are used. Label-free detection is the least artificial way of characterizing a molecular reaction *in vitro*, due to the absence of a third interacting element and the non invasive sensing method.

On the other hand, labeled methods are well-established in the field of biomedical discovery, due to the high sensitivity and specificity they provide (Cretich et al., 2011; Epstein et al., 2002; Camarca et al., 2021). Particularly, fluorescent microarrays enable multiplexed detection and quantification of molecular contaminants, DNA mutations, as well as single biological particles counting and phenotyping (Gagni et al., 2016). Fluorescence is a fascinating biophysical concept that relies on narrowband light adsorption and re-emission by chemical compounds that possess an excitable state. For decades, it has allowed researchers to 'shine a light in the dark', and detect the presence of biological phenomena that would otherwise be invisible to the human eye.

However, labeling is a cumbersome, challenging process which is usually low yield, and can sometimes lead to molecular denaturation or hindering of the analyte binding sites (Syahir et al., 2015). In most cases, the label is covalently attached to the target molecule by direct modification, which can cause structure distortion and loss in reactivity. As an alternative to modification, secondary fluorescent antibodies are often utilized for post-reaction labeling. This method is more straightforward, but it requires two subsequent incubations of the sensor - first with the analyte and then with the label.

Moreover, the labeling antibody needs to target a binding site on the analyte molecule that remains available after the reaction with the probe, and that is reachable despite the steric hindrance caused by the presence of the probe and the surface. For example, in the case of ELISA sandwich assays, antibody pairs are specifically developed to target two different binding sites positioned at two opposite sides on the analyte molecule. Obviously, this is particularly challenging for small molecule targets, which often have only one binding site, or - if more than one is present - they are all very close to each other and therefore made unavailable by steric hindrance.

All these issues delineate the motivation for the development of biocharacterization methods that do not require labeling. In biomedical research, there is a crucial need for easy to use, versatile sensors that do not require special treatments of the molecules involved and that produce reliable characterization data. This dissertation will describe the development of a system which enables the characterization of most biological samples, with few or no purification and/or modification steps required, down to the single particle digital counting level. The hereby discussed platform has the power to establish itself as a better alternative to both labeled and unlabeled characterization methods currently available in the field.

1.2 Properties of multi-scale analytes

The main objective of this dissertation was to develop a versatile platform that can provide label-free, accurate kinetic binding data, enabling real-time characterization of highly diverse analytes, varying both in size and biophysical properties.

In the following Sections, we will give a brief overview of the most important characteristics of the studied molecules and nanoparticles, in order to highlight both the challenges that we had to overcome to achieve accurate affinity measurements of this wide range of targets, as well as the impact of our work on the field of biomolecular development.

1.2.1 Small molecules and drug development

Small molecules (SMs) are defined as the chemical compounds with a molecular weight below 1kDa (Fechner et al., 2014; Peltomaa et al., 2018). Due to their low molecular weight, SMs have recently gained a huge popularity in the drug development field, because they can easily penetrate the cellular membrane and produce their effect. In 2019, 73% of all approved drugs by the FDA belonged to the category of SMs (Mullard, 2020). As an example of their relevance, is has been demonstrated that SMs can easily penetrate the blood-brain barrier (BBB), which is the interface between the vascular system and the brain, and represents a significant obstacle in delivering drugs and medicines to the brain (Eyal et al., 2009). Its permeability is extremely low, and only a few chemicals can easily cross it through ion channels. However, it has been shown that small lipophilic molecules ($MW < 500Da$) can be transported across the BBB thanks to passive diffusion across the membrane of brain cells (Wong et al., 2013). This has been an invaluable discovery for research in brain cancer treatment, and other brain-related diseases.

One other fundamental application of SMs characterization is toxin detection. More than 99% of all toxins in nature belong to the category of SMs (Wishart et al., 2015; Peltomaa et al., 2018), and these compounds are harmful to humans. Of particular relevance are mycotoxins, toxic compounds produced by molds or fungi, especially from the species *Aspergillus*, *Fusarium*, and *Penicillium*, that are most commonly found in corn and other crops (Granados-Chinchilla et al., 2018). Mycotoxin intoxication has been shown to have an impact on the formation of esophageal cancer (Sydenham et al., 1990; Chu and Li, 1994). Consequently, having a method of efficient identification of mycotoxin presence in organic products is absolutely critical for the food industry, especially in the quality control phase.

However, despite the huge impact that SMs have in various research and industry fields, there is still a lack of consensus on a good detection and characterization method. As a matter of fact, due to their low molecular weight, SMs are particularly challenging to detect in a label-free manner, as molecular binding of tiny-sized compounds produces a small optical response on label-free transducers. One of the most widely used sensors for SMs research is Surface Plasmon Resonance (SPR). SPR is highly sensitive, and it provides the ability to detect and phenotype SMs. However, its sensitivity to environmental conditions, particularly refractive index changes of the surrounding solution, makes it non ideal for SM measurements. SMs are indeed mostly insoluble in aqueous buffers, requiring in most cases the addition of a powerful organic solvent which considerably raises the refractive index of the environment surrounding the surface. This, combined with the dense and thick surface chemistry that SPR requires, reduces its ability to provide reliable kinetic data for SMs binding. This topic will be further discussed in Section 2.4.

Labeling small molecules with either a fluorescent tag (Joubert et al., 2013; Mizukami et al., 2014) or a metallic nanoparticle (Cao et al., 2018; Lin et al., 2007) makes them easier to detect. However, as explained above in Section 1.1.1, labeled techniques have multiple issues, one of the most relevant being that they lack kinetic capabilities. Furthermore, efficient labeling of SMs can be challenging: sandwich assays with a secondary fluorescent antibody are virtually impossible, since SMs usually possess a single binding site; modification with fluorescent chemical groups is an invasive process that can cause changes in the molecule's functionality, especially if the tag is similar or larger in size (Fechner et al., 2014). Label-free techniques are, therefore, preferred when it comes to evaluating the kinetic behavior of drugs, toxins, and small analytes in general. In this dissertation, we have explored SMs binding kinetics on the IRIS sensor, successfully producing repeatable binding data for a small molecule toxin (fumonisin, MW$\approx$722 Da) and for biotin, an essential SM protein (MW$\approx$244 Da) utilized in combination with its binding partner, streptavidin, in many surface chemistry applications due to the almost-covalent nature of their interaction (Wong et al., 1999).

1.2.2 Biological nanoparticles: Extracellular Vesicles (EVs)

Extracellular Vesicles (EVs) are lipid-bilayer delimited particles that are produced inside cells in the human body, and are subsequently released into the bloodstream by various mechanisms, including fusion of endosomes with the cell membrane (Lötvall et al., 2014). All EVs are incapable of replicating, vary in size in the 30nm-1μm range and can contain variable amount of biological material of diagnostic relevance. For example, *exosomes* are small EVs (30-150nm) of endosomic origin which have been shown to carry information both on their surface and inside their cargo which allows to discern whether the cell that originated them is a healthy or a cancer cell. As a matter of fact, it has recently been demonstrated that exosomes can be utilized as biomarkers for various types of cancer, including lung (Sandfeld-Paulsen et al., 2016b) and prostate (Nawaz et al., 2014) cancer. For all these reasons, the interest in EVs as biomarkers has vertiginously increased in the past few years, and development of platforms that provide extensive analysis of EVs samples has seen a steady upsurge, both in research and in the industry.

Fluorescence is still the most common method for analysis of EVs samples, as it is sensitive, robust and can provide high marker specificity (Wang et al., 2020). However, label-free methods have also been applied to EVs analysis, including SPR and SPR imaging (SPRi) (Picciolini et al., 2018). Here, we will discuss the results of detection, characterization and phenotyping of EVs samples with the IRIS system, which - in two different configurations - provides both measurements of analog real-time binding of EVs, as well as single particle counting.

1.2.3 Antibody- gold nanoparticle complexes (mAb-GNP) for lateral flow assays

Lateral Flow Assays (LFAs) are cellulose-based point of care (POC) diagnostic tools that are widely utilized for detection of infectious diseases, toxins, food contaminants and other biothreats (Liu et al., 2021). These tests have gained a huge popularity in the past fifty years due to the many advantages over other techniques: LFAs are rapid, cheap (down to <1$ per test) and robust, as well as not necessitating any technical expertise on the tester's side. They utilize simple colored lines - a 'control' line and a 'test' line - to readily provide the information on the presence or absence of a certain pathogen or biomarker target in human fluids.

LFA-based devices are composed of a nitrocellulose membrane, a conjugate pad, for sample intake and an absorbent pad, for sample delivery to the test line. The test line utilizes highly specific antibodies and gold nanoparticles in order to create a control colored band, as well as a test/positive band, while the sample flows through the line. In the past two years, LFAs have become incredibly popular due to their huge impact in SARS-CoV-19 diagnosis. Most self-administrable, at-home test kits are based on LFA technology. However, LFAs have been around for decades, and the most popular and readily available example are pregnancy tests.

Investigating the reaction kinetics of LFAs is a crucial step in the development of successful assays and is also essential for obtaining the highest possible sensitivity (Liu et al., 2021). Right now, the sensitivity of LFAs is in the μM range in terms of target concentration, while laboratory tests such as ELISA assays or PCR-based tests can detect concentrations down to pM-fM range. Thus, given the great advantages of LFAs, which led to their quick rise in popularity, it has become more and more crucial to improve their sensitivity as well as the specificity of the involved antibody-gold nanoparticle complexes (mAb-GNP). In the final section of Chapter 4, we will introduce a method to analyze the kinetics of mAb-GNS complexes, while also performing single particle imaging and counting, on a novel, hybrid interferometric sensor.

1.3 Dissertation objectives and overview

In this work, we aim to describe a versatile biosensing platform for the complete analysis of highly diverse biochemical samples. The dissertation is divided into three main chapters. In Chapter two, we describe the working principle of the Interferometric Reflectance Imaging Sensor (IRIS); first, we distinguish two main applications of the platform: kinetic analysis of biomolecules using the *analog* configuration of the sensor, and single nanoparticle detection and phenotyping by switching to the *digital* configuration, or SP-IRIS. After reviewing the theoretical principles and the physical requirements of each setup, we then begin to describe the hardware modifications needed to create a hybrid system (h-IRIS). In Chapter 3, we focus on system performance optimization. We discuss noise factors, the impact of illumination uni-

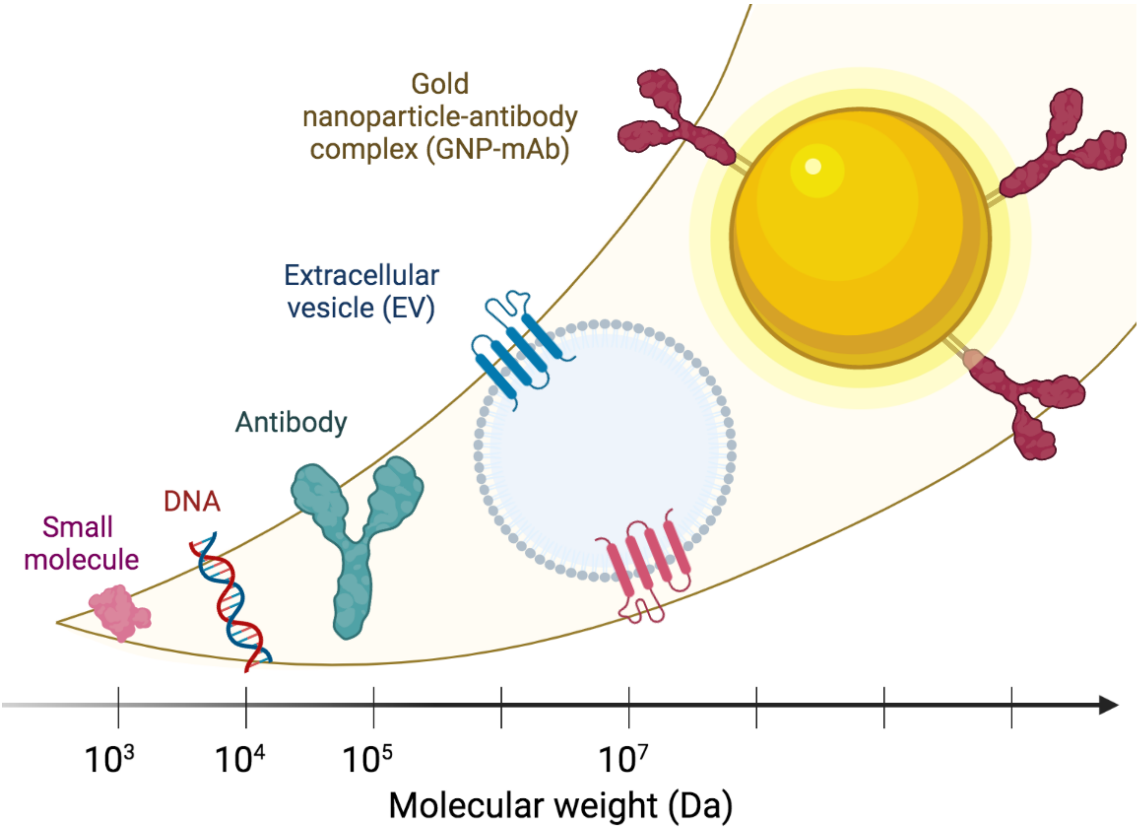

Figure 1·1: Multi-scale analytes studied on the Interferometric Reflectance Imaging Sensor (IRIS)

formity and potential optical improvements, solution effects such as the *bulk shift*, and advantages and limitations of various surface chemistry methods. We also show some theoretical results on wavelength optimization, with simulations for nanoparticle analysis both at the analog and digital level. Finally, in Chapter 4 we show several experimental results, where we successfully demonstrate characterization of heterogeneous samples ranging from small molecules to extracellular vesicles and gold nanoparticles-antibody complexes on the h-IRIS system.

1.4 Published work

Most of the work presented in this dissertation has been published in academic journals. The small molecule characterization work discussed in Chapter 4 has been published in ACS Omega (Chiodi et al., 2020a), while a paper on kinetic analysis of extracellular vesicles was published in Sensors (Chiodi et al., 2021a); such work is also presented in Chapter 4.

The work on bulk effect elimination discussed in Chapter 3 has been published in ACS Omega (Marn et al., 2021a). We have recently published two reviews in the journal Polymers that focus on the impact of surface chemistry on label-free measurements (Chiodi et al., 2021c; Chiodi et al., 2022), while a paper that introduces an innovative method for surface chemistry optimization has been published in Analytical and Bioanalytical Chemistry (Chiodi et al., 2020b); we will discuss such method in Chapter 3, as a part of system optimization. Finally, we are currently working on a paper where we introduce the hybrid h-IRIS system.

During the past three years, we have published additional papers that I have contributed to as part of my doctoral work, which unfortunately did not find a place in this dissertation (Bakhshpour et al., 2022; Marn et al., 2021b; Brambilla et al., 2021; Chiodi et al., 2021b; Celebi et al., 2020).

Chapter 2

The Interferometric Reflectance Imaging Sensor (IRIS)

2.1 Analog measurements: sensor's working principle and current performance

The Interferometric Reflectance Imaging Sensor (IRIS) is an interferometry-based biosensor for the real time detection and characterization of biomaterial accumulation. In its *analog* configuration, it exploits the simple concept of thin-film interference, the same physical principle that allows the human eye to see colorful reflections in soap bubbles, in order to achieve highly sensitive detection of biomolecular binding. Furthermore, years of research have demonstrated how interference can also be utilized to enhance the scattering signal from single particles, leading to a different application of the sensor, its *digital* or Single-Particle IRIS configuration (SP-IRIS), which will be described in the following section (Section 2.2). Both IRIS-based platforms have been widely described in the literature, and applied to the detection of numerous biologically relevant samples - from proteins, antibodies, and oligonucleotides, to single viral particles and bacteria.

Practically, the optical configuration of the IRIS system is a simple reflectance-based common-path interferometer, and the physical sensor chip is a silicon substrate with a thermally-grown silicon dioxide layer on top (Si/SiO$_2$). A set of four generic RGYB light emitting diodes (LEDs) is used for illumination, in a custom configuration; depending on the application, light from a single or multiple LEDs can be employed. The partially coherent light is further randomized by an integrating sphere (for example, ThorLabs IS236A-4), then collected and collimated by illumination optics. The optical configuration of the illumination arm of the interferometer, as well as the objective magnification and the thickness of the oxide layer, all depend on the specific application chosen, either analog or digital detection. These differences will be discussed more in details in Section 2.3. The analog configuration of the IRIS uses a critical illumination setup, where the source light is collected and collimated by an achromatic doublet with a focal length (f) of 50mm (ThorLabs AC254-050-A-ML), then focused on the sample plane.

An adjustable-diameter aperture is placed at the output of the integrating sphere to eliminate light at extraneous angles from entering the system. The collimated light is then shined on the chip, through a beam splitter (ThorLabs CCM1-BS013) and an infinity-corrected objective (Nikon, various models). Light is reflected back from the surface of the chip, and is subsequently collected and imaged through the same objective, beam splitter and a tube lens onto a CMOS camera (FLIR BlackFly BFS-U3-17S7M). A simplified scheme of the interferometer is shown in Figure 2·1.

Critical illumination is the simplest possible illumination scheme, and results in the source being imaged at the camera level. However, for analog measurements, low numerical aperture objectives are employed in order to approximate to normal illumination and collection, and therefore the illumination across the image plane remains sufficiently uniform. This will not be true for digital, single-particle counting measurements, where a more sophisticated illumination setup is necessary, as described later in Section 2.2.

For flow-based, real-time kinetic measurements, the Si/SiO_2 substrate is illuminated from the top through a microfluidic chamber, formed by sandwiching the chip

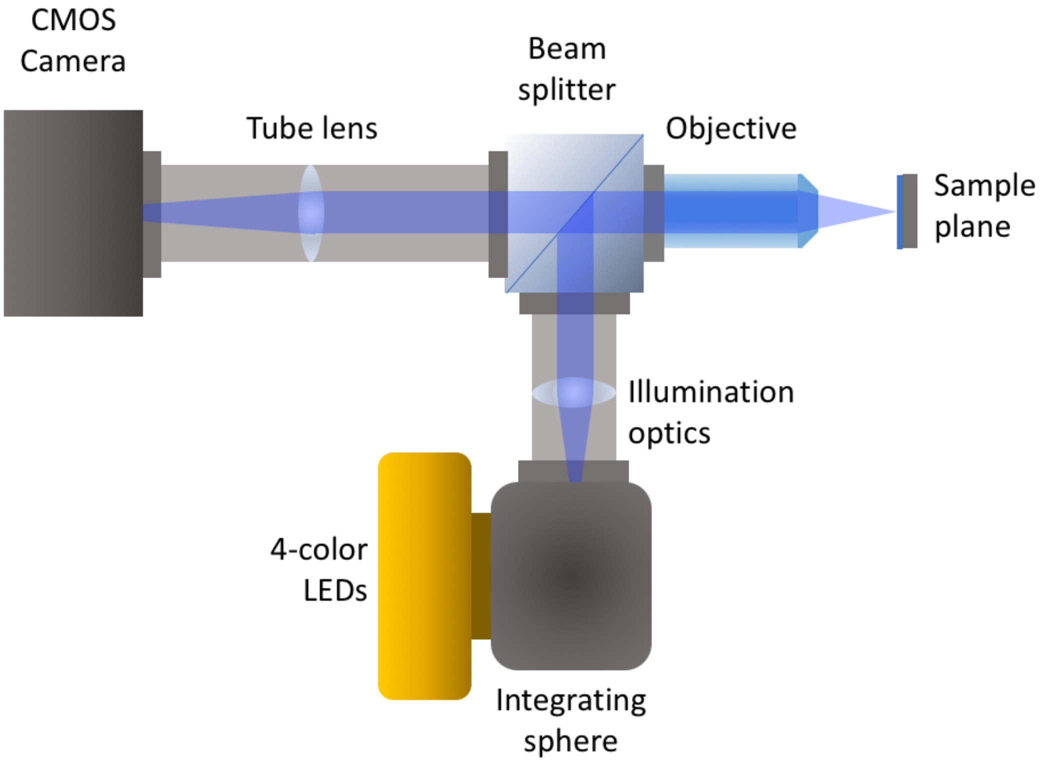

Figure 2·1: A simplified scheme of the optical configuration of the IRIS platform. The configuration of the illumination arm changes based on the specific application.

with a PSA-coated gasket (Grace Bio Labs) and an AR-coated glass slide (Abrisa technologies, inc.). The chip has laser-drilled inlet and outlet holes, therefore allowing solutions to be flowed across its surface (Figure 2·2). The liquid is driven through the system by a microfluidic setup composed of a programmable precision syringe pump (Hamilton PSD/4 54848-01) coupled with an eight way ceramic valve (Hamilton 59943-01). The microfluidic scheme is represented in Figure 2·3. The 130-μm thick microfluidic chamber allows for high flow rates and reduction of mass transport effect.

The light reflecting from the Si-SiO$_2$ and the SiO$_2$-immersion medium interface will interfere to produce a spectral reflectance curve that is dependent on the OPD (optical path difference) between the two interfaces. The reflectance from this dual-

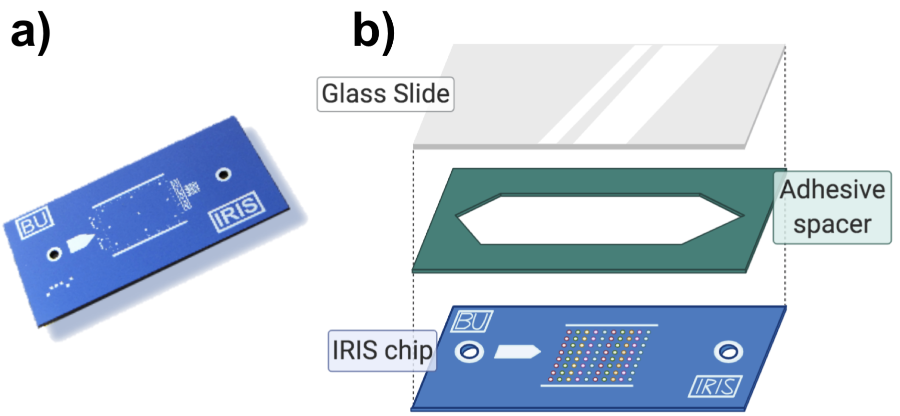

Figure 2·2: (a) A photo of the Si/SiO_2 IRIS chip and (b) a scheme of the fluidic cartridge used for the experiments.

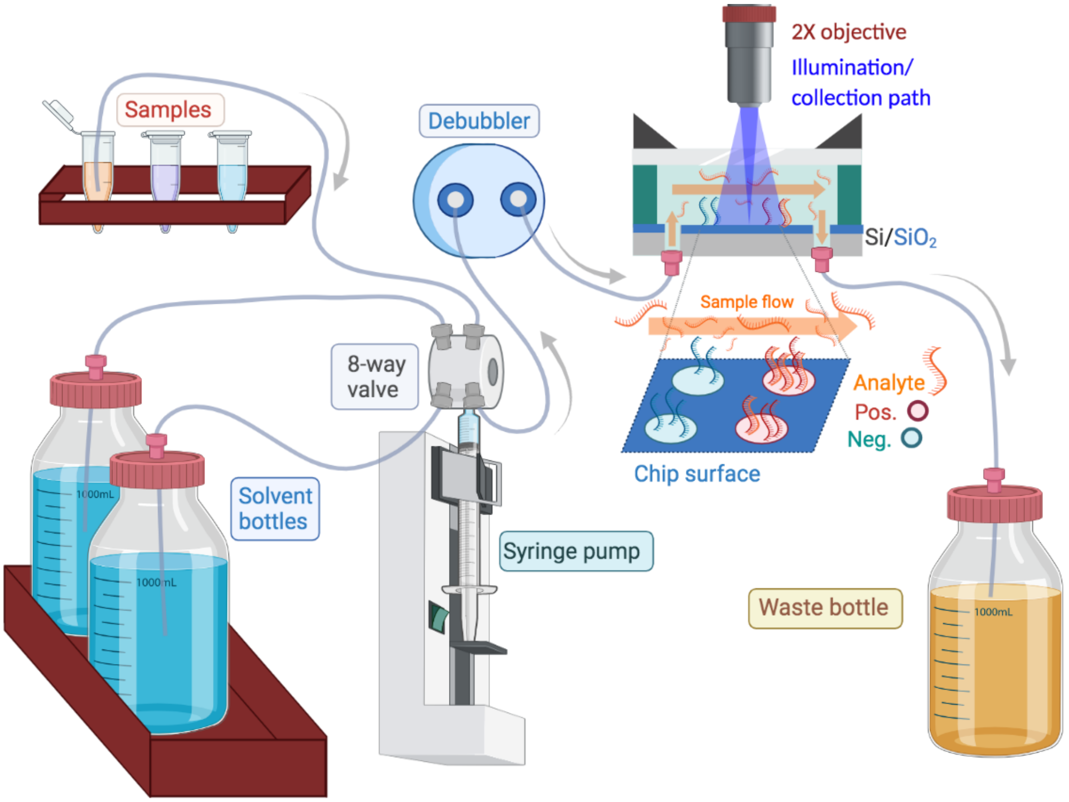

Figure 2·3: A graphical scheme of the microfluidic system employed on the IRIS instrument.

layer substrate can be measured on the IRIS at discrete wavelengths. Accumulation of biomass on the sensor surface will increase the effective thickness of the oxide layer and therefore alter the spectral reflectance. In order to maximize the signal due to molecular binding, the thickness of the oxide layer and the illumination wavelength need to be engineered so that constructive interference is obtained, and signal change is maximized for changes in the OPD. For our measurements in pure analog configuration, the thickness of the oxide was optimized at $d(\mathrm{SiO_2}) = 110\mathrm{nm}$, while the wavelength was $\lambda = 452\mathrm{nm}$ (blue).

The reflectance equation is obtained by simplifying Fresnel equations for reflection and transmission of light in layered substrates. Briefly, when light travels from a medium with a refractive index n_1 to a second medium n_2, part of the radiation is reflected and part is transmitted; the reflected fraction depends on the wavelength of light, the incidence angle and the optical properties of the two media. The reflected intensity is referred to as the reflectance R_s for s-polarized light and R_p for p-polarized light, and its derivation is described by the equations below based on the the reflection coefficients r_s (s-polarized) and r_p (p-polarized).

$$r_s(\lambda, \theta) = \frac{n_1(\lambda) cos\theta_i - n_2(\lambda) cos\theta_t}{n_1(\lambda) cos\theta_i + n_2(\lambda) cos\theta_t} \tag{2.1}$$

$$r_p(\lambda, \theta) = \frac{n_1(\lambda) cos\theta_t - n_2(\lambda) cos\theta_i}{n_1(\lambda) cos\theta_t + n_2(\lambda) cos\theta_i} \tag{2.2}$$

$$R_s(\lambda, \theta) = |r_s(\lambda, \theta)|^2 \tag{2.3}$$

$$R_p(\lambda, \theta) = |r_p(\lambda, \theta)|^2 \tag{2.4}$$

On the IRIS system, illumination can be approximated as normal, and therefore $\theta = 0$. Furthermore, incident radiation is unpolarized, reducing the effective reflectance to the average of the reflectance from both polarizations:

$$r(\lambda) = \frac{n_1(\lambda) - n_2(\lambda)}{n_1(\lambda) + n_2(\lambda)} \tag{2.5}$$

$$R(\lambda) = |r(\lambda)|^2 \tag{2.6}$$

Which then yields: (Sevenler and Ünlü, 2016):

$$R(\lambda, d) = |r^2| = \frac{{r_{12}}^2 + {r_{23}}^2 + 2r_{12}r_{23}\cos 2\phi}{1 + {r_{12}}^2{r_{23}}^2 + 2r_{12}r_{23}\cos 2\phi} \tag{2.7}$$

Where:

$$\phi = \frac{2\pi d}{\lambda} n_2 \tag{2.8}$$

$$r_{12} = \frac{n_1 - n_2}{n_1 + n_2}, \tag{2.9}$$

$$r_{23} = \frac{n_2 - n_3}{n_2 + n_3}, \tag{2.10}$$

The OPD is described by the phase difference ϕ, which changes in response to biomass accumulation (increase in d), as shown in Figure 2·4.

By acquiring the reflectance at four discrete wavelengths (center wavelengths of the RGYB LEDs: λ=452nm, 518nm, 595nm, 632nm) the values can be fitted to the reflectance equation. By assuming small, linear shifts in the reflectance curve due to biomass accumulation, it is possible to only acquire a four-color image of the chip at the beginning of the experiment, and afterwards utilize a single-color LED for acquisition. The four-color image is used to generate a lookup table, in order to correlate changes in reflectance for a single color to biomass density increments. This calibration step allows for conversion of reflectance values to mass density values

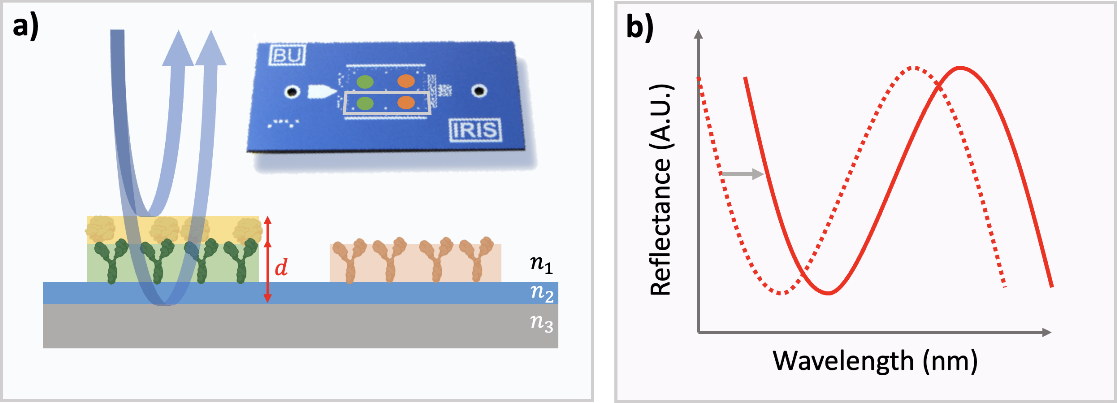

Figure 2·4: The working principle of the IRIS system. a) When biomass accumulates on the IRIS chip, the OPD d changes, causing a phase shift of the b) reflectance curve, producing constructive interference signal.

(expressed in pg/mm^2) (Sevenler and Ünlü, 2016).

On a side note, if the refractive index of the solution were to change (n_1), the phase would not change but the total measured reflectance would. More precisely, a change in n_1 would cause the reflectance curve to shrink, while a change in d would cause it to shift. In this case, the look-up table method would not work, and four color images would have to be acquired at each time point. Since changes in the refractive index of the solution usually correlate with small molecule characterization experiments, due to the need for high refractive index solvents to dissolve them, we have developed a method to remove such effect in practice by manipulating the LED wavelength. Such *bulk effect removal* technique will be described in Section 3.4.1.

The performance of the IRIS system should be determined based on the specific application. Here, the discussion will mostly focus on the analog configuration of the sensor, as most of the data shown in this dissertation were acquired in this modality. For analog measurements, the important parameter is the mass density sensitivity or *limit of detection* (LOD) of the system, which can be defined as the minimum measurable change in reflectance due to molecular binding. Currently, the sensitivity of the sensor in terms of the minimum measurable increment in mass density (mass per unit area) is LOD = 1pg/mm^2. This value can be improved further with various methods, both computational and physical, as described in Section 3.1.

2.2 Introduction to single particle (digital) detection

In the era of pandemics, accurate and highly sensitive detection of biological particles (BPs) such as viruses and bacteria is of crucial importance for pharmaceutical research as well as diagnostics (Kairdolf et al., 2017). Particularly, biological nanoparticles (BNPs) are a subset of BPs sized 10-100nm which includes viruses and small extracellular vesicles (SEVs). Label-free, scattering-based detection of single BNPs poses multiple challenges, due to their weakly scattering characteristics, the low refractive index contrast with the surrounding medium and the sub-wavelength spatial resolution limit imposed by the optical imaging system.

While pure scattering-based, dark-field methods for nanoparticle detection are limited in the size of particle they can measure due to the fact that the measured scattering signal scales with the sixth power of the particle size ($S \approx r^6$), on the SP-IRIS system, the detected intensity has a linear dependence on the induced scattered field, and the measured signal scales with the third power of the nanoparticle size ($S \approx r^3$), a huge improvement with respect to standard techniques.

More precisely, in the quasi-static dipole limit ($r << \lambda$: the nanoparticle size is much smaller than the wavelength) the far-field scattered field induced by illumination of a nanoparticle with polarizability tensor $\boldsymbol{\alpha}$ is expressed as (Novotny and Hecht, 2006):

$$\mathbf{E_s} = \frac{k_0^2}{\epsilon_0} \mathbf{G_s} \boldsymbol{\mu} \tag{2.11}$$

Where ϵ_0 is the vacuum dielectric constant, k_0 is the wavenumber in vacuum, $\mathbf{G_s}$

is the far-field dyadic point spread function (PSF) of the particle, and is the sum of its primary point spread function $\mathbf{G_0}$ and the reflected point spread function $\mathbf{G_r}$ because we are considering dipole emission close to a planar surface; and μ is the induced dipole moment, expressed as:

$$\boldsymbol{\mu} = \epsilon_m \boldsymbol{\alpha} \mathbf{E_d} \tag{2.12}$$

$$\boldsymbol{\alpha} = \mathbf{I}\alpha \tag{2.13}$$

$$\tag{2.14}$$

Where $\mathbf{E_d}$ is the total driving field, which again is the sum of the incident field and the reflected field. The polarizability magnitude of a nanoparticle in the Rayleigh scattering limit can be written as (van de Hulst, 1958):

$$\alpha = 4\pi r^3 \epsilon_m \frac{\epsilon_p - \epsilon_m}{\epsilon_p + 2\epsilon_m} \tag{2.15}$$

And for a spherical nanoparticle, the tensor reduces to the identity matrix:

$$\mathbf{I} = \begin{bmatrix} 1 & 0 & 0 \\ 0 & 1 & 1 \\ 0 & 0 & 1 \end{bmatrix} \tag{2.16}$$

Based on Equation 2.11, the pure elastically scattered intensity ($I_s = |\mathbf{E_s}|^2$) will depend on the square volume of the particle ($\alpha^2 \propto V^2 \approx r^6$), resulting in exceptionally low optical contrast for small nanoparticles. On the other hand, by considering the sum of the scattered field with a reference, interfering field, the detected intensity will take the form:

$$I_d = |\mathbf{E_s} + \mathbf{E_r}|^2 = |\mathbf{E_s}|^2 + |\mathbf{E_r}|^2 + 2|\mathbf{E_s}||\mathbf{E_r}|cos\theta \tag{2.17}$$

$$I_d = E_s^2 + E_r^2 + 2E_sE_rcos\theta \tag{2.18}$$

Where $\theta = \phi_s - \phi_r$ is the phase difference between the reference and scattered fields, and $|\mathbf{E_x}| = E_x$. Assuming maximization of the phase term ($cos\theta = 1$), and considering weakly scattering particles ($E_s \approx 0$) as well as a strong reference ($E_r >> E_s$), the detected intensity will scale as:

$$I_d \approx E_r^2 + 2E_rE_s \tag{2.19}$$

And therefore, the measured differential signal ($dS = I_d - I_r$ where $I_r = E_r^2$) will scale as:

$$dS = 2E_sE_r \propto r^3 \tag{2.20}$$

This interferometric contribution has a huge impact on the measurable signal for small scatterers, leading to high signal-to-noise ratio (SNR) imaging of sub-wavelength particles. Far-field Green's functions can be utilized to calculate the scattered fields, and Fresnel coefficients are used to calculate the reflected field by the silicon oxide surface as discussed in Section 2.1. By considering both contributions, the measured signal at the camera level can be obtained. To further enhance the measured scattering signal, the oxide thickness has been engineered and optimized, and simulations show that the highest particle-background contrast is achieved at $d(\mathrm{SiO_2})$ = 60nm where $d(\mathrm{SiO_2})$ is the thickness of the oxide (Yurdakul, 2021).

Moreover, the interferometric detection of elastically scattered light by single BNPs requires high numerical aperture in order to collect as many scattering angles as possible. High-NA objectives are being employed on the SP-IRIS setup (NA$\geq$0.4) with high magnification (20-60X). The illumination scheme is more sophisticated than what is required for analog measurements, since better particle contrast can be achieved by engineering the illumination function. On the SP-IRIS, a Köhler illumination geometry is implemented by conjugating the objective back pupil plane with an aperture mask in the source plane. This is obtained by implementing a 4-f system with two lenses of focal length f_1=75mm. The mask is an adjustable diaphragm placed at the output of the integrating sphere. By adjusting the size of the aperture, the illumination angle can be controlled, up to the maximum angle which will be determined by the numerical aperture of the objective. A scheme of Köhler illumination geometry as it is implemented on the SP-IRIS is shown in Figure 2·5. An additional aperture is placed exactly in the middle between the two lenses to minimize stray radiation coupled into the system.

The interferometric image of sub-wavelength particles will be diffraction limited according to the equation:

$$R_{DL} = \frac{\lambda}{2NA} \tag{2.21}$$

Where R_{DL} is the minimum resolvable size and λ is the wavelength. The other limiting factor is the pixel size, which - in order to sample twice the diffraction limited resolution of the system - will need to be smaller than:

$$d_{pix} \leq \frac{\lambda}{4NA} \times M \tag{2.22}$$

Where $M = M_{obj}/M_{sys}$, M_{obj} being the magnification of the objective and M_{sys} the magnification of the system. This places a requirement on the camera to be utilized for nanoparticle detection. For example on a system that uses a 20X objective with 0.45NA at a 518nm wavelength, the maximum pixel size allowed to visualize

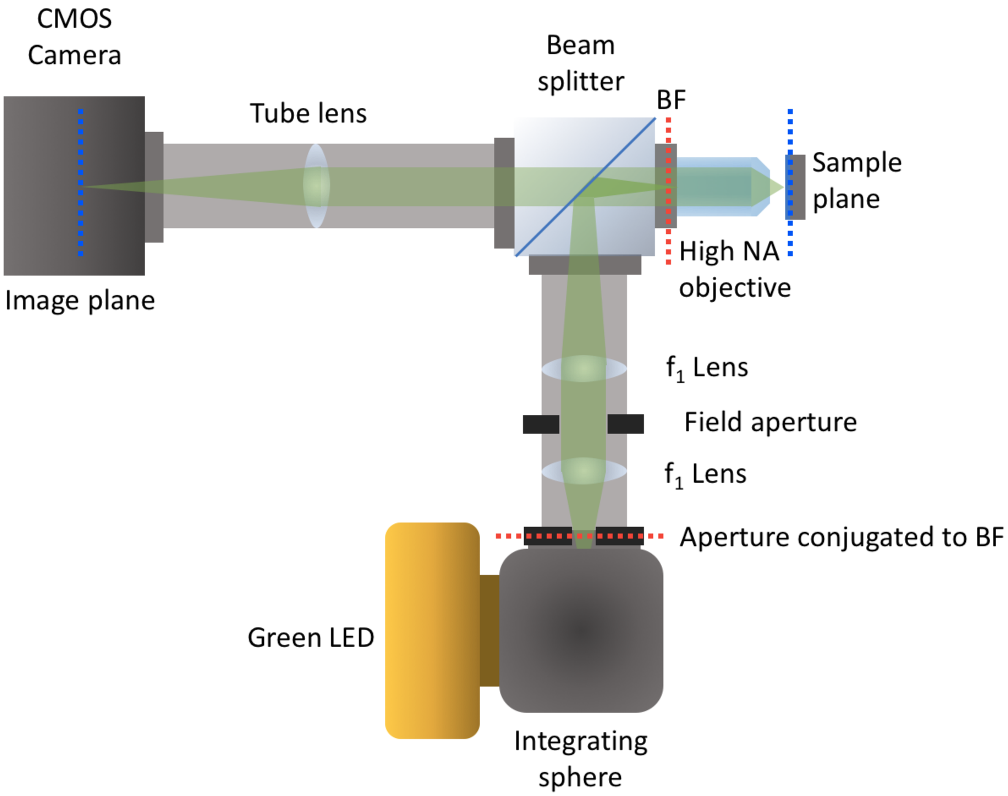

Figure 2·5: A scheme of the optical configuration of the SP-IRIS. BF refers to the back-focal plane of the objective. The lenses in the 4f system have a focal length f_1 of 75mm. Red and blue dotted lines indicate conjugate planes.

diffraction limited particles will be $d_{pix} = 518nm \times 20/(4 \times 0.45) = 5.75\mu m$.

The SP-IRIS system features a XY-manual stage and a focal-direction both manual and piezometric stage. The manual stage is utilized to move across the surface of the chip and for gross focusing, while the piezo is utilized for precision focus adjustments and to acquire defocus images of the particles. By acquiring defocus scans of particles, it is possible to determine their contrast with respect to the background at different focal planes. As an example, the defocus curve of a 100nm polystyrene bead immobilized on an IRIS chip is shown in Figure 2·6. The red curves show the defocus curve of the particle when the surrounding medium is air, while the blue curves refer to the same particle when the chamber is filled with PBS, therefore the particle is immersed in liquid. To simplify, the contrast diminishes when the medium has a refractive index more similar to that of the particle, and the defocus curve broadens.

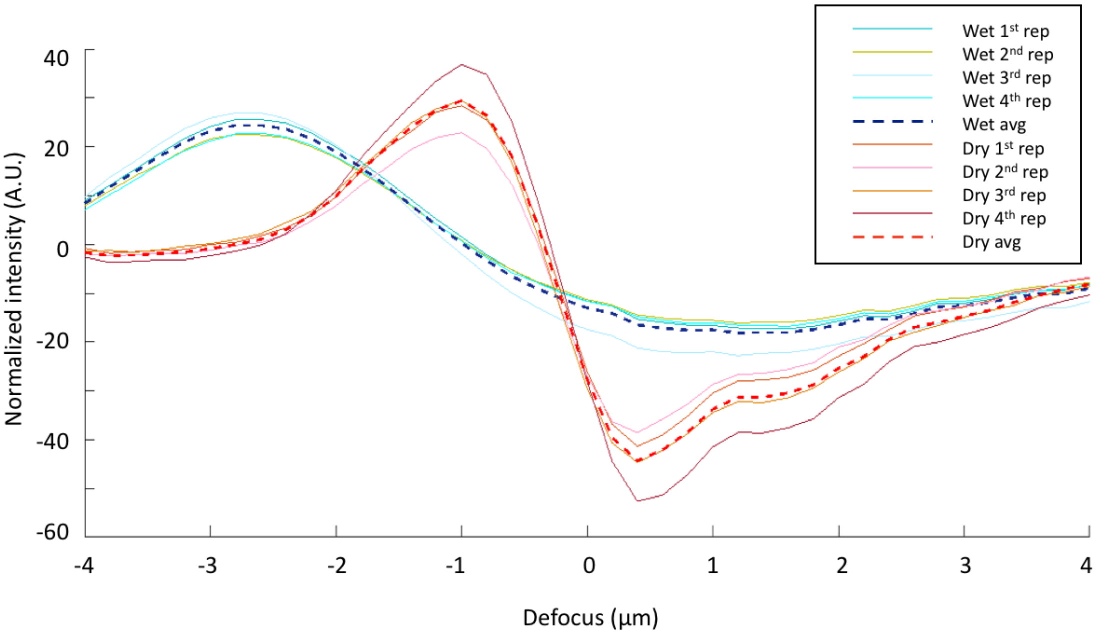

Figure 2·6: The defocus curve of a polystyrene bead immobilized on an IRIS 60nm-SiO_2 chip, immersed in air (red curves) and in PBS (blue curves). The same particle was imaged in each medium four times and the average curve was calculated (dashed lines).

2.3 Combining analog and digital detection

While high-resolution, high-sensitivity single nanoparticle detection has recently seen a huge rise in popularity due to the impact it has in the diagnostics and personalized medicine field, the drug development industry is focusing more and more on small molecules as the next generation medicines, given the many advantages they bring in terms of easy access to the cell through the cellular membrane. As detailed above in Section 4.1, characterization of these chemical compounds in a label-free manner is equally challenging, due to the minuscule optical signal they produce when accumulating on the sensor surface. These considerations show a need for a versatile, flexible and robust platform with the ability to handle very diverse samples without losing sensitivity and reproducibility.

As detailed in the previous Sections 2.1 and 2.2, in the past decade, the IRIS technology has seen development along two well defined directions: biomass accumulation sensing (*analog* configuration), applied to kinetic analysis of proteins, antibodies, and oligonucleotides; and single nanoparticle detection and phenotyping (*digital* configuration), for specific characterization of viruses, bacteria and extracellular vesicles. However, in a sense, the analog configuration is simply a generalization of the digital one: the increase in planar reflectance that we define as analog signal is in fact light scattering by single molecules that interferes constructively. In Figure 2·7 we schematically show how the analog signal produced by molecular accumulation can be seen as a generalization of the digital signal generated by single particles. As one of the main objectives of this dissertation, we have explored this concept by merging these two configurations together on the same platform, creating a new instrument, the hybrid IRIS system (h-IRIS). By optimizing illumination and collection optics, as well as illumination wavelength and oxide thickness, analog and digital measurements were successfully performed on the h-IRIS with minimal hardware adjustments, as presented in the Results Section (Section 4.3). In this Section, on the other hand, we will go through the optimization steps that were performed in order to obtain such results.

In the past, each configuration of the IRIS instrument was developed with a different optical configuration, as well as specific hardware and software characteristics. Generally, for biomass accumulation measurements (*analog* configuration), low magnification, low-numerical aperture (NA) objectives were utilized, in order to maximize the field of view and minimize non-normal reflection. Having a large field of

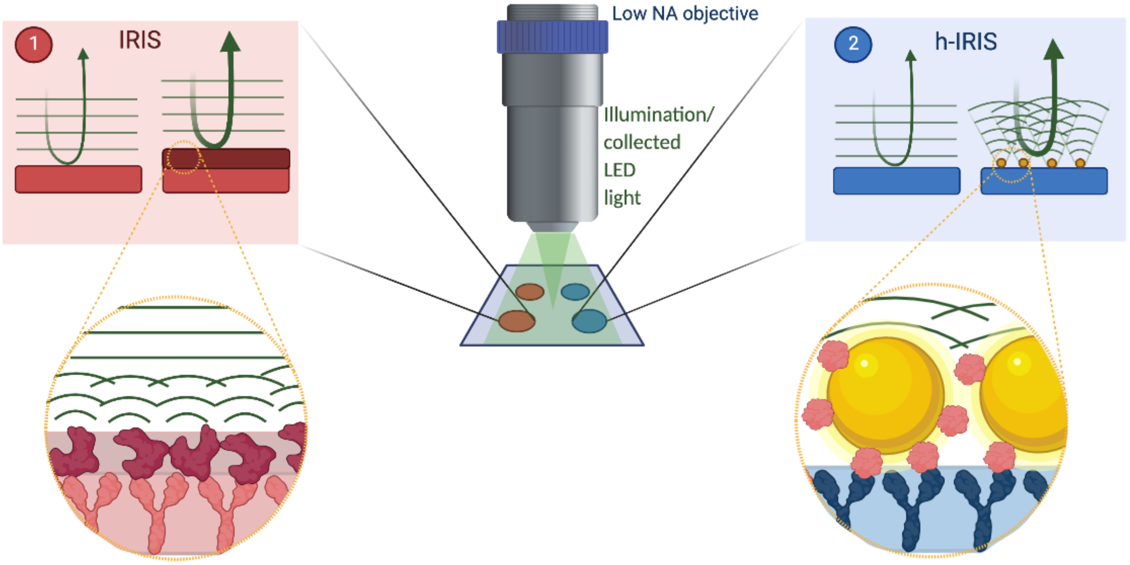

Figure 2·7: A simplified scheme of the signal measured on 1) the standard analog IRIS system and 2) the h-IRIS system in its analog configuration.

view (FOV) is essential for multiplexing: the field of view on the current IRIS analog instrument is 5mm x 7mm, and with an average diameter of a microarray spot of 100μm, this FOV allows for monitoring of thousands of spots at the same time. This translates to hundreds of possible probe conditions that can be monitored simultaneously. The SiO_2 layer on analog IRIS chip needs to be $>$100nm in thickness, and is engineered in order to maximize the changes reflectance due to biomass accumulation at an LED wavelength, typically blue. Moreover, for low-magnification analog measurements, a simple illumination scheme such as critical illumination can be utilized, while for digital measurements a more sophisticated illumination scheme such as Köhler illumination is required, to avoid artifacts caused by imaging the source onto the image plane.

As mentioned above, the final goal of the hybrid IRIS (h-IRIS) platform is to detect the analog signal produced by nanoparticles (NPs) rapidly accumulating on the sensor surface, particularly when they do not produce a carpet, i.e., the surface of the spot is not fully covered, by exploiting the constructive interference produced by adjecent NPs. A simplified scheme of the signal measured on the h-IRIS system is reported in Figure 2·7. Such measurements are performed with a low-NA objective and full NA illumination. Then, the nanoparticles are imaged in a digital fashion by switching to a high-NA objective and low-NA illumination. This technique allows for measuring the affinity of low concentrated samples to their antibodies by NP-labeling, in a multiplexed fashion, and then 'digitally' count and phenotype the single NPs. So far, the main application of this method is the characterization of mAb-GNP complexes for lateral flow assays; however, since on the analog IRIS sensor we achieved characterization of EVs, and then imaged them on the SP-IRIS system, a new application of the h-IRIS could be characterization and imaging of EVs and other biological NPs.

Practically, when switching from high to low collection NA for nanoparticle detection, both resolution and contrast are lost, for two main reasons: first of all, the minimum resolvable size R_{DL} (Eq. 2.21) is increased; additionally, much less light is collected and at smaller angles, therefore reducing the total acquired intensity and favoring forward scattering. Since the scattering from a single NP is approximated as a spherical wave, not being able to collect light at large angles clearly reduces the measurable scattered signal with respect to the planar background. Here, loss in resolution is not important for analog signal measurements. However, loss in contrast is, and therefore maximizing the NA is still crucial. Figure 2·8 is a photo of the physical h-IRIS setup, and in the next few sections, we will detail its features, in order to summarize the main hardware adjustments that were performed to build the versatile platform.

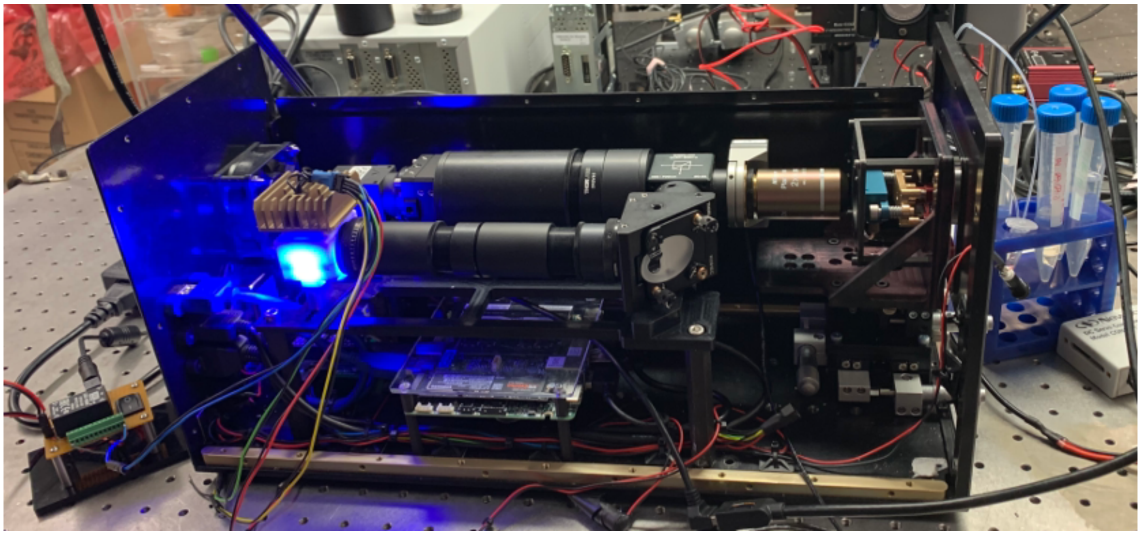

Figure 2·8: A photo of the physical h-IRIS platform.

2.3.1 Illumination on the hybrid IRIS system

On the h-IRIS platform, Köhler illumination geometry was implemented. In addition to the many advantages it provides in terms of visualization improvement for NP scattering, this illumination scheme is also effective for analog measurements since it improves illumination uniformity.

Furthermore, it has been demonstrated that the best interferometric contrast for single NPs on the IRIS system is obtainable at low illumination NA, due to the preferred excitation in that case of horizontally-oriented dipoles, which generate a more intense scattering signal in the near-normal direction (Avci et al., 2017). On the other hand, the analog system operates in a shot-noise limited regime (Section 3.1), and for this reason it is essential to maximize the total acquired signal in order to minimize the noise. The best way to increase the acquired reflectance signal is to maximize the total light that is shined on the chip, and that requires full NA illumination. Therefore, one of the minimum hardware adjustments necessary to switch from analog to digital measurements on the h-IRIS is to adjust the pupil mask placed in front of the integrating sphere, reducing it from 13mm in diameter for analog measurements (maximum) to around 3mm for digital.

In terms of choosing the best LED wavelength for hybrid measurements, simulations show that green LED light (center λ=518nm) is the best compromise between decent biomass accumulation sensitivity and high single-nanoparticle contrast, especially for gold nanoparticles (GNPs). We optimized the system for single GNP detection since our main application of the h-IRIS platform is the analog-to-digital study of GNP-mAb complexes. The simulation results are shown and further commented in Section 3.2.3.

2.3.2 Camera and objective selection

Having a small pixel size is crucial when running single-NP detection experiments. As defined in Equation 2.22, there is a limiting pixel size above which diffraction-limited NPs are not discernible anymore. On the other hand, for kinetic measurements, the limiting factor is the acquisition speed: for the same camera sensor size, smaller pixels cause extra computational effort, thus resulting in slower acquisition times. As we will explain in detail in Section 3.1, the best way to reduce the noise on the IRIS system is by spatial and temporal averaging. Particularly, temporal averaging consists in averaging together multiple acquired frames to obtain a single image. For kinetic experiments, we have demonstrated that averaging 100 frames is an ideal compromise between major noise reduction and maintaining good temporal resolution (Chiodi et al., 2020a). Since most of the molecular interactions we have investigated happen on a timescale on the order of 30 seconds to ten minutes, a good time resolution would be in the order of seconds. A camera sensor that has a frame rate of 50fps would allow us to acquire an averaged image every 2s, which is acceptable.

Therefore, in order to combine single NP resolution with kinetic measurements, it is necessary to compromise on a camera with a large enough sensor size in order to achieve multiplexing for kinetic measurements, and whose time resolution does not drop below 50 frames per second (fps); at the same time, the pixel size should be small enough to allow for resolution of diffraction-limited particles. The table below summarizes the requirements of the h-IRIS system, together with the characteristics of the currently employed cameras for analog and digital detection, respectively.

Table 2.1: Camera comparison of the GS3-U3-51S5M (standard for digital configuration) and the BFS-U3-17S7M (standard for analog configuration).

	h-IRIS requirements	**GS3-U3-51S5M (Std digital)**	**BFS-U3-17S7M (Std analog)**
FWC (electrons)	Largest possible	10361	98645
FPS (frames/s)	≥50	38	196
Resolution (MPixels)	Largest possible	5.0	1.7
Sensor Size (mm^2)	Largest possible	8.45 x 7.07	14.4 x 9.90
Pixel Size (μm)	≤5.75	3.45	9.00

As one can see from the table above, neither the standard (std) digital or analog configuration cameras satisfy all the requirements: the pixel size on the digital sensor is very small and therefore the frame rate is far too slow. Moreover, the sensor size is much smaller than what is normally used for analog detection, reducing multiplexing capabilities for kinetic measurements. On the other hand, the pixel size on the std analog sensor would not allow to resolve single scattering nanoparticles with a 20X, 0.45NA objective. After a meticulous search and optimization of all the parameters, we consider a good compromise between the characteristics of these two cameras to be the BlackFly BFS-U3-70S7M, the features of which are summarized below.

Table 2.2: Comparison of the h-IRIS system requirements in terms of camera sensor, with the characteristics of the chosen camera BFS-U3-70S7M.

	h-IRIS requirements	**BFS-U3-70S7M (Chosen sensor)**
FWC (electrons)	Largest possible	25420
FPS (frames/s)	$\geq$30	51
Resolution (MPixels)	Largest possible	7.1
Sensor Size (mm^2)	Largest possible	14.4 x 9.90
Pixel Size (μm)	$\leq$5.75	4.5

This sensor is ideal for our purpose of adapting a system to do both single NP detection as well as multiplexed kinetic measurements: it has a decent full well capacity, not as large as on the analog sensor but still more than two times larger than that of the standard digital sensor. Moreover, its pixel size is small enough to resolve diffraction limited particles on a 20X objective with 0.45NA, but not too small - allowing for a decently fast frame rate, 51 fps, satisfying the time resolution requirement for kinetic measurements.

For what concerns objective selection, there are a few incompatibilities between the two applications that require that a different objective is used for each of them. For kinetic measurements, low magnification is needed as multiplexing is essential. Lower NA is acceptable since we are approximating illumination with normal incidence, however, on this system it is necessary to have a high enough NA that allows to acquire the scattering signal produced by single NPs in an analog fashion. Simulations shown in Section 3.2.3 demonstrate that with an NA of 0.15 (5X objective) single NPs are non-resolvable but the bulk scattering signal is still measurable. Therefore, for analog measurements, our objective choice landed on a 5X, 0.15 NA objective from Nikon (MUE12050) while for digital measurements we utilized a 20X, 0.45NA objective (MRH08230). The latter was chosen because it allows us to visualize diffraction-limited particles and still preserve a good field of view for digital imaging: approximately 3mm x 2 mm, allowing to visualize four $400\mu m$ diameter spots simultaneously.

2.4 State of the art of label free detection and competing technologies

In the context of label-free detection, kinetic measurements are utilized to evaluate the affinity of two molecules binding to one another, and biomass accumulation is translated to an analog signal by a transduction mechanism. In most cases, the measurement is based on detecting a small variation of an optical parameter close to the surface of the sensor, such as the refractive index. Sensors whose working principle is based on such a measurement are referred to as *optical biosensors*. However, there are few examples in the literature of sensors based on the modification of mechanical properties, such as the tension of a cell membrane (Zhang et al., 2018), or the oscillations of piezoelectric crystals (Pohanka, 2018).

In general, there are a few label-free optical biosensors that are well established in the field, and are widely utilized both in academic and industrial research for molecular discovery. The gold standard in this sense is Surface Plasmon Resonance (SPR). SPR sensors are label-free optical sensing tools that base their working principle on the resonant coupling of an evanescent field with the plasmonic excitation of the electrons in a gold layer, in order to measure local refractive index variations.

Practically, an SPR biosensor is constituted by a gold-coated glass prism that is functionalized with a reactive hydrogel layer where probe molecules are covalently immobilized. During an SPR measurement, a solution containing a relevant concentration of target analytes is flowed across the surface of the sensor thanks to a microfluidic system that converges to a fluidic chamber. This way, the gold layer is enclosed between the solution and the glass, creating two metal-dielectric interfaces. To detect refractive index variations, p-polarized monochromatic light is shined at a specific angle θ_{SPR} on one side of the prism, and the reflected light is measured on the other side of the prism by an array of photodetectors, as shown in in Figure 2·9.

In this configuration, light propagates from a medium with higher refractive index (n_{glass}) to a medium with lower refractive index ($n_{solution}$), and total internal reflection (TIR) can be achieved for all incidence angles above a critical angle $\theta_c = n_{solution}/n_{glass}$. Since $\theta_{SPR} > \theta_c$, this generates an evanescent field which extends into the solution with exponentially-decaying amplitude. The evanenscent field is represented in Figure 2·9 by a continuous black line.

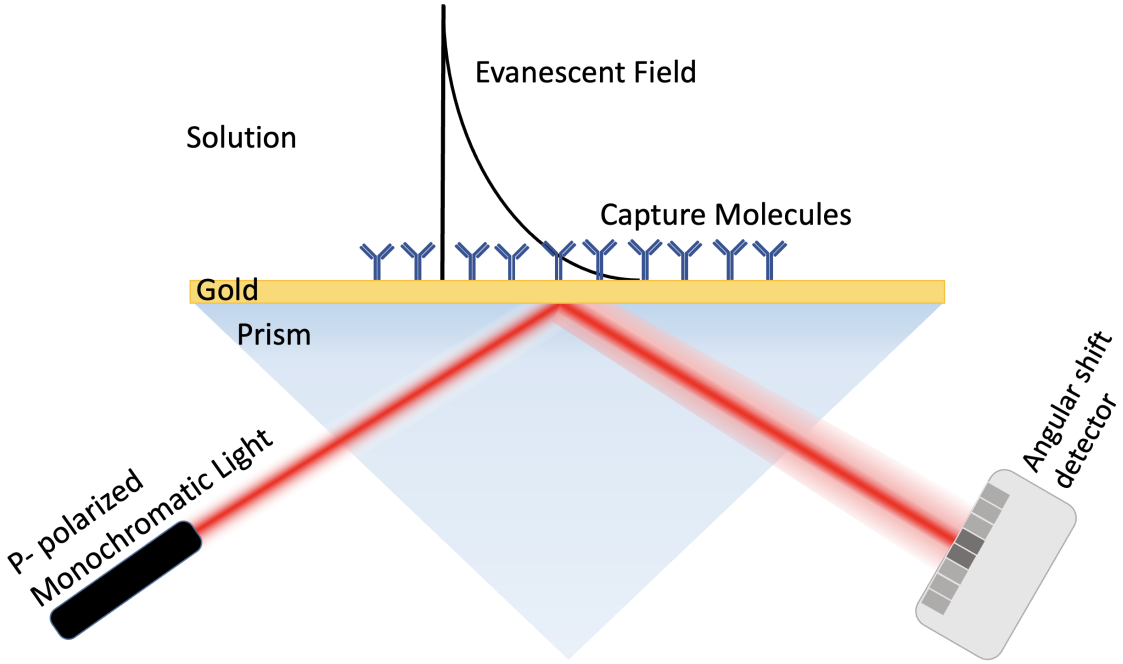

Figure 2·9: A simplified scheme showing the working principle of a Surface Plasmon Resonance (SPR) sensor.

When phase-matching conditions are met, the evanescent field is strongly absorbed by the ≈50nm-thick gold layer, thanks to the abundance of free electrons in the metal ('electron plasma' = plasmon) (Schasfoort, 2017). The absorption generates a 'dip' in the measured reflected intensity on the other side of the prism, measured by the photodetectors. The specific angle of incidence θ_{SPR} which meets the phase-matching conditions depends very strongly on the refractive index in proximity of the gold layer, as described below.

Briefly, when one considers the wavevectors of the incident and evanescent fields respectively, Snell's law requires the components parallel to the metal-dielectric interface to match ($k_{x,i} = k_{x,ev} = k_x$ when considering xy as the plane of incidence as shown in Figure 2·9). Therefore, the p-component of the wavevector $k_{p,ev}$ assumes the form (Tang et al., 2010):

$$k_{p,ev} = \sqrt{k_x^2 + k_{y,ev}^2} = \frac{2\pi}{\lambda} n_{glass} \sin(\theta_i) \tag{2.23}$$

On the other hand, by applying Fresnel equations for a three-layer interface, the wavevector at which it is possible to achieve plasmon excitation for a thin gold layer in the SPR configuration (glass-gold-solution) can be calculated (Tang et al., 2010; Schasfoort, 2017; Kurihara and Suzuki, 2002):

$$k_{p,PE} = \frac{2\pi}{\lambda} \sqrt{\frac{n_{solution}^2 n_{gold}^2}{n_{solution}^2 + n_{gold}^2}} \tag{2.24}$$

Where $k_{p,PE}$ stands for Plasmon Excitation (PE). By imposing phase matching at the interfaces, one can derive the optimal incidence angle $\theta_i = \theta_{SPR}$ to obtain resonant coupling of the evanescent field with the plasmon excitation (Tang et al., 2010; Schasfoort, 2017; Kurihara and Suzuki, 2002):

$$\theta_{SPR} = \sin^{-1}\left(\frac{1}{n_{glass}} \sqrt{\frac{n_{solution}^2 n_{gold}^2}{n_{solution}^2 + n_{gold}^2}}\right) \tag{2.25}$$

SPR biosensors provide real-time monitoring of interactions of a wide range of analytes, enabling fast, sensitive and specific kinetic measurements. In the past decade, SPR platforms have been utilized for the detection of viruses, bacteria, biosimilar molecules and proteins. Studies show that accurate and early recognition of infectious diseases biomarkers can be performed in real-time (Saylan et al., 2019). Today, these biosensors are utilized in many areas, including basic biochemical studies such as interactions between protein and protein, or DNA-DNA, in clinical, environmental, and agricultural settings (Bakhshpour and Denizli, 2020).

For many applications, however, SPR is not an ideal solution, as there are several disadvantages to the technique. First of all, measuring kinetics of low molecular weight (LMW) analytes, also defined as *small molecules* (SMs, MW<1kDa, (Piehler et al., 1996)) is not ideal on SPR, since the surface chemistry utlilized on SPR chips requires probe molecules to be immobilized in thick hydrogels. This helps increasing the binding signal by creating multiple layers of probes, but, on the other hand, it causes most reactions to be diffusion limited (Li et al., 2015; Nikolovska-Coleska, 2015). Moreover, SPR is incredibly sensitive to environmental conditions: measurements can be affected by temperature or pH shifts, vibrations, and slight changes in the refractive index of the running solution (General Electrics Company, 2012). The latter is a challenging issue when working with small molecules, since low-molecular weight compounds are usually insoluble in acqueous buffers, therefore high-refractive index solvents are needed to dissolve them. One of the most commonly utilized solvents is dimethyl sulfoxide (DMSO), which has a refractive index n=1.479 at visible wavelength - much higher than that of the typical running buffer, phosphate buffer saline (PBS - n=1.335). The signal generated on SPR by a solution containing 1% DMSO is hundred times larger than the signal generated by binding of low molecular weight analytes (General Electrics Company, 2012). These difficulties, together with the complexity of operating an SPR instrument and the elevated cost of both the system and its consumables, draw attention to the need for a simpler, more robust and cheaper method for biomolecular kinetic analysis.

Another example of a biosensor widely utilized and well established in the field is Bio-Layer Interferometry (BLI). Similar to the IRIS, the working principle of BLI sensors is also based on interferometry. However, in this case, probe molecules are immobilized on the tip of an optical fiber that contains an internal reference reflecting layer. The functionalized fiber tip is submerged in a microwell plate containing the analyte solution. White light is coupled to the fiber, and reflected light from the fiber tip is acquired. Measurable reflectance shifts occur when analyte molecules bind to the fiber tip. Then, the tip is moved to a different well that contains an analyte-free buffer solution for the wash step. A graphical scheme of the working principle of BLI is shown in Figure 2·10.

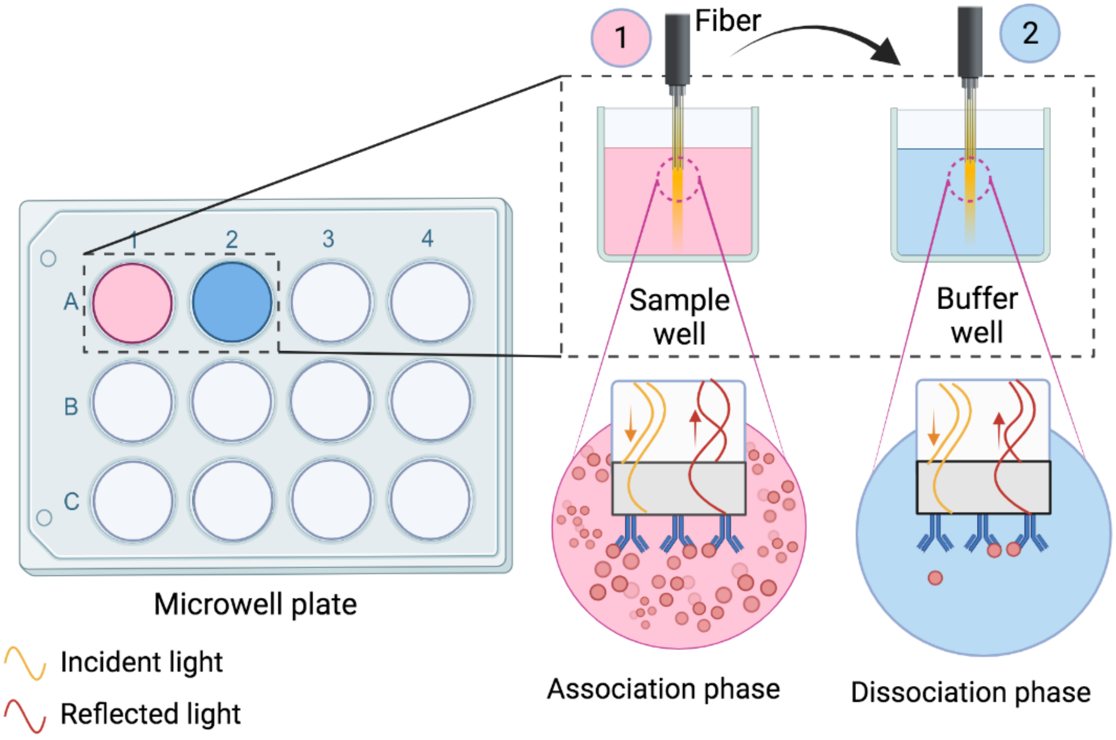

Figure 2·10: A simplified scheme showing the working principle of a Bio-Layer Interferometry (BLI) sensor.

The main advantages of BLI are its ease of operation, its reduced cost with respect to SPR, its high throughput, and the fact that it is compatible with well-plate systems. However, diffusion limit remains a problem since the analyte diffusion obtained by shaking and rocking the well plate is not as effective as flowing an analyte solution across the surface. Moreover, functionalizing fiber tips can be cumbersome and time consuming. And finally, when moving the fiber tip from one well to another, an artifact in the measured signal appears, which requires post-processing of the data in order to be removed.

In terms of bulk effect corrections, both SPR and BLI utilize a negative channel, or a negative well, which has an environment similar in refractive index to that of the active channel, and where a blank solution is flowed (or added for BLI). Such blank signal is subtracted from the kinetic data in post-processing. This is not an ideal approach, since the outcome is extremely vulnerable to slight differences between the active and inactive well or channel. While the IRIS system is not as susceptible to bulk effect as these two techniques, when working with small molecules, even the slightest background change can affect the quality of the signal. Therefore, we have implemented a method for bulk-free measurements that will be explained in detail in Section 3.4.1. Moreover, functionalization of the IRIS chip is much simpler with respect to both SPR and BLI consumables. A simple polymeric coating is enough to produce a monolayer of probe molecules, that will be stably immobilized while preserving their structure. A more detailed explanation of how surface chemistry can affect kinetic measurements will be given in Section 3.5.

Chapter 3

System Optimization

3.1 Noise Analysis

3.1.1 Shot noise limited operation and averaging

Building an instrument that can characterize targets with very different biophysical properties requires optimization of all possible parameters, in order to perform accurate measurements at both extremes of the molecular weight spectrum. Particularly, detection of small molecules (SMs) in a label-free fashion requires extremely high sensitivity, as we discussed in Section 1.2.1. Here, we will review the main limiting factors to the sensitivity of the IRIS, as well as the ultimate sensitivity limit in terms of physical properties of the system.

The first element to consider when analyzing the sensitivity of an imaging system is the camera sensor; the sensor currently employed on the IRIS is a scientific grade CMOS camera. Generally, noise sources in CMOS sensors include dark current noise (σ_D), read noise (σ_R), fixed pattern noise (σ_F), and shot noise (σ_S). Dark current noise is temperature dependent, and is defined as the noise produced by thermal excitation of the electrons in the junction. It can be quantified as dark current (I_D) times the exposure time (t): $\sigma_D = \sqrt{I_D \times t}$ This type of noise can be relevant when the sensor is overheated, but is generally negligible if the camera does not exceed room temperature during experiments. Read noise is dependent on sensor design, particularly the production of the electronic signal, while fixed pattern noise depends on the fabrication quality of the sensor chip; scientific grade cameras are typically designed and carefully fabricated to minimize both these noise sources. Finally, shot noise originates from the discrete nature of light and electric charge, and this source of noise can often dominate in bright field imaging. The effective noise results from combining the contributions from each of these noise sources:

$$\sigma_{eff} = \sqrt{\sigma_D^2 + \sigma_R^2 + \sigma_F^2 + \sigma_S^2} \tag{3.1}$$

In the product specifications of the FLIR BFS-U3-17S7M camera (used in the IRIS system), the sum of read noise and dark noise values is given as 3.1x10^{-4} Noise/Signal. To experimentally verify this value, we measured the level of noise produced in the sensor when there is no light impacting it for two hours. The measured noise level was around 10^{-5} Noise/Signal (Marn, 2021), which is negligible compared to shot noise. This demonstrates that the signal acquired by the IRIS is shot-noise limited.

Shot noise is defined as the statistical noise associated with the arrival of photons at the sensor, and their conversion to electrons. Due to the discrete nature of light, the occurrence of the event of photons hitting the sensor can be described by a probability distribution, particularly by a Poisson model, the same that describes the probability distribution of coin tosses. The signal to noise ratio (SNR) in a Poisson distribution increases as the square root of the number of events $\sqrt{N}$, where N in this case is the number of photons hitting the sensor; thus, the easiest way to improve the SNR is to increase the amount of light on the camera. In CMOS sensors, the maximum collectable signal corresponds to the full well capacity (FWC) of the sensor's pixels. Shot noise cannot be infinitely reduced, and even the best camera sensors available on the market are affected by it, especially since there is a limit to the largest obtainable value for the FWC. Particularly, in order for us to achieve small molecule sensitivity on the IRIS system, selecting a sensor with a very large FWC was not enough. We therefore implemented an additional SNR improvement method by performing temporal and spatial, or ensemble, averaging of signal collected by adjacent pixels.

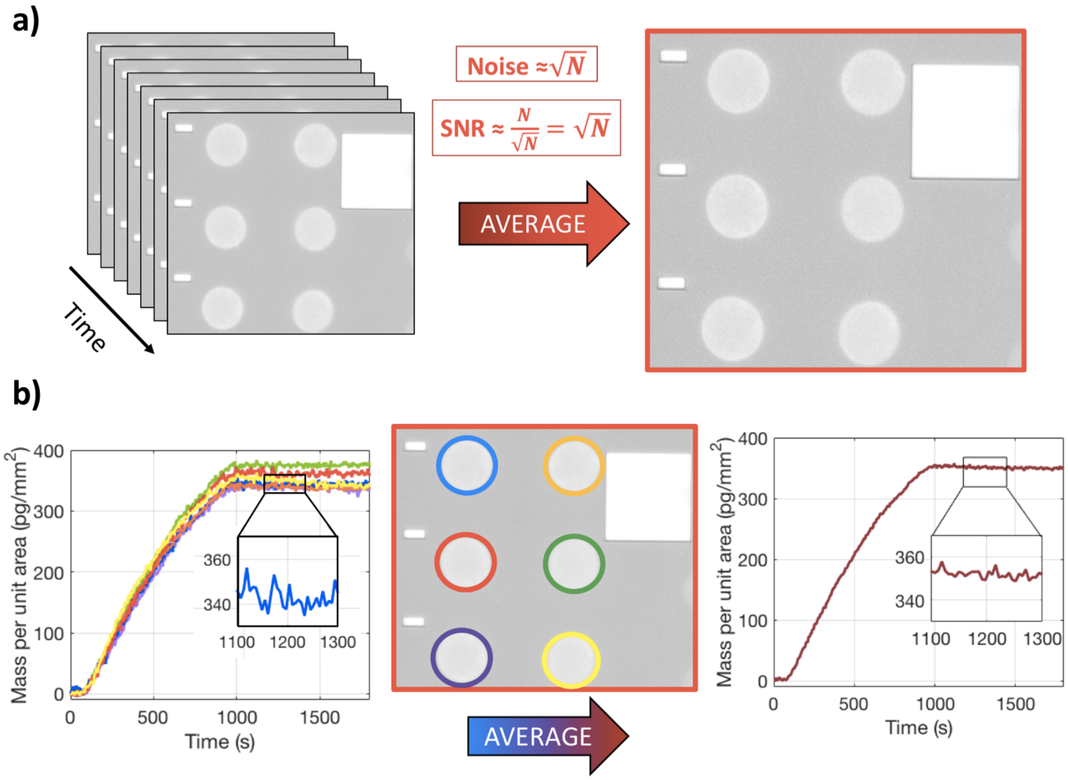

Figure 3·1: A graphical representation of a) temporal and b) ensemble averaging, as the two main methods utilized on the IRIS platform to improve the SNR. The insets in the binding curves in b) show the level of noise before (blue) and after (burgundy) performing ensemble averaging.

A temporally averaged signal value is obtained by averaging the intensity from the same pixel in subsequently acquired frames, while a ensemble average is performed by averaging the signal acquired from adjacent pixels on the same image. Practically, temporal averaging is also referred to as frame averaging, which in our case is carried out during acquisition, and consists of acquiring a predefined number of frames (N_f), summing the acquired intensity, then dividing it by N_f, obtaining a single, averaged image. The frame rate of the camera, together with the amount of performed temporal averaging, defines the temporal resolution of the system. On the other hand, an example of ensemble averaging on the IRIS is the average of the signal from pixels belonging to the same probe spot. When there are more spots with the same probe condition on the surface, signal from identical spots can also be averaged. An illustration of the meaning of ensemble and temporal averaging is shown in Figure 3·1.

Since we are working in shot-noise limited operation, the noise is quantified as the standard deviation over the signal. Figure 3·2a and 3·2b show the theoretical noise reduction expected from temporal and ensemble averaging in a shot noise-dominated model (blue dashed lines), as well as the experimentally measured noise reduction (black lines). Figure 3·2a depicts the noise-to-signal ratio for one single pixel when an increasing number of frames is averaged, confirming the dependence of the noise on $\sqrt{N}$. In our case, the optimal number of averaged frames was a hundred frames. This number was obtained as a compromise between minimizing the noise and not impacting time resolution. On the other hand, Figure 3·2b reports the trend of the noise-to-signal level when all the pixels belonging to an increasing number of 100μm microarray spots (5024 pixels each) are averaged. This noise reduction is calculated on top of 100 averaged frames for every considered spot. It has to be pointed out that the deviation of the experimental trend from the theoretical model in Figure 3·2b should be attributed to the fact that the spots are not identical to each other, and also to the noise generated by particles and small bubbles passing across the surface of the chip through solution flow.

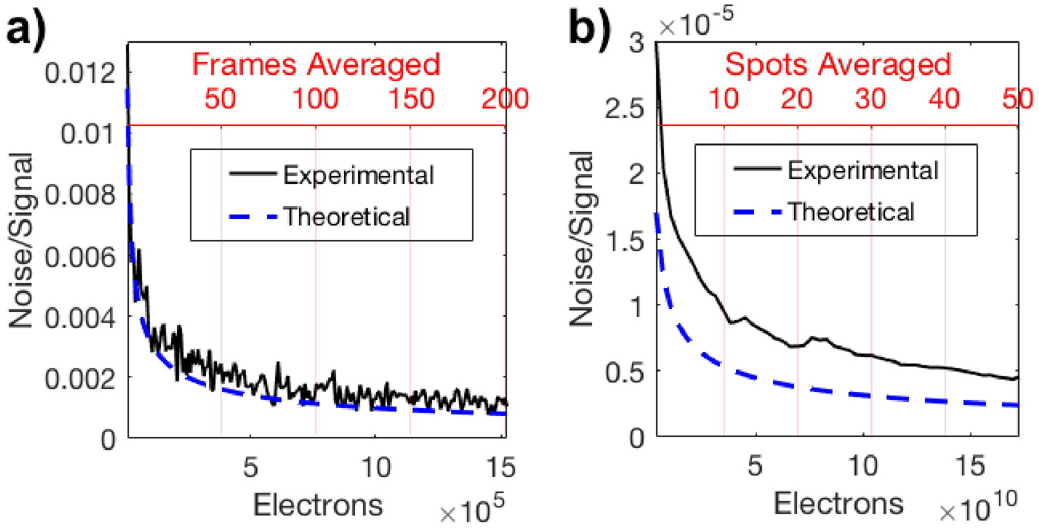

Figure 3·2: The effect of averaging on the IRIS signal. Theoretical and experimental reduction in the noise level due to (a) temporal averaging and (b) ensemble averaging. Reproduced with permission from (Chiodi et al., 2020a).

This results shows the effect of averaging on the SNR of acquired data on the shot-noise limited IRIS system, highlighting the importance of optimizing averaging parameters when running small molecule detection experiments. Results obtained by applying this model to SMs characterization data are shown in Section 4.1.

3.1.2 Ultimate sensitivity limit

In a shot-noise dominated model, the performances of the sensor strictly depend on the available hardware. Not only does the FWC of the camera sensor play a crucial role, but also its frame rate and field of view, since those two characteristics influence our capabilities to perform ensemble and temporal averaging. Moreover, the radiance of the available LEDs limits the amount of light that we can shine on our sensor, posing another limit in terms of how much signal can be collected. Even if a camera with an extremely large FWC existed, we would still be limited by the performances of the LED source.

Here, we would like to calculate what would be the ultimate limit in sensitivity of the IRIS platform by considering ideal hardware (LEDs with maximum possible power, minimized losses, camera with the largest possible FWC). What would be the limiting factor in that case?

First, we will remove the limit on the FWC of the camera: we will hypothesize using a camera with an unlimited FWC, thus able to potentially collect an enormous amount of signal. In that case, the maximum signal we can acquire for one frame will be limited by the shutter time, which will limit our time resolution, and by the radiance of the LED source.

Ideally, if we could irradiate our chip with an incredibly large amount of light in a small time, the shutter time would not be a limiting factor anymore, but rather the amount of light we would be able to shine on our chip. We will therefore assume the chip to be irradiated with a very large amount of light, and ask ourselves what is the maximum amount of light we can shine on the surface before that becomes a limiting factor.

We will start by considering the highest power LEDs available at present time on the market. Visible wavelength LEDs from ThorLabs have a maximum power output in the order of 1000 mW = 1W (ThorLabs M415L4, Violet). However, some of that power will be dissipated as heat, and, as it can be found in the LEDs specifications, the measured irradiance with no focusing measured at 200mm from the source is in the order of $10\mu\mathrm{W/mm}^2$. Calculating the radiance of an LED from its intensity measured at a certain distance can be done by approximating it to a point source emitting forward, and integrating its emission over the full-width half-maximum (FWHM) angle given in its specification. In this case, the FWHM angle is 120°, which results in a polar angle of 60°. The area of the irradiated screen will therefore be:

$$A = \pi R^2 = \pi(d \times \frac{\cos\theta}{\sin\theta})^2 \tag{3.2}$$

$$A = \pi\frac{200mm}{\sqrt{3}} = 41,187mm^2 \tag{3.3}$$

Thus the total radiance will be:

$$10\frac{\mu W}{mm^2} \times 41,187mm^2 = 412mW \tag{3.4}$$

Which is around 40% of the maximum LED emitted power. We will now ignore the losses due to propagating the radiation through the optics, and we will assume to be focusing all that light in a small spot on the surface of the chip. In our case, the size of such spot can be calculated by using the field number of the objective, that is the diameter of the maximum field of view obtainable with that objective multiplied by its magnification, and can be found in the objective specifications. On the h-IRIS system, analog measurements are performed with a 5X objective with a field number of 22mm, therefore the diameter of the maximum obtainable FOV is $22/5 = 4.4$mm, which results in a spot area of $\pi(2.2\text{ mm})^2$ =15.2mm^2.

When focusing light onto a small spot, part of the radiation will contribute to heat up the irradiated area. The power in mW corresponds to the amount of mJ/s delivered to the surface. Therefore, the maximum heat produced in a second will be 418mJ. We can calculate how that heat would affect the system. In our case, the irradiated area is around 15mm^2, and is composed of a 1mm-thick layer of glass, a 130μm-thick layer of solution and a 1.5mm-thick silicon chip. Glass and water are mostly transparent to visible light, therefore most of the radiation is absorbed and dissipated by the silicon chip. Out of the three materials, silicon is the one with the lowest heat capacity and greatest heat conductivity, thus it would probably easily dissipate the heat produced by the light. However, if we imagine that all 418mW are focused on a 15.2mm^2 area on the silicon chip, that would mean all the heat will be concentrated on a cylinder of silicon with a base area of 15.2mm^2 and a thickness of 1.5mm, which can be converted to mass in grams by using density:

$$m^{Si} = \rho^{Si} \times V^{Si} = 2.33\frac{g}{cm^3} \times 0.0228cm^3 = 53.1mg \tag{3.5}$$

The specific heat of silicon is $c^{Si} = 0.7Jg^{-1\circ}C^{-1}$. Using the simple thermodynamics formula for conservation of heat ($\Delta Q = mc\Delta T$), we find that:

$$\Delta T = \frac{0.418J}{0.053g \times 0.7Jg^{-1\circ}C^{-1}} = 11.1^\circ C \tag{3.6}$$

So would the surface of the chip increase temperature this fast? Not really, since silicon has a great thermal conductivity ($\tau^{Si} = 1.3Wcm^{-1\circ}C^{-1}$) and would dissipate the heat incredibly fast. Therefore, the heat would certainly propagate through our chip: we can thus apply the formula above for our entire chip, which was weighed and measures m^{chip} =0.5±0.01 g.

$$\Delta T = \frac{0.418J}{0.5g \times 0.7Jg^{-1\circ}C^{-1}} = 1.18^\circ C \tag{3.7}$$

If the chip was isolated, and all the irradiated LED power was focused on it, the temperature increase it would experience would be $\Delta T = 1$°C every second. However, the chip lays on an aluminum chuck (the chip holder fixture) which is a cube of approximately 5cm-side. Therefore, the heat would dissipate through the metal, at a speed dictated by the aluminum thermal conductivity, which is even higher than that of silicon ($\tau^{Al} = 2.39Wcm^{-1\circ}C^{-1}$). So, a standard LED, even the most powerful one, assuming no propagation losses, would not be able to heat up our system by an amount that would cause a problem with the measurements.

Assuming that more powerful LEDs will be produced in the future, we will now calculate how much power is needed to heat up the system to a temperature harmful for the functionality of the molecules. We will consider a final temperature around 70°C, since it is above the denaturation temperature of most proteins (Loveday, 2016). Assuming that the experiment starts at room temperature (25°C), in order to heat the chip by 70-25 = 45°C, the absorbed radiation should produce:

$$\Delta Q = (0.5g \times 0.7Jg^{-1\circ}C^{-1} + 337.5g \times 0.89Jg^{-1\circ}C^{-1}) \times 45^{\circ}C = 13532J \qquad (3.8)$$

Which we can divide by the energy produced by the LED in one second (418mJ), resulting in Δt = 9 hours needed to heat up the chuck to that temperature. Considering that the chuck is connected to the aluminum box enclosing the instrument, which will also dissipate part of the heat, it would certainly take longer. However, if we assume that more powerful LEDs will be produced, or to utilize a different light source, it would be possible that the focused light would heat up the system to a point that measurements would not be performable. Ultimately, that would pose a limit to the reachable sensitivity on the IRIS system.

3.1.3 Long-term stability for low $\mathbf{k_{OFF}}$ analytes

One other important aspect to consider when optimizing a system for diverse analytes is stability, since several biomolecular interactions at high affinity have very long dissociation times. Therefore, in order to be able to measure association and dissociation constants accurately, it is fundamental to have a system that is stable in time, for running 3-4h long experiments. To make an example, SPR systems are highly unstable: the laser alignment varies incredibly with environmental factors such as vibrations and temperature (Wu et al., 2003).

The IRIS system is a very robust platform, mostly insensitive to vibrations and temperature shifts, and its long term stability primarily depends on robust optical setup and on the chosen light source. After a brief warm up period (10 to 30 minutes), LEDs reach thermal equilibrium and are usually stable for a long time (Della Corte et al., 2020). Moreover, ThorLabs LEDs have lifetimes of 100,000 hours. This gives potential to the IRIS platform to be an incredibly time-stable instrument.

In order to practically demonstrate this concept, we have performed a multiplexed, long dissociation experiment, where we flowed both DNA targets as well as high affinity, low-k_{OFF} antibodies across the surface of an IRIS chip functionalized with complementary probes. For these experiments, we immobilized both DNA and human IgG probes on the substrate. After spotting and blocking, we stabilized the surface of the chip with PBS for five minutes, then we ran the complementary molecules, an anti-human IgG at 20nM concentration, which bound to the IgG probes, and the surface probe-matching DNA sequence at 1μM, which obviously bound to the DNA probes. We measured the dissociation rate over three hours. The results of the experiment are shown in Figure 3·3a. As expected, DNA dissociation over the analyzed time period is negligible, while the antibody dissociation rate is accurately measurable, and was estimated to be $k_{OFF} = (1.317 \pm 0.002) \times 10^{-5}$ s^{-1} (blue fit line). In this case, the estimated association constant is $k_{ON} = (2.132 \pm 0.009) \times 10^{5}$ s^{-1}M^{-1} (red fit line), which leads to a value for the equilibrium constant of $K_d = k_{OFF}/k_{ON} = 61.8 \pm 0.4$pM. Figure 3·3b shows an inset of the measurement over one hour, the typical duration of a biosensing experiment with other techniques. As it can be observed in the graph, the dissociation of the antibody is almost negligible on such a short timescale, leading to inaccurate k_{OFF} measurements. Using the MATLAB curve fitting tool, we fitted the dissociation data on such time window, obtaining a similar but less precise result ($k_{OFF} = (1.58 \pm 0.01) \times 10^{-5}$ s^{-1}). Figure 3·3c shows the fitted dissociation curve on the entire 3h dissociation period.

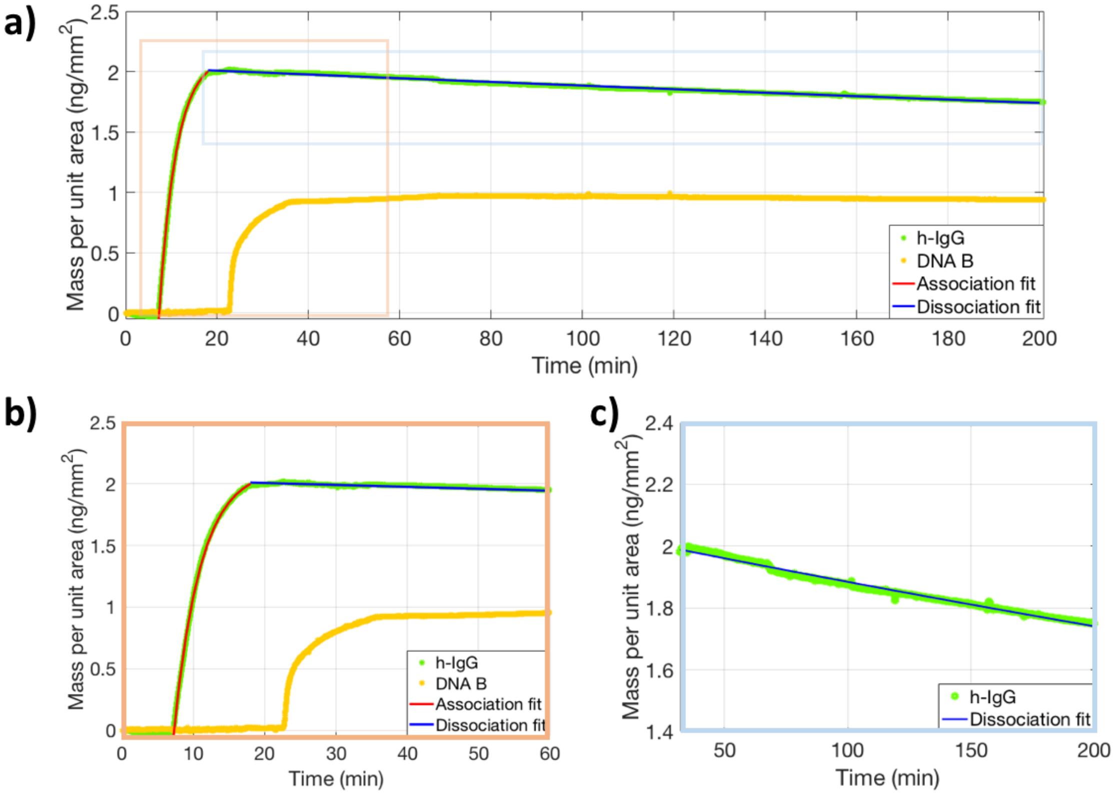

Figure 3·3: Multiplexed measurement of DNA and antibody binding kinetics on long dissociation timescales. Inset b) shows the curve cropped on a 60-minutes time window and c) shows the fitting of the antibody dissociation phase.

3.2 Four-color imaging and wavelength optimization

The working principle of the IRIS system is based on determining the thickness of a thin layered substrate by using light at different wavelengths. However, continuous acquisition at multiple wavelengths causes issues in terms of stability, since it requires LEDs to be turned on and off repeatedly. Additionally, fitting the multi-wavelength data points to the reflectance equation for each acquired image is computationally heavy, and storing multiple images for each time point is cumbersome, as well as affecting the time resolution.

In the past, our group has demonstrated that acquiring a single multicolor image at the beginning of the experiment is sufficient to create a reflectance look-up table, which can then be applied to single-wavelength data under the assumption that the increase in thickness generates a linear reflectance response at that wavelength (Sevenler and Ünlü, 2016). We have demonstrated that this method can be improved by using a color camera, as discussed below in Section 3.2.1.

The linearity assumption, however, is only valid for a certain biomass accumulation range, which depends on the wavelength used. For example, with blue wavelength (452nm) - the standard wavelength used for analog measurements - the assumption only applies for a total biomass accumulation value that does not exceed 10 nm in thickness - a condition that is satisfied for most proteins, antibodies and oligonucleotides binding to our sensor. The approximation though cannot be applied if the studied analyte is a vesicle or a nanoparticle, since such samples would form a much thicker layer on the sensor. Therefore, in Section 3.2.2 we will discuss how to optimize wavelength choice for detecting large analytes in an analog fashion.

Finally, in Section 3.2.3, we will talk about analog detection of spaced out nanoparticles and show the results from simulations using the Boundary Element Method (BEM) software.

3.2.1 Thickness measurements with color camera

For small molecule measurements, it is crucial to precisely know the thickness of the silicon oxide substrate, to perform bulk effect removal and to achieve sensitive measurements, as further detailed in Section 3.4.1. In general, estimating the thickness of the oxide layer is important in order to determine the exact amount of biomass accumulating on the chip surface. On the first generation of the IRIS, a multicolor image was acquired with four-color LEDs at each time point, so that the thickness d of the substrate could be precisely calculated for every reflectance datapoint. This method resulted in time-consuming acquisitions and was computationally heavy. Moreover, performing the thickness calculation at each datapoint is unnecessary once the initial thickness of the oxide is a known parameter of the measurements. As a matter of fact, calculating the biomass accumulation value from the reflectance values at a single wavelength is simple if the initial thickness is known and if the reflectance-biomass correlation is assumed to be linear, which is true for molecular binding (Δd<10nm).

More recently, the system was improved so that a single four-color image was acquired at the beginning of each experiment, which was then used to generate a look-up table for single wavelength reflectance-to-thickness conversion. Here, we propose an even more simplified version of that method, where a white light source substitutes the multicolor LED, and the sensor is a color (RGB) camera. With the proposed method, the thickness measurement is performed on a separate, very straightforward IRIS platform, which provides in-advance information on the substrate thickness; this allows for chip pre-selection when a particular oxide thickness is needed, for example for bulk effect free measurements.

The thickness measurement platform features the same optical path as the analog IRIS system, in a vertical configuration; a broad wavelength visible light source (white light); and a color RGB camera sensor (FLIR BlackFly BFS-U3-16S2C-CS). The white light source allows for faster and simpler acquisition: only one image per chip is needed, while four images were necessary with the single-channel sensor. Moreover, the exposure time is automatically adjusted and normalized by the RGB sensor at all wavelengths.

The software is a custom MATLAB plugin that takes the reflectance RGB values and then utilizes the reflectance equation to calculate the thickness of the oxide (Eq. 2.7). Figure 3·4 shows a picture of the system as it is now. The white light source has not been incorporated yet, instead the platform is currently utilizing multicolor LEDs that are all being turned on at the same time.

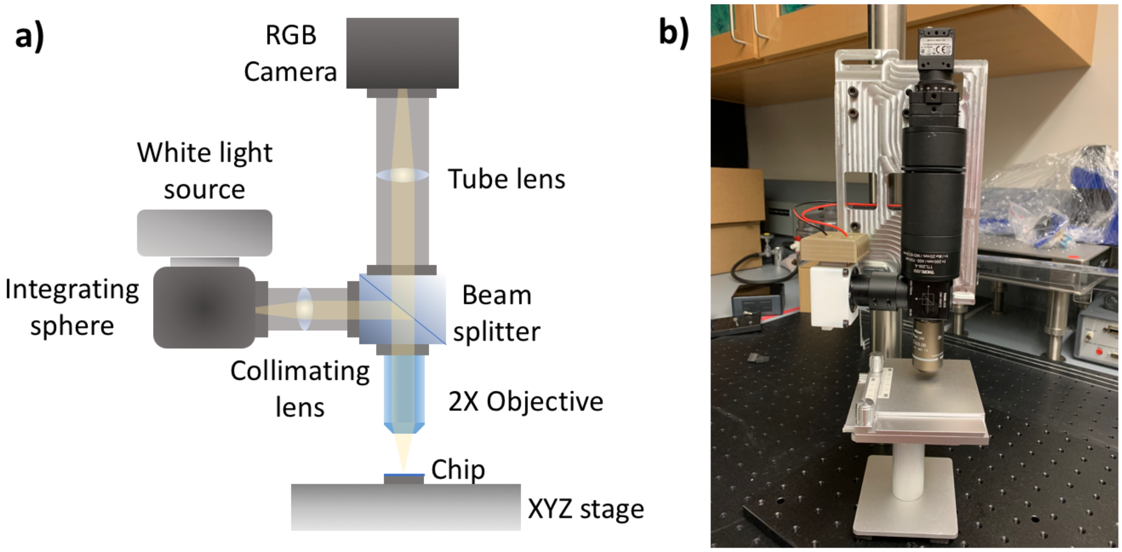

Figure 3·4: The chip thickness measurement platform. a) A graphical scheme of the optical path and components and b) a photograph of the physical instrument.

3.2.2 Wavelength simulations for large analytes

Large analytes such as biological nanoparticles (BNPs) can be complex to study at an analog level. The reason for that is the heterogeneity in their structure and size, which results in a 'rough', non-uniform layer of biomass on the surface of the sensor. Small extracellular vesicles (SEVs) are a collection of bi-lipidic membranous BNPs that range in size between 30-100nm, and in order to study their kinetics we have employed the analog IRIS sensor as detailed in Section 4.2.1.

The standard wavelength utilized to measure biomass accumulation on the IRIS is blue (452 nm). The reason for this choice is that reflectance at blue wavelength has the maximum variation for small amounts of molecular binding, that is, it is the wavelength that provides the most sensitive measurements. However, when the thickness increases above a certain value, this high sensitivity is partially lost: for thicknesses above 130nm (110nm SiO_2 + 30nm accumulated material), the derivative of the reflectance curve at blue wavelength gets closer and closer to zero, meaning that for increases in thicknesses there will be a very small increase in signal. Therefore, it is not the ideal wavelength when it comes to studying large analytes.

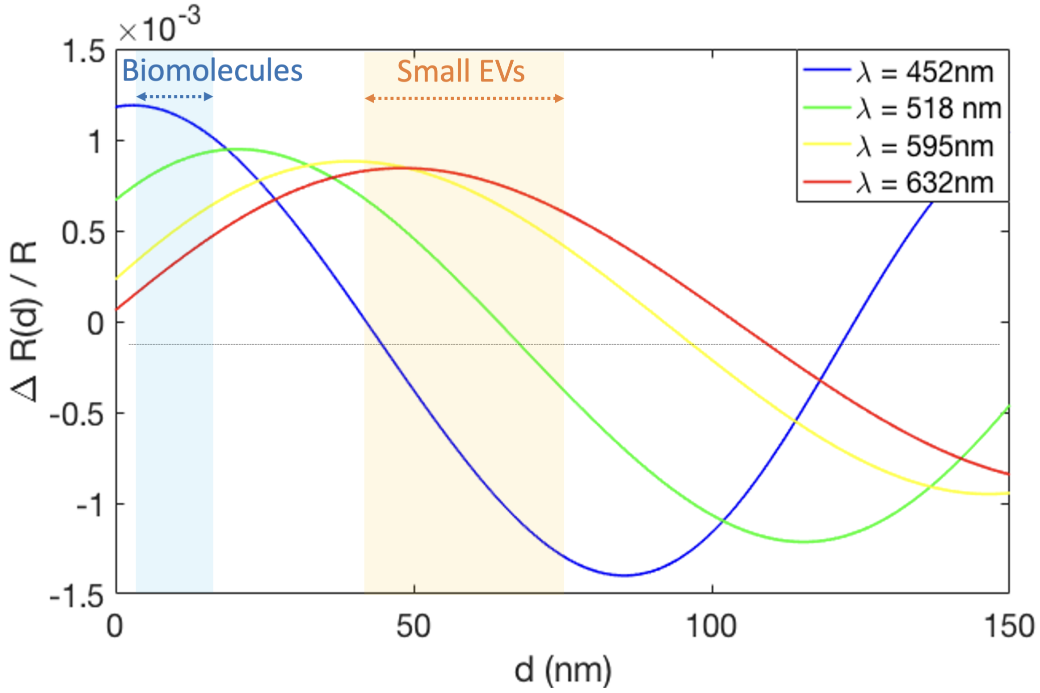

Figure 3·5: Simulations of the change in reflectance for increasing amounts of biomass accumulation on an IRIS chip, at the four wavelengths corresponding to the center wavelengths of the employed LEDs.

Simulations shown in Figure 3·5 demonstrate that green wavelength (center $\lambda =$ 518nm) is the best choice for studying larger analytes at the analog level, particularly small extracellular vesicles (SEVs), whose size range is between 30-100nm, with the majority of them concentrated in the range 40-70nm (Section 4.2.1, Figure 4·9). Indeed, Figure 3·5 shows that, for green wavelength, the increase in reflectance with biomass accumulation is positive for larger thickness values: the derivative of the reflectance equation is larger than zero for biomass accumulation values up to 64nm, with respect to blue (center λ=452nm), where it's positive only up to 42nm. This result demonstrates that a better signal to mass density correlation can be obtained for large analytes such as EVs when using green LED light.

3.2.3 Nanoparticle scattering simulations

As discussed above, one of the conditions for visualizing the signal produced by nanoparticles at the analog level, in most cases, is to obtain a uniform carpet of particles captured on the sensors' surface. This only happens under precise conditions - high particle concentration in the sample, low steric hindrance. Here, we will aim to study gold nanoparticle complexes (GNPs) at the analog level. The motivation for these studies arises from the possibility of simulating real-time lateral flow assays, as well as to study the behavior of complex analytes, such as antibody-particle complexes (mAb-GNPs), as we mentioned in Section 1.2.3.

However, reaching the condition of capturing a full carpet of mAb-GNPs on the surface of an IRIS chip is in practice very challenging: the concentration of the particles must be very high ($>10^{1}0$ part/mL), which in most cases is impossible due to the small amount of sample available. Moreover, surface probes' conditions have to be optimized and steric hindrance must be minimized. As shown in the Results Section 4.3, at the tested concentrations, GNPs were never observed to form a full carpet, always keeping a minimum of one-nanoparticle distance between one another. A reason for this behavior might reside in the combination of polymer and antibody molecules that coat the GNPs' surface, causing steric hindrance and repulsion, resulting in a larger average distance between particles.

However, the scattering signal produced by gold nanoparticles is large, specifically, it is orders of magnitude larger than that produced by EVs or other biological nanoparticles. Thus, while in the case of EVs a full NPs carpet was needed in order to measure an analog signal, it is possible that for GNPs such condition might not be necessary. In other words, we studied the possibility of measuring the analog signal produced by GNPs that accumulate without fully covering the surface. Particularly, we aim at maximizing constructive interference by studying the dependance of the measured intensity on the thickness of the oxide layer, the numerical aperture of the system and the average distance between the particles. In the following paragraphs, we will show simulation results obtained with the MATLAB toolbox MNPBEM, which we used to simulate the signal produced by single gold nanoparticles in a two dimensional space on our sensor.

Illumination wavelength should be the first parameter to be discussed. However, we have already determined in the previous section that the best illumination wavelength for large analytes is green, therefore we will fix the value of $\lambda = 518$nm and we will begin our discussion with some considerations regarding the thickness of the oxide layer. Experiments for detecting mAb-GNPs complexes on the h-IRIS system have to simulate sandwich assays, where a protein is captured by the active sensor first, then a mAb-GNP complex binds to the captured target. Thus, the chosen oxide thickness must work for detecting signal produced by accumulated molecules as well as nanoparticles. For analog measurements of biomolecules, the best thickness has been determined to be 110nm of oxide. On the other hand, for single particle detection, the chosen thickness is usually 60nm of oxide, because it provides the maximum NP-background contrast (Yurdakul, 2021). In order to determine if one of these thicknesses would work for hybrid experiments, we have simulated the contrast generated by a single 80nm GNP on an IRIS chip with various oxide thicknesses. The results of the simulations are shown below in Figure 3·6. The surrounding medium was assumed to be PBS, which is the standard buffer used in the experiments (n = 1.335).

As expected, simulations show that the best contrast ($S_{max} - S_{min}$) is achieved for 60nm of SiO_2. However, the signal generated on 110nm of SiO_2 is still high, and the

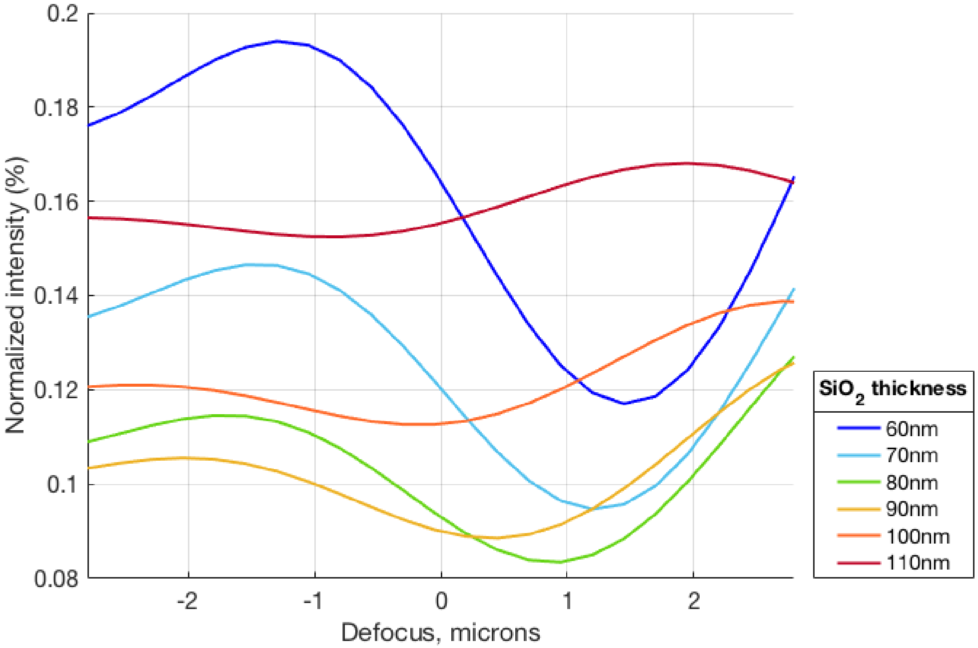

Figure 3·6: Simulations of the signal produced by a single GNP captured on the surface of an IRIS chip, assuming an elevation of 10nm from the surface (polymer and capture probe), for a range of oxide thicknesses.

contrast is not excessively low, enabling digital measurements. Therefore, 110nm of SiO_2 could definitely be a fair choice for both analog and digital detection of GNPs.

Next, we verified how the measured scattering signal changes when varying the numerical aperture of the system. Figure 3·7 shows the loss in resolution when moving from NA=0.7 (Figure 3·7a) to NA=0.45 (Figure 3·7b) for digital detection of a single gold nanoparticle. Here, the conditions are the ones described above (PBS buffer medium, particle elevated 10nm above the surface of a 110nm SiO_2 IRIS chip), and the simulated illumination is at green wavelength (λ = 518nm). The particle is shown at the focal position that yields the maximum contrast. Despite the loss in resolution at the edges, the particle is still clearly resolvable with 0.45 NA, justifying the use of a 0.45 NA, 20X objective for digital detection on the h-IRIS. Moreover, in Figure 3·7c, the signal produced by a single particle in the analog configuration is shown (NA=0.15). As expected, the contrast is incredibly low, and the particle is non resolvable. Additionally, the reflectance does not change when varying the focal position.

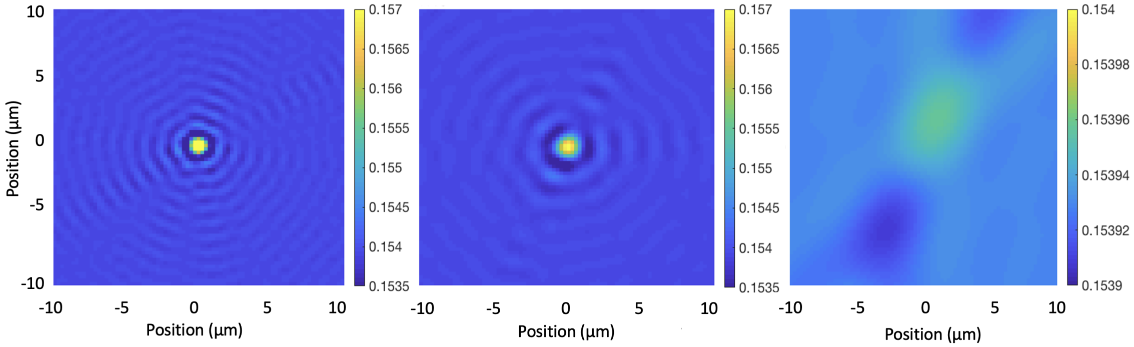

Figure 3·7: Simulations of the signal produced by a single GNP captured on the surface of an IRIS chip for different numerical aperture values: a) NA = 0.7 b) NA = 0.45 c) NA=0.15. The color axes indicate the total scattered signal ($S_{scat} + S_{ref}$).

We then simulated several particles on the surface of a 110nm-SiO_2 IRIS chip, to study the constructive interference generated by neighboring particles. In order to mimic a real GNPs binding experiment, we simulated a relatively large area ($0.16mm^2$) on the IRIS chip, and distributed numerous GNPs on the surface in a random configuration. In order for these simulations to be realistic, a large number of particles needs to be considered: our best estimate, from experimental results is between 5000-50'000 part/mm^2. Using the BEM tool, it is possible to simulate the signal produced by each of the particles individually at a different position, randomly chosen inside the selected area. However, simulating such a large number of individual particles is computationally very heavy. Thus, we assumed all GNPs to be identical, and - under this assumption - it was possible to calculate the electric field generated by a single particle, then move the particle across the image, in different positions, recursively summing the scattered electric fields.

We started by simulating the electric field generated by a single particle placed in the center of a 400μm^2 square on the surface of the IRIS chip. We made sure the scattered field dropped to zero at the edges, to avoid border artifacts. Then, we created a 0.16mm^2 (160,000μm^2) dark image where we randomly positioned the single-particle matrix, summing the generated electric field at each iteration, with an exclusion condition on occupation of the same pixels. Finally, we calculated the total measured intensity by taking the square modulus of the sum of the scattered and reference field. When positioning 1000 particles in such area, the particle density is 6000part/mm^2. We simulated this condition for the two numerical aperture values used for digital (NA $=$ 0.45) and analog (NA $=$ 0.15) detection, and the result is shown in Figure 3·8. The figure was cropped to a smaller 0.04mm^2 area in order for the particles to be more visible. These simulations are a good approximation of experimental data, and again show how the numerical aperture affects the resolution of the acquired image, as well as the amount of measured signal. Despite that, however, they also demonstrate that it is still possible to visualize the intensity generated by non-adjacent particles as a collective scattering signal, justifying analog measurements at low NA.

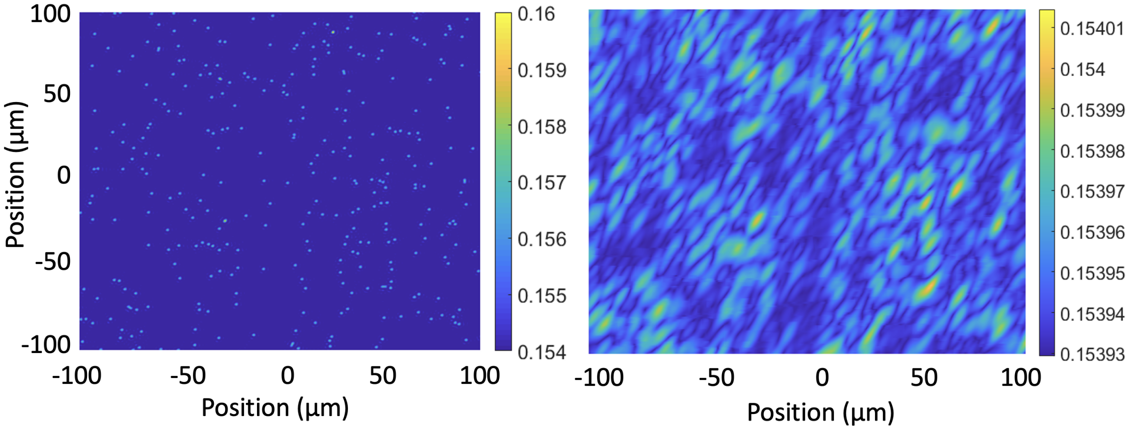

Figure 3·8: Simulations of the signal produced by 6000 GNPs/mm^2 captured on the surface of an IRIS chip for a) digital (NA=0.45) and b) analog (NA=0.15) detection on the h-IRIS platform. The color axes indicate the total scattered signal ($S_{scat} + S_{ref}$).

Furthermore, if the number of particles on the surface is increased, the relative distance between them will drop. This increases the amount of signal measurable in analog conditions. Below, in Figure 3·9, an example of the analog signal measured when 60,000 GNPs/mm^2 are accumulated on the simulated surface. The surface density of particles shown in Figure 3·9 is very close to the highest density that is obtainable experimentally. The results from these simulations will be compared to experimental data acquired on the h-IRIS system in Section 4.3.

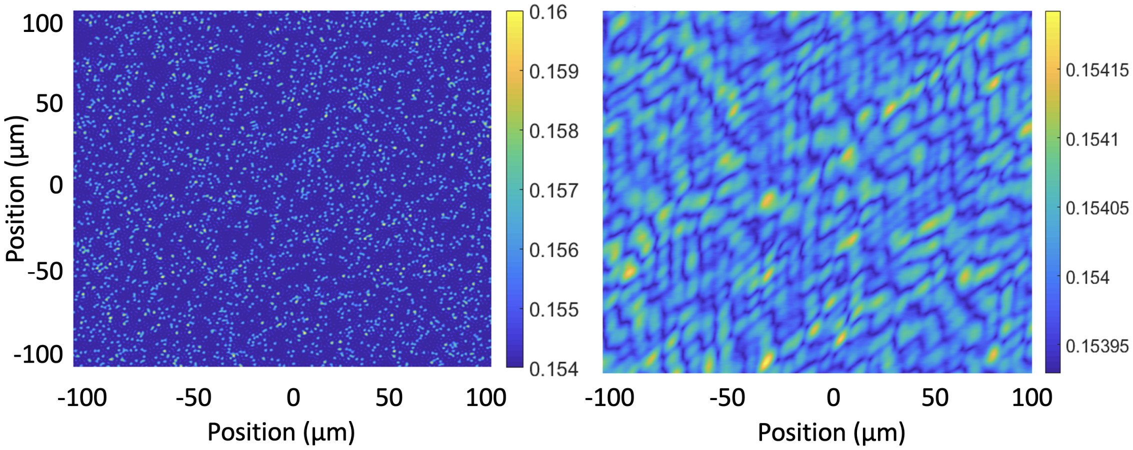

Figure 3·9: Simulations of the signal produced by 60,000 GNPs/mm^2 captured on the surface of an IRIS chip for a) digital (NA=0.45) and b) analog (NA=0.45) detection on the h-IRIS platform. The color axes indicate the total scattered signal ($S_{scat} + S_{ref}$).

On the same note, one can simulate how the measured analog signal would increase with particle density. This might be non-trivial since we are considering a combination of constructive and destructive interference, as it can be observed in Figures 3·9b and 3·8b. Hypothetically, if the impact of destructive interference was negligible, the signal would increase linearly with particle accumulation, then saturate when no more binding sites are available. Indeed, if we plot the average analog normalized signal calculated for a particle density increasing from 600 to 120,000 GNPs/mm^2, we notice that the signal increases monotonically with the particle density, as shown in Figure

3·10. This can also be observed when looking at the simulated analog images on the same color scale (Figure 3·11). These results confirm once again the potential of the h-IRIS system to detect and quantify the analog signal generated by single scatterers.

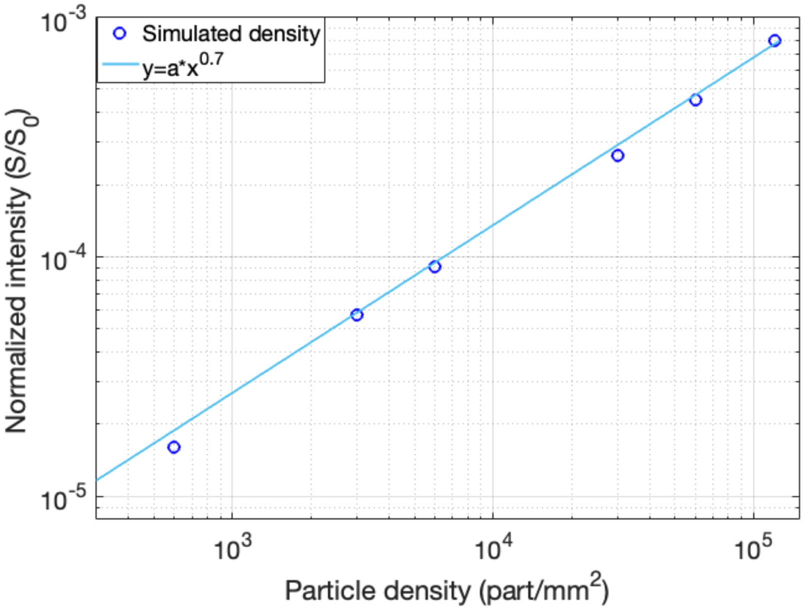

Figure 3·10: Simulations of the average normalized signal (scattering signal/reference signal) produced for increasing GNPs density on the surface of an IRIS chip, in analog detection mode. The signal is plotted on a log-log scale and is fitted with the equation $y = a \times x^{0.7}$.

3.3 Illumination uniformity

As we strive for higher sensitivity, we have to consider the impact of illumination artifacts on our system. In a shot-noise limited system, since the noise level depends on the measured signal, variation of the illumination intensity across the imaged surface causes spatial-dependent noise - the spots in the darker region of the surface will be subject to a higher level of noise with respect to those in a better illuminated area.

So far, we have presented two different illumination schemes: critical illumination,

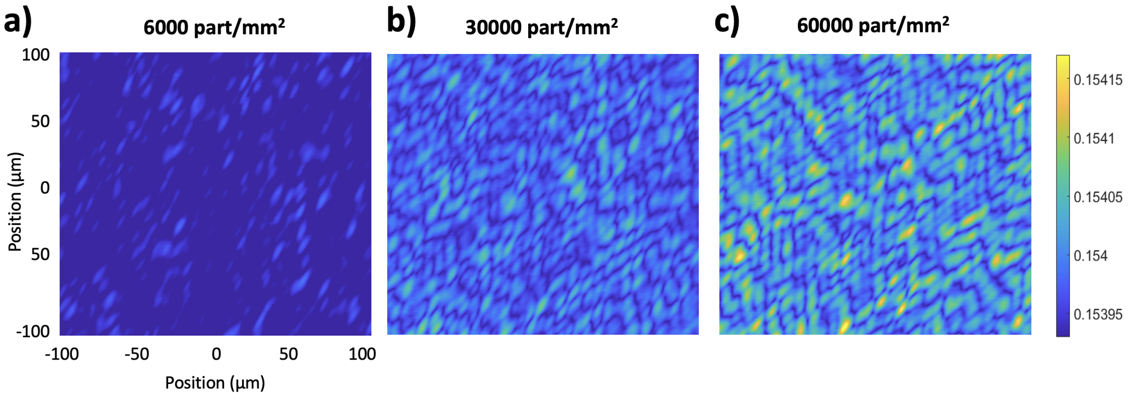

Figure 3·11: Simulations of the average total signal ($S_{tot} + S_{ref}$) produced by increasing GNPs density accumulating on the surface of an IRIS chip, in analog detection mode, for a) 6000 GNPs/mm^2 b) 30,000 GNPs/mm^2 c) 60,000 GNPs/mm^2.

which is the direct focusing of the source on the sample plane, and Köhler illumination, where the source plane is conjugated with the back focal plane of the objective. It has been demonstrated that Köhler illumination improves illumination uniformity in digital configuration, since it provides a source-free image. However, when using for example a 2X objective in full NA illumination mode, the maximum aperture of the integrating sphere is smaller than the back aperture of the objective, resulting in a bright spot in the center. Therefore, for analog measurements, Köhler illumination is not ideal.

In order to achieve both analog and digital measurements on the same system, we had to compromise on the illumination scheme. We compared the efficiency of both schemes; we chose to implement a Köhler scheme, since it has a sensible impact on the contrast of single nanoparticles, and for what concerns analog, the difference in terms of illumination uniformity is negligible with respect to critical illumination, as reported below (Section 3.3.1). However, there is room for improvement, and we are developing new optical design ideas that will improve the uniformity of the illumination across the surface.

3.3.1 Comparison of critical and Köhler illumination schemes and the impact of pixel-to-pixel variation

In order to determine the impact of illumination artifacts on our measurements, we acquired 2X images of the surface of an IRIS chip with both the standard analog system (critical illumination) and the h-IRIS (Köhler illumination). We then plotted the illumination profile, obtaining a gaussian profile in both cases, as expected. The profiles are shown in Figure 3·12a. Köhler illumination (green line in Figure 3·12a) plays a role in having a brighter center on the h-IRIS setup. Despite this, however, the two profiles are not extremely different, confirming that choosing Köhler illumination would most probably not influence analog measurements significantly. The slightly higher signal measured in critical configuration (yellow line in Figure 3·12a) is probably due to the fact that the source is focused on the sample plane, therefore more light is collected. However, the difference is negligible. Moreover, on the h-IRIS, analog measurements are usually performed with a 5X objective; the illumination profile obtained with the 5X objective is shown in Figure 3·12b. It can be observed the profile obtained with the 5X objective results more uniform, and clearly the higher magnification has an impact, reducing the field of view and thus making border effects less visible.

When sectioning the image along a line that contains microarray spots, the profile of the spots will be convoluted with that of the illumination. They are still clearly discernible, as shown in Figure 3·13, however both the measured signal and the background slightly vary depending on the spot position. One way of minimizing the impact of the illumination on the acquired data is then to perform differential measurements, where a donut-shaped region around the spot acts as a background. This ensures that illumination of the background is similar to that of the enclosed spot.

Additionally, we are working on the design of novel light integrating devices that

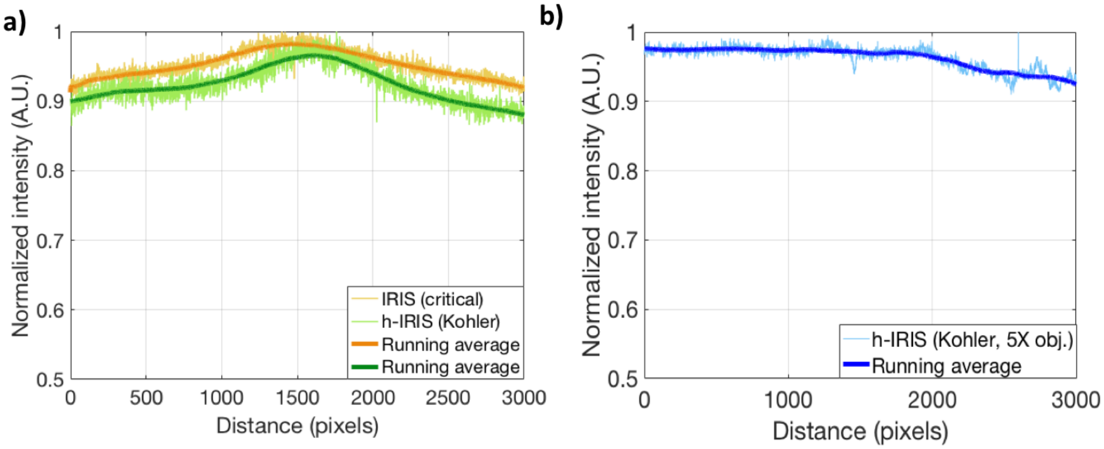

Figure 3·12: a) The illumination profiles obtained on the analog IRIS system with critical illumination (yellow) and on the h-IRIS system with Köhler illumination, with a 2X objective. b) The illumination profile obtained on the h-IRIS system with a 5X objective.

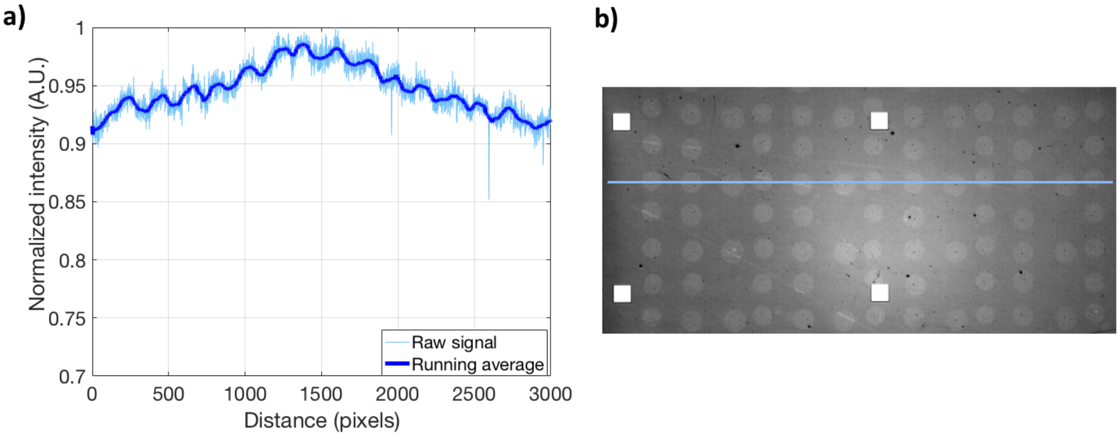

Figure 3·13: a) The light profile obtained on the IRIS system when sectioning a microarray image along the line shown in b) containing 200μm sized spots.

will provide major improvements to the illumination uniformity and increase the total light intensity delivered to the surface of the chip, leading to more consistent, more sensitive analog measurements.

Finally, it is important to observe that when using a color camera to measure the thickness of the chips, one pixel on the color camera is divided into smaller pixels, corresponding to different channels (R,G,B). Since the RGB value will then be used to calculate the reflectance curve, it is crucial to demonstrate that the standard deviation between adjacent pixels is minimal. We plotted the profile obtained by selecting ten adjacent pixels in the center of the image (Figure 3·14), and realized that the noise/signal ratio is 0.009 = 0.9%, which can be considered negligible if an average of few pixels is taken into consideration when making the thickness calculation.

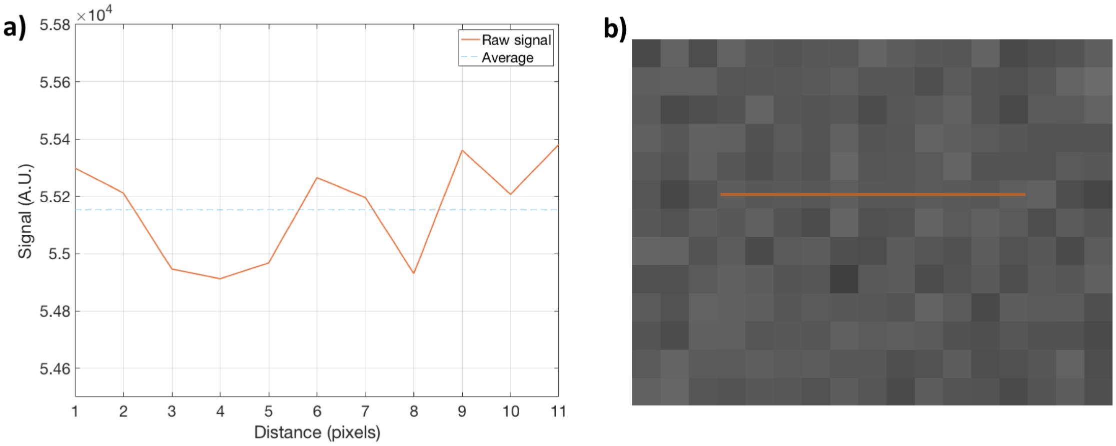

Figure 3·14: a) The signal variation measured on the IRIS system when considering 10 adjacent pixels, along the orange line shown in b). The average value is shown as a dashed blue line.

However, when performing digital measurements, a 0.9% error between adjacent pixels can be relevant: one particle only occupies a few pixels when imaged in a single particle detection experiment. It is therefore important to minimize all sources of noise for single particle imaging, including fabrication noise which can generate a physical pattern on the sensor's pixel and therefore affects the particle imaging sensitivity.

3.4 Solution effects

One of the main causes of artifacts in label-free biosensing resides in the optical properties of the utilized solutions. Most label-free biosensors measure the change in refractive index at an interface, and correlate such change with an increase or decrease in biomass accumulation. However, variations in the refractive index of the surrounding medium can also generate a signal, causing confusion when interpreting binding data. This occurrence is referred to as the *bulk effect.* Organic solvents such as methanol or dymethyl sulfoxide (DMSO) are the main agents responsible for this effect, since they are often utilized to dissolve low molecular weight compounds that are insoluble in water, and their refractive index is very high with respect to commonly used running buffers such as phosphate buffer saline (PBS).

When a high refractive index solution comes in contact with the interface of an optical-based biosensor, an artificial jump in signal is recorded. There are several possible methods to eliminate this artifact from binding data. In order to prevent it, one could perform 'buffer matching', where the running buffer is matched as closely as possible in composition to the sample solution. Even so, sometimes, the very presence of the target molecules is what causes most of the bulk RI change, making buffer matching quite useless. Some sensors, such as SPR, utilize a blank channel, that is, an unfunctionalized channel where the same exact solutions are flowed at the same time as the active channel, then perform a differential measurement. This is a pretty straightforward method, yet, if the conditions of the two channels are not exactly the same, an artifact could still occur.

In the next section we will briefly describe a simple method that has been applied to IRIS measurements in order to completely remove the bulk effect. Then, we will discuss an alternative method, which is less rigorous but can be more easily implemented.

3.4.1 Bulk effect elimination method

The IRIS platform bases its sensing principle on thin-film reflectance. When biomaterial accumulates on the surface of an IRIS chip, the reflectance spectrum shifts, and, thanks to constructive interference, an increase in signal is generated at a particular wavelength. As explained in Section 2.1, usually an IRIS measurement starts by acquiring a multi-wavelength image of the substrate, which is then subsequently fitted to the reflectance equation to extract a look-up table. The look-up table correlates changes in reflectance with changes in thickness of the oxide layer. However, when the refractive index of the surrounding solution varies, the reflectance curve also undergoes a change: as it can be deduced from Equations 2.7 and 2.8, variations in the medium refractive index cause the curve to shrink along the y-axis.Figure 3·15a compares the bulk effect-related change in reflectance to that generated by biomass accumulation.

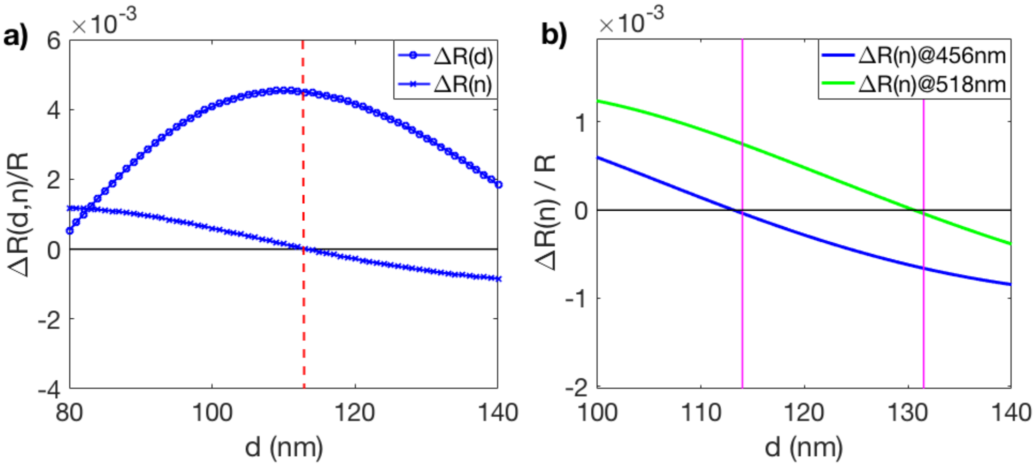

Figure 3·15: a) The signal generated on the analog IRIS system by biomass accumulation (circle markers) and by bulk effect (cross markers) with blue LED illumination. The red line indicates the bulk-effect free thickness at 113nm. b) The signal generated by bulk effect with blue and green LED illumination. When the thickness of the substrate resides between the two purple lines, blue and green LED light can be utilized simultaneously to eliminate the bulk signal.

We have demonstrated that, for every thickness of the oxide layer, a particular wavelength exists for which the reflectance signal is insensitive to bulk changes and only responds to thickness variations. For a substrate thickness comprised between

d=113 and d=132nm, such wavelength resides on the spectrum between λ=452nm and λ=518nm, which are the peak wavelengths of the blue and green LEDs used (Figure 3·15b). Thus, we have experimentally shown that a precise combination of green and blue light can be used as illumination source in order to achieve bulk-effect free measurements in the presence of a solution containing 1%DMSO, with small molecule sensitivity (Marn et al., 2021a). To compare, on SPR, a solution of 1%DMSO causes a bulk signal that is hundreds of times larger than that of small molecules (Schasfoort, 2017).

The implemented method, however, has some drawbacks: it requires two LEDs to be turned on at the same time, which can cause overheating. Alternatively, they can be powered on sequentially one at a time, which can, on the other hand, cause instability. Moreover, the bulk effect free wavelength changes depending on the thickness of the chip: this would not be a big issue if chip fabrication process had a small error on the thermally grown layer, however, that is unfortunately not the case. Chips with a nominal thickness of 110nm of thermally grown oxide suffer from a 10% variation in thickness from one wafer to another, and 5% error across the same wafer (these accuracy data were provided by our vendor, Silicon Valley Microelectronics - SVM). Consequently, the bulk-effect free wavelength has to be determined every time a new chip is utilized, requiring a calibration step with known refractive index solutions. This can be cumbersome and time-consuming, with a potential to affect the spotted molecules if they are particularly delicate.

Hence, we have decided to implement a new process in order to prevent bulk effect from affecting our measurements: since the bulk effect free wavelength varies with the substrate thickness, we have calculated the substrate thickness which corresponds to bulk-free operation at the center wavelength of our blue LED. The bulk-effect free thickness is 113nm, as shown in Figure 3·15a by the red dashed line. Thus, instead of adapting the wavelength to a certain chip, we have chosen to adapt the chip to a certain wavelength. Before preparing a chip, the thickness is precisely measured with the color camera setup described above (Section 3.2.1). If the thickness is very close to 113nm, the chip is then prepared and used. Otherwise, it is saved and utilized for other experiments. This is the advantage of this method and of developing a versatile platform: since not all measurements are affected by bulk artifacts, but mostly small molecule kinetics experiments that require high percentages of solvent in the solution, the excluded chips can be used for other applications. This method reduces the amount of time and effort to produce bulk-effect free data, and ensures consistency across all experiments.

3.5 Surface chemistry

One of the disadvantages of label free biosensors is the fact that one of the two molecular reacting partners (the probe) needs to be attached to a surface, namely the sensor itself. This is obviously less trivial with respect to reactions that are carried out in solution, where both partners are free to wander around and explore various configurations in order to bind. When the probe is anchored, the part closer to the surface will be harder to reach for the analyte molecules: therefore, if the active binding site on the probe is too close to the surface, it will be hindered and the analyte will not be able to bind. Steric hindrance caused by the presence of other probe molecules can also be a cause of less efficient binding: the congestion caused by the physical presence of the surrounding ligands can diminish the binding efficiency due to the fact that some binding sites might be unreachable by the analyte molecules.

Moreover, immobilizing a molecule requires the application of a slight pulling force on its structure, which can cause it to bend and distort, thus causing denaturation and loss of reactivity. While oligonucleotides also suffer from interaction problems related to 'laying flat' on the surface, this issue mostly regards proteins, where structure and functionality are closely related. Some proteins are more prone to denaturation than others: those are referred to as *soft* proteins, which relates to the number of disulfide bonds present in their structure (Faccio, 2018). While *hard* proteins contain a high number of disulfide bonds per molecule (a good example is bovine serum albumin - BSA, with seventeen disulfide bonds), soft proteins contain less, and are therefore more easily deformable. An example of a soft protein is α-lactalbumin, with only four disulfide bonds. Most immunoglobulins (IgG) also are considered soft, which is relevant considering that IgGs are very often used as probes for biological assays.

In this regard, surface chemistry development is a research field whose goal is achieving efficient immobilization of biomolecules onto a rigid substrate, while maintaining a uniform surface morphology. The functionality of biosensing substrates, particularly microarrays, is strongly dependent on the structure of the surface, which can influence both the sensitivity of the measurements as well as the reactivity of the probes. For example, for digital detection of nanoparticles, surface roughness could disguise the particles, impacting the measured contrast and therefore the detection capability. On the other hand, for all specific molecular assays, both analog and digital, it is fundamental that the probes maintain their molecular structure in order to keep their native functionality. Moreover, they need to be spaced and distributed enough that the target can easily reach them. Maintaining a specific orientation of the probe molecules is also helpful in order to maximize binding (Trilling et al., 2013).

Many different approaches are utilized for this purpose, from coating the surface with epoxisilane-based polymeric thin films (Nimse et al., 2014; Seurynck-Servoss et al., 2007) or with matrix-structured polymers whose tridimensional properties can contribute to preserving the structure of the molecules (Pirri et al., 2004; Chiodi et al., 2022). Another interesting approach utilizes nanostructures (Kim et al., 2008), a method that allows for specific control of the wettability of the surface (Khranovskyy et al., 2012; Tsougeni et al., 2018).

As another example, SPR sensors utilize thick hydrogel matrices in order to improve the probe density and increase the binding signal. However, these dense polymeric matrices cause diffusion effects, which in turn contribute to generate artifacts in the measured binding constants (Drake et al., 2012). SPR software for data analysis have developed diffusion-influenced kinetic models in order to remove the contribution given by mass transport limitation: however, the correction they provide is still inaccurate, due to the fact that - in the best of cases - they utilize a first order correction with a two-compartment model, which is not representative of the real diffusive processes happening in the matrix. This topic will be further discussed in Section 3.5.3. Some common functionalization methods are summarized and graphically represented in Figure 3·16.

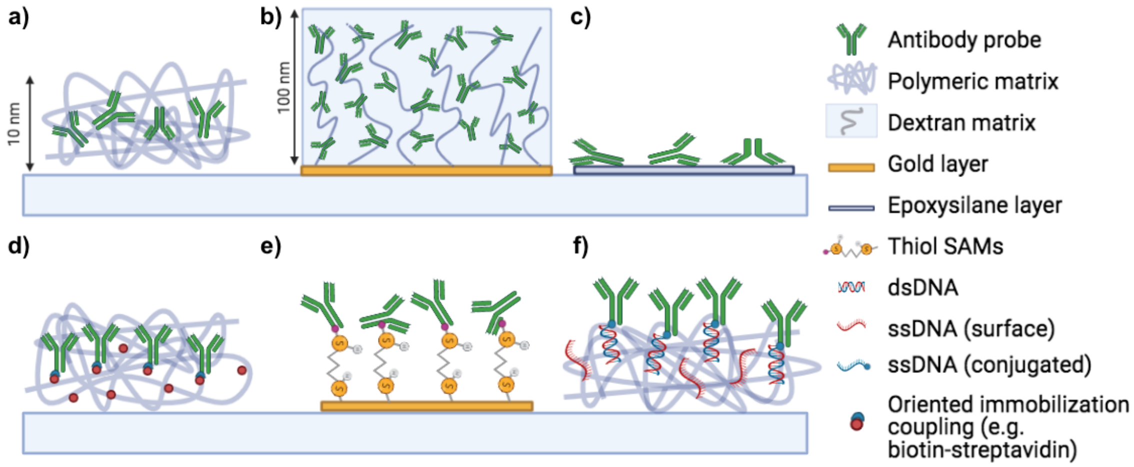

Figure 3·16: Graphical representation of some of the most common surface chemistry functionalization methods. a) Copoly(DMA-NAS-MAPS) developed by Chiari et al. (Pirri et al., 2004) b) Dextran matrix typically utilized for SPR c) Epoxysilane d) Biotin-streptavidin on copolymer e) Thiol-gold SAM linkage f) DNA-directed oriented immobilization.

Our approach utilizes a soft, hydratable and anti-fouling polymeric coating that has been developed and optimized for creating a single layer of molecules on the surface of the sensor. The polymer is approximately 2 nm-thick when dry, and 10 nm-thick when hydrated (Yalçın et al., 2009). Its ability to hydrate and create a thin tridimensional layer allows the molecules to maintain their structure, avoiding denaturation. The polymer has been developed by Chiari et al. (Pirri et al., 2004) and is a N, N-dimethylacrylamide (DMA) with N-Acryloyloxysuccinimide (NAS) and 3-(Trimethoxysilyl)propyl methacrylate (MAPS) based polymer which forms a thin film on different materials by a combination of physi and chemisorption. This copoly(DMA-NAS-MAPS) is commercially available under the name of MCP-2, and in an effort to taylor surface properties, it has been recently modified by introducing various building blocks to create different functionalities such as - for example - azide, alkyne, dibenzocyclooctine, maleimide moieties. This has been achieved by exploiting the reactivity of NAS with amino groups, which has enabled its transformation into other functional groups by post polymerization modification (PPM) reactions. The common backbone of DMA and MAPS shared by all polymers in the family confers them adhesive properties on a variety of surfaces.

In the following Sections, we will explore the effect of surface chemistry on reaction kinetics, probe immobilization efficiency and diffusion. We will start by presenting the microarray preparation protocol that has been utilized for most of the experiments narrated in this dissertation, from chip cleaning to insertion into the IRIS system. Then, we will describe an innovative technique that we recently developed to analyze multiple surface chemistry approaches simultaneously. Finally, we will briefly discuss the impact of diffusive effects on kinetic measurements and how to minimize the impact of mass transport with thin tridimensional coatings.

3.5.1 Standard microarray preparation

The IRIS platform is a surface-based biosensor, which therefore requires an active substrate accommodating the probe molecules, while the analyte molecules will be dissolved in solution and then flowed across the surface. As mentioned in Section 2.1, our active substrate is a Si/SiO_2 chip, 12.5mm wide x 25mm long. Chips are supplied by Silicon Valley Microelectronics (SVM) in pre-cut wafers coated in photoresist film and with laser-drilled inlet and outlet holed for fluidics measurements. In order to remove the photoresist coating, chips are placed in a glass petri dish, then a 5M solution of sodium hydroxide (NaOH) is poured on top. The chips are swirled for a couple minutes in the NaOH solution, then rinsed in NanoPure water and dried under nitrogen stream.

To coat the chips in MCP-2 polymer, they are oxygen plasma activated for 10 minutes and subsequently immersed in an aqueous solution containing the polymer (1%, w/v MCP-2 in 20% saturated ammonium sulfate) for 30 minutes. Afterwards, they are washed with NanoPure water and again dried under nitrogen stream. Finally, to complete the dip-and-rinse coating procedure, they are dried in a vacuum oven at 80°C for 15 minutes. At the end of this procedure, chips are ready to be spotted. Spotting can be performed using a robotic spotter (M2 iTwo Precision Liquid Handler) or by hand, utilizing a simple pipette tip (Celebi et al., 2020). Spotting of antibodies and proteins was always performed at 70% humidity, while DNA spotting can be handled at lower humidity levels, usually around 65%.

The spotted chips are then incubatet overnight in a NaCl saturated humid chamber. Finally, a one-hour blocking step with a 50mM ethanolamine solution (pH=9) is performed to inactivate the residual amine groups on the surface. After blocking, the chip is washed with PBS and then quickly dipped in water, dried gently under nitrogen stream, and is ready to use.

3.5.2 Comparison of various surface chemistry methods

In an effort to determine the properties and immobilization efficiency of different polymers in the MCP family, we have engineered a new method to compare the performances of distinct surface chemistries on the same sensing substrate, on the IRIS system. Namely, we have utilized a robotic spotter to isolate several reactive polymers on different regions of the same chip. A simplified scheme of the technique compared to the standard flat coating approach is represented in Figure 3·17a and b.

Generally, in order to test multiple surface chemistries with a standard protocol, it is necessary to coat several chips, then immobilize molecules in a microarray modality on top of them, and finally run several experiments. The detail of this standard procedure will be described in the following section on microarray preparation (Section 3.5.1). Despite coating with MCP polymers being a much simpler process with respect to most of the other surface chemistry methods available, having to perform this process numerous times is still time consuming and expensive. Thus, we developed a technique which allowed us to localize 11 different reactive polymers on the same chip, then run a single experiment to determine both their immobilization capacity as well as the efficiency of the binding reaction for each of them. The polymers we evaluated in these experiments were amphoteric, positively and negatively charged polymers belonging to the MCP family, some of them containing succinimide esters, some were azide-modified.

Chip preparation for these experiments required spotting of pL-quantities of the polymer solutions, then co-spotting probe molecules in the same exact position. First, polymer solutions were prepared by diluting them up to 0.014% in water with sucrose monolaurate 0.01% w/v, Then, 400 pL of either native (on standard MCP) or DBCO modified (on azido-MCP) α-lactalbumin 1mg/mL were spotted on top. The spotted chips were incubated overnight in a NaCl saturated humid chamber, then blocked with

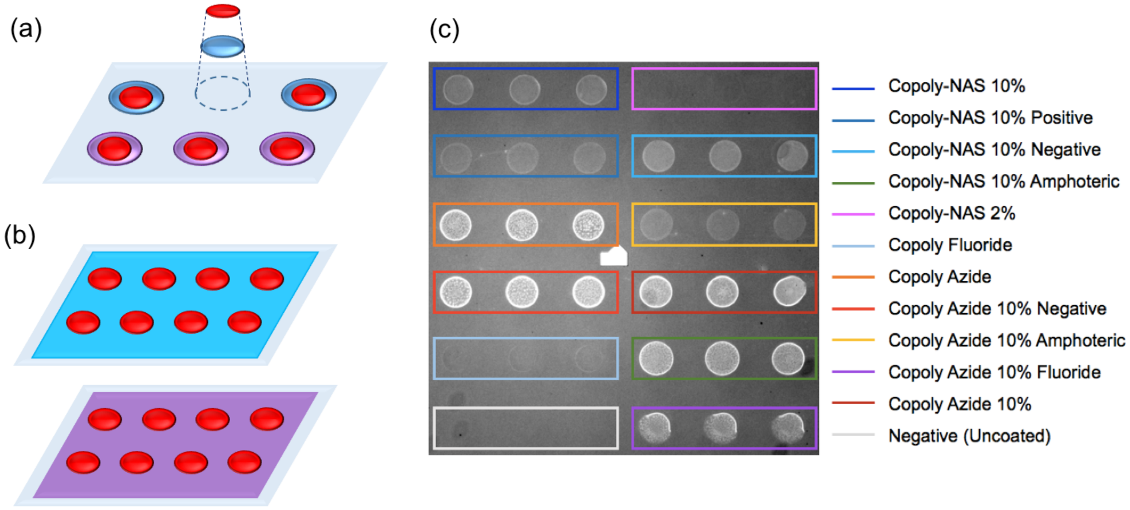

Figure 3·17: Left: a comparison of the localized chemistry technique (a) and the standard flat coating technique (b). Right: an example of an IRIS image of one of the chips utilized for the experiments. Reproduced with permission from (Chiodi et al., 2020b).

a 0.5% solution of ethylene propylene diene monomer (EPDMA) w/v in water for 15 minutes. This creates a polymeric layer surrounding the polymer spots, uniforming the surface of the chips. Finally, the chips were washed in DI water and dried under nitrogen, and they were ready to use. As described above, prior to starting the IRIS kinetic experiment, the chips were topped with an adhesive spacer and an AR coated glass slide to form a chamber for in-liquid measurements.

Chips were used to run an in-liquid IRIS experiment. An example of an IRIS image of one of the chips is reported in Figure 3·17, while an example of binding curves obtained during the experiments are shown in Figure 3·18. Filtered PBS buffer was initially flowed into the system for 15 minutes, to stabilize the surface. Afterwards, anti-α-lactalbumin antibody at 1ug/mL ($\approx$7nM) was injected for 20 minutes. PBS buffer was then injected again as a washing buffer for another 20 minutes. Finally, the surface was restored by flowing a 100 mM glycine solution at pH=2 for 5 minutes. The sudden pH change enabled fast debinding of the antibody molecules from the probes without damaging the probes. Each point of the curve in Figure 3·18 corresponds to one acquired image.

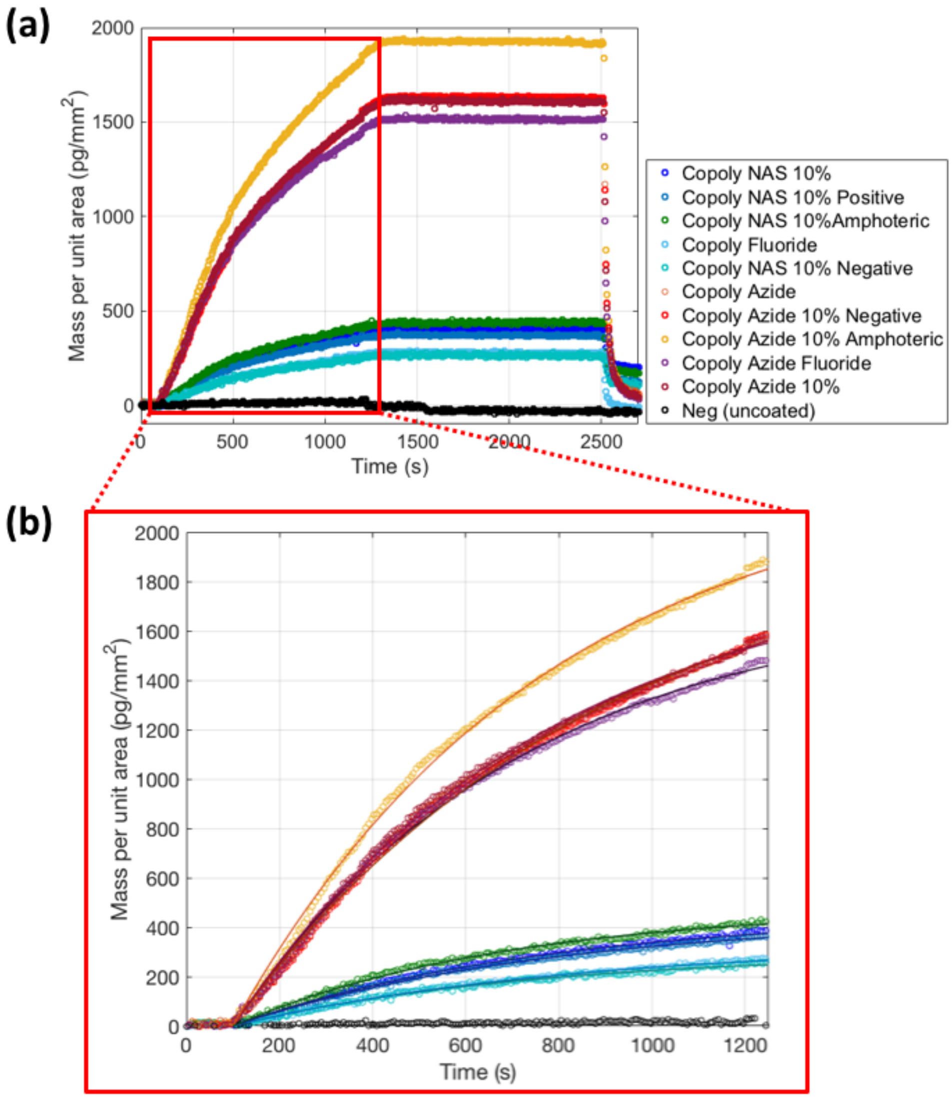

Figure 3·18: Binding curves obtained for the interaction of antiα-lactalbumin antibody with the target protein on the localized chemistry chip. Reproduced with permission from (Chiodi et al., 2020b).

As it can be seen from Figure 3·17, some polymers ensured better immobilization than others (brighter spots). We measured the accumulated mass and determined that the charged polymers were particularly efficient in immobilizing a large quantity of protein. However, when analyzing the binding rates, the more 'crowded' spots were not necessarily better at efficiently binding the antibody: this could be due to steric hindrance due to the high concentration of probes on the surface, or to electrostatic interactions between analyte and probe molecules due to the charged surface. Denaturation could also be caused by electrostatic attraction and repulsion of the probes. In the end, we have established that - for our purposes - a neutral chemistry was the best choice. With this technique, we also demonstrated characterization of differently-modified molecules on the same support.

3.5.3 Diffusion effects and mass transport limitation

Diffusion is a common cause of artifacts in kinetic measurements. In order to measure precise kinetic association constants, the analyte molecules need to be efficiently transported to the immobilized probe molecules by a fast flow. The flow needs to be fast enough that when molecules bind, the layer of solution close to the surface maintains its original concentration, that is, it does not suffer from *depletion*. However, the flow cannot be too fast, otherwise the molecules will not spend enough time close to the surface, and will not be able to explore the configurations that would allow them to bind. When depletion occurs, the system is said to be *mass-transport limited*, or *diffusion limited*. On the other hand, when the flow is too fast and molecules do not have time to bind, the system is referred to as *reaction limited* (Squires et al., 2008). The 'sweet spot' between these two regimes is a system in which the concentration of the analyte is maintained constant by a sustained flow, and the molecules are transported efficiently to the sensor, allowing for reaching a true dynamic equilibrium, the only condition in which it is possible to measure an accurate binding rate. The parameters to achieve this ideal regime are defined by the size of the sensor, the thickness of the measurement chamber, the affinity of the molecules and the flow rate (Squires et al., 2008).

In practice, in order to achieve efficient transport and rapid solution exchange to the surface of the sensor, diffusive and convective forces must be carefully balanced. If convective forces are too high, the molecules will be swept away before they have time to diffuse down to the immobilized probes. If convective forces are too low, diffusion will occur slowly and the available analyte concentration will be depleted. The ratio of the diffusive time to the convective time is called the Peclet number and can be described by (Squires et al., 2008):

$$Pe_H = \frac{Q}{DW_c} \tag{3.9}$$

where Q is the volumetric flow, D is the diffusivity of the target molecule and and W_c is the channel width (Squires et al., 2008). Most sensors, such as SPR and BLI, suffer from mass transport limitations when working with high affinity molecules (Schuck and Zhao, 2010; Karlsson, 2016). BLI sensors utilize a shaking mechanism to deliver the molecules to the sensing tip, which usually does not successfully overcome mass transport limitation. On SPR, probe immobilization is usually carried out by using thick hydrogel matrices made of carboxymethyl dextran (CM-dextran). Specifically designed for SPR sensors, CM-dextran is a carbohydrate polymer that creates a tridimensional structure by adding 50-1500nm of thickness to the sensor surface, allowing for most of the evanescent wave penetration depth to be filled with probe molecules. This reduces the bulk effect while increasing the effective volume where target molecules can bind and generate a signal (Nikolovska-Coleska, 2015; Li et al., 2015). The number of probes per unit volume can also be tuned, by having different hydrogel densities, as shown in Figure 3·19.

This approach solves some of the issues of SPR sensors; however, the fact that the probe molecules are submerged in a thick solid matrix also introduces non-negligible

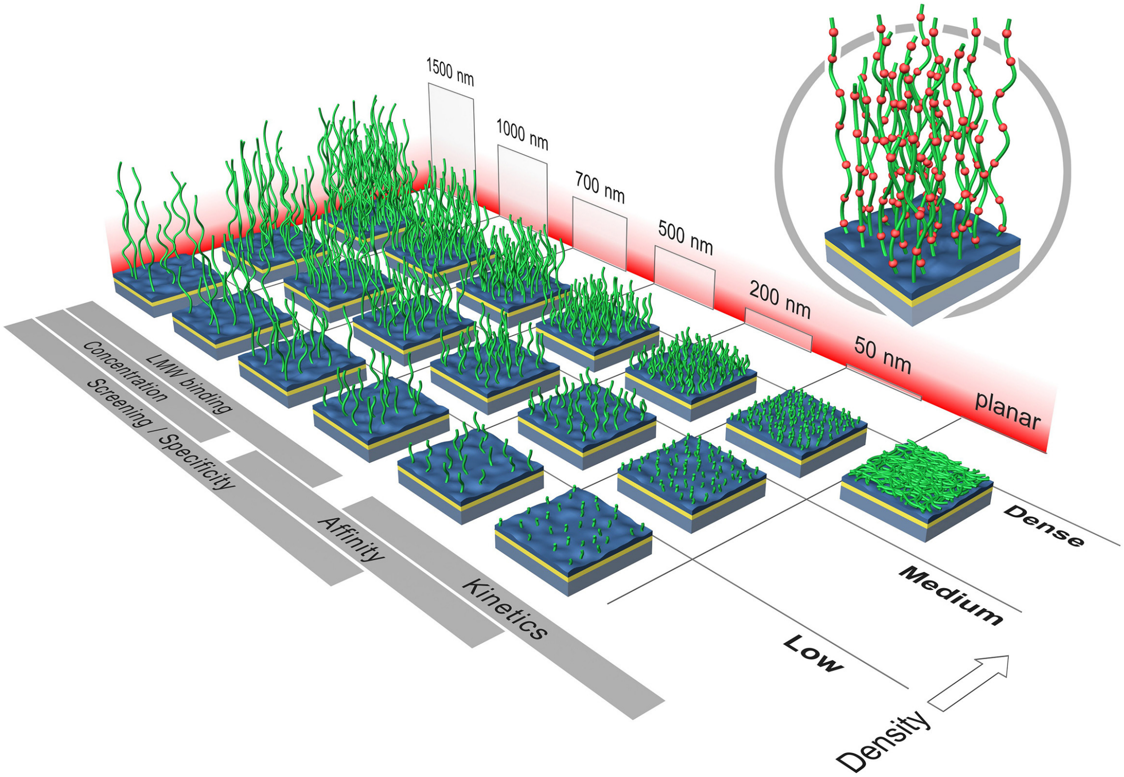

Figure 3·19: SPR chips commercially available from Xantec, Inc. (© Xantec 2021, all rights reserved).

artifacts, limiting the kinetics of the reaction and leading to mass transport limitation. The inherently slow diffusion through the hydrogel limits the velocity at which the solution is replaced by the flow. In most cases, the reaction is therefore diffusion limited, and the measured binding rate is actually the volumetric diffusion rate. Furthermore, given the exponential-decaying nature of the evanescent wave, the target molecules binding closer to the gold layer generate a bigger signal with respect to those binding further away from the surface. This creates additional confusion when interpreting SPR data, causing a discrepancy in the calculated association and dissociation constants.

In order to address some of these issues, available fitting software for SPR data such as EvilFit (Svitel et al., 2003; Svitel et al., 2007) provide various mass transport limited binding models, which consider first-order corrections to the fitting model. In this first-order approximation, the flow channel is treated as a two compartment system, where a *depletion zone* is defined as the section of the channel close to the gold surface, containing the dextran matrix and extending slightly into the solution. When mass transport limitation is present, the concentration of analyte inside the depletion zone is lowered due to binding, and the on and off rates are affected by this change in concentration, causing the reaction to be diffusion limited (Squires et al., 2008). More specifically, if mass transport limitation were not present, the surface binding of a single class of analytes to a single class of ligands (1:1 interaction) would follow a simple rate equation as described by Equations 1.4 - in Section 1.1. In those equations, C is a constant since the concentration of the analyte is assumed to be constant throughout the experiment. Now, the two compartment model considers a depletion of the analyte molecules in the volume close to the surface, resulting in a variation of the concentration from the value C to a lower 'depleted' value $C_d < C$, which is not constant, but rather changes with time, as the surface binding sites start to saturate:

$$\frac{dC_d}{dt} = k_{TR}(C - C_d) - \sum_{i=1}^{N} \frac{dS_i}{dt} \tag{3.10}$$

For N binding sites considered, $i = 1, \cdots, N$. Here, the transport rate parameter (k_{TR}) is introduced, which has been demonstrated to approximately depend on the diffusion coefficient D of the analyte as:

$$k_{TR} \approx 1.282 v^{1/3} h l^{-1/3} D^{2/3} \tag{3.11}$$

where v is the flow rate, h and l are the height and length of the flow channel respectively. Therefore, equation 1.3 mentioned above assumes the form:

$$\frac{dS_i}{dt} = k_{ON,i} C_d (S_{max} - S_i) - k_{OFF,i} S_i, \tag{3.12}$$

which in turn produces distinct association and dissociation rates for each binding site. The discrete increment of bound analyte to single probes can be approximated to a continuous function, in order to obtain single k_{ON}, k_{OFF} and k_{TR} values by numerically solving the following system of differential equations for $S(t)$:

$$\begin{cases} dS/dt = (k_{ON} C_d(t) - k_{OFF}) S(t) \\ dC_d/dt = k_{TR}(C - C_d(t)) - dS(t)/dt \\ S(t=0) = 0; S(t = t_{sat}) = S_{max} \end{cases} \tag{3.13}$$

where t_{sat} is the time where all binding sites are saturated, and the maximum reachable signal is measured (S_{max}) (Svitel et al., 2007).

This discussion shows that having a three-dimensional distribution of probes is not an ideal solution to compensate for the lack of sensitivity of the biosensing platform. On the contrary, working with a monolayer of probes is highly desirable; this however requires extreme sensitivity when working with small molecules (SMs), since detecting a single layer of bound low-molecular weight analyte is non-trivial. The optical signal generated is indeed proportional to the refractive index variation caused by the biomass and will therefore be incredibly small for SMs, as we discussed in the Introduction (Section 1.2.1).

On the IRIS system, we achieve small molecule characterization with a single layer of probes (as discussed in Section 4.1) immobilized on a semi-tridimensional soft polymer, MCP-2 (Pirri et al., 2004). Considering Equation 3.9, on the IRIS system with DNA as the analyte being investigated and a volumetric flow rate of 200 μL/min, the Peclet number is approximately 10^5, confirming convection as the dominant factor. Thus, depletion is negligible for most analytes - down to nM affinity.

The combination of the IRIS detection system with the surface chemistry provided by the MCP-2 polymer provides a really good balance between high molecular probe density and sensitive kinetic measurements.

Chapter 4

Experimental results

4.1 Small molecules characterization

Small molecules (SMs) are defined as the chemical compounds with a molecular weight (MW) below 1kDa (Fechner et al., 2014). Reliable characterization of SMs is still an unmet need in the field of biotechnological development, since most available biosensing platform require to either label the SMs - which is an invasive process that could alter the functionality of the molecule - or are affected by mass transport and diffusion limitations, as discussed in Section 3.5.3. Here, we demonstrate small molecule sensitivity on the IRIS. We will start by showing a simple proof-of-concept experiment, biotin binding to a streptavidin surface, where we determine the limit of detection (LOD) of the sensor and once again highlight the importance of reducing the noise by averaging, on a shot-noise limited system such as the IRIS. Then, we will present a relevant biotechnological application with the characterization of a corn toxin, fumonisin B1, whose detection is of utmost importance in food quality control and toxicology.

4.1.1 Biotin

In order to experimentally measure the LOD of our sensor for SMs detection, we have implemented a simple, proof-of-concept biotin-streptavidin binding experiment (Chiodi et al., 2020a). Biotin belongs to the category of SMs (MW = 244.31Da) and is one of the most utilized chemical compounds in biology and biotechnology applications. Its interaction with streptavidin is the strongest non-covalent interaction in nature, which makes these two molecules suitable for strongly anchoring other biomolecules to a surface (Wong et al., 1999). Here, the biotin-streptavidin interaction is used as a proof-of-concept to optimize the acquisition parameters of the sensor.

For this experiment, streptavidin molecules were immobilized on MCP-2-coated IRIS chips in a microarray modality, at a spotting concentration of 1mg/mL ($\approx$ 18μM). The resulting spots were around 100μm in diameter. Biotin was flowed across the streptavidin spots at a 1μM concentration for 20 minutes, at a flow rate of $200 \mu L/min$. Binding of biotin molecules to the streptavidin probes is extremely fast, as is expected if one considers the very low K_D of the interaction ($\approx 1pM$). Therefore, the obtained binding curve has the appearance of a step (Figure 4·1).

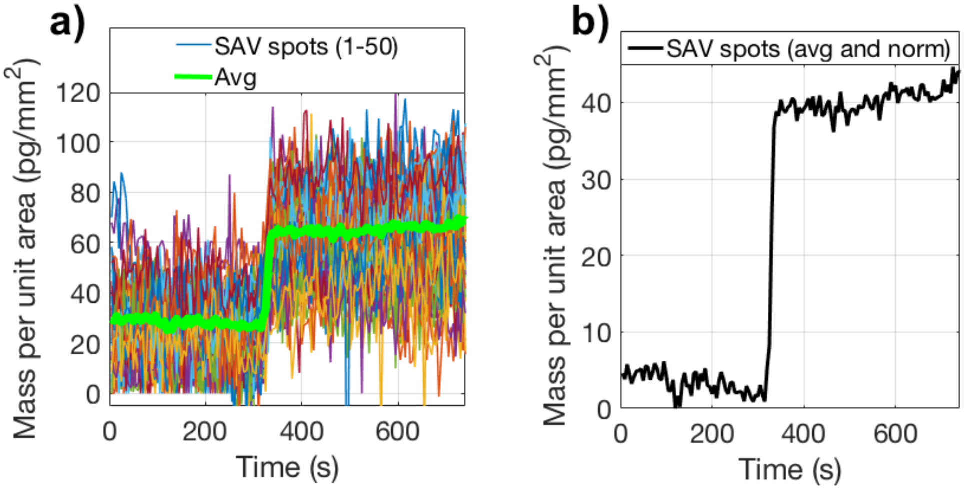

Figure 4·1: The effect of averaging on a streptavidin-biotin experiment. Biotin was flowed at a concentration of $1\mu M$ across a chip where 50 streptavidin spots were previously printed. (a) Biotin signal without spatial averaging (single spots) (b) compared to biotin signal with spatial averaging (50 spots). Temporal averaging was fixed at 100 frames/image. Reproduced with permission from (Chiodi et al., 2020a).

Here, the averaging techniques discussed in Section 3.1 were applied in order to achieve the best possible sensitivity. Precisely, 100 frames were averaged in time for each image in the experiment, and 50 microarray spots (5024 pixels each) were analyzed. The data in Figure 4·1a, shows the average signal value for each of these 50 microarray spots. When these 50 microarray spots are averaged together, the result, seen in Figure 4·1b, shows a clear binding step and an SNR of 34. The noise level achieved was 1pg/mm^2 (Chiodi et al., 2020a).

4.1.2 Fumonisin toxin

Toxins are poisonous substances produced by living organisms. Most toxins fall into the previously defined category of SMs (Wishart et al., 2015). In particular, mycotoxins are low-molecular weight ($<$800Da) secondary metabolites produced by microfungi which can be easily found in fresh produce, as a result of fungal infections. Mycotoxins are harmful to both humans and animals, provoking diseases (mycotoxicoses) which might lead to cancer formation (Chu and Li, 1994). Given the serious effects that they provoke on human health, the food industry is facing the critical issue of trying to detect the presence of mycotoxins in food products during quality control procedures.

The noise-optimized IRIS system is applied here to the study of the binding kinetics of Fumonisin B1, a 721.8Da mycotoxin produced by the Fusarium fungal species. This fungus usually attacks corn crops and acts by weakening the core structure of corn cobs.

For these experiments, twenty antibodies that tested positive to the toxin in an enzyme-linked immunoassay (ELISA) were immobilized onto a MCP-2-coated IRIS chip, where twenty spots were devoted to each antibody, for a total of 440 active spots that were imaged simultaneously (Figure 4·2, 20 antibodies, each printed on 20 equal spots, and 40 control spots). Each antibody was originally at a different concentration, , due to variations in the purification yield, and therefore the spots have different initial mass densities, which relates to varying intensities as shown in Figure 4·2; thus, the steady state signal level may not be predictive of binding kinetics.

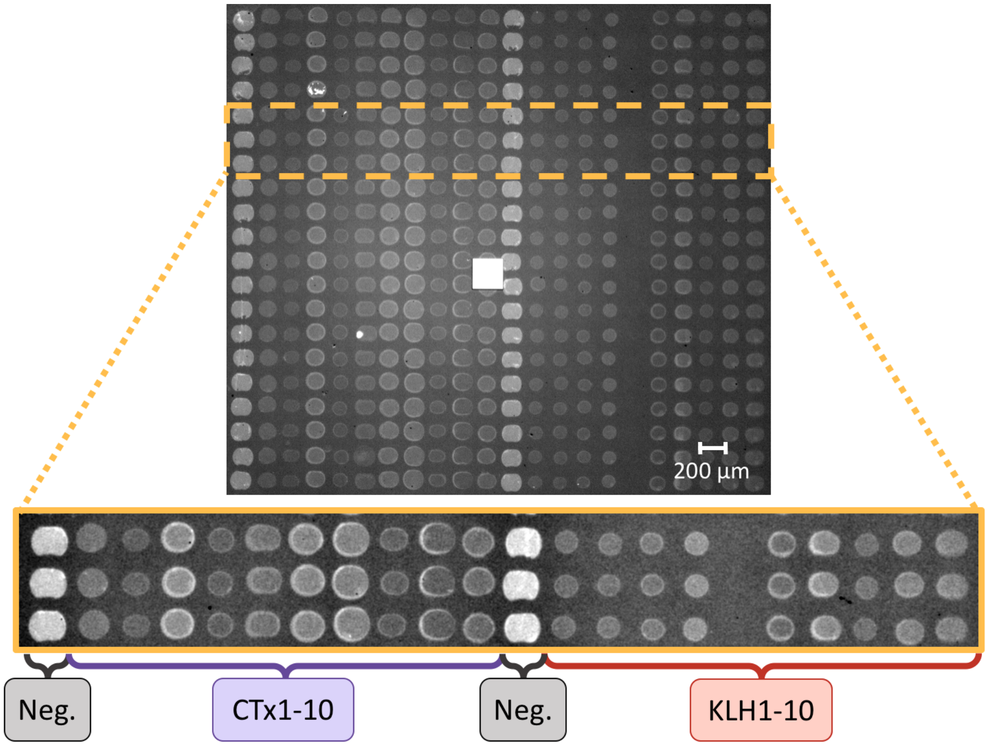

Figure 4·2: An IRIS image of the 440 antibody spots on one of the chips used for the experiments. The first and 12th columns are devoted to the control (bovine IgG); columns 2 to 11 are devoted to fumonisin B1-CTxB antibodies (CTx1-10), and columns 13 to 22 are devoted to fumonisin B1-KLH antibodies (KLH1-10). The different intensity of the spots is due to differences in concentration of the spotted samples. Reproduced with permission from (Chiodi et al., 2020a).

Fumonisin at a concentration $C_0 = 100\mu M$ was flowed across the surface of the chip for 20 minutes at $200\mu L/$min, followed by PBS-1X at $200\mu L/$min for 20 more minutes. Binding was detected on 18 out of the 20 antibodies, and representative binding curves are reported in Figure 4·3. A simple 1:1 Langmuir model (Equation 1.3) was used to fit the curves and obtain the association and dissociation constants, reported in the Appendix (Table A.1). The remaining 14 binding curves are reported in the Supplementary Material (Figures A·1 and A·2).

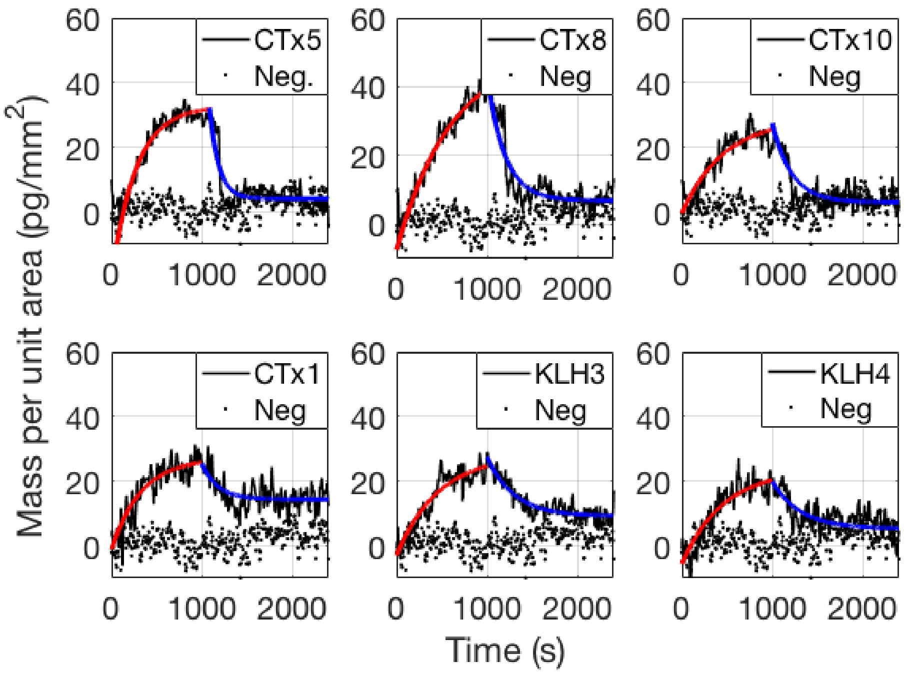

Figure 4·3: Binding and debinding curves of the fumonisin B1 toxin at a concentration of $100\mu M$ to six different antibodies. The association part of the fit is shown in red, solid line. The dissociation part is shown in blue, solid line. The control spots' trend is shown in black, dotted line. Reproduced with permission from (Chiodi et al., 2020a).

From our measurements, the antibodies produced with fumonisin B1-CTxB, seem to have a higher affinity to fumonisin B1. Particularly, the antibody that we have labeled as CTx5 has the highest association constant and lower equilibrium constant (K_D).

Moreover, we have calculated the theoretical mass density that a single layer of fumonisin molecules would produce on our sensor. More precisely, we have predicted the expected biomass accumulation for a certain range of analyte sizes (in daltons). We have calculated how many probe molecules would fit inside a 100μm-diameter spot, by simulating them as spheres with a diameter in the nm range. Streptavidin can be modeled as a 4.66nm-diameter sphere (Reth, 2013), while IgG antibodies can be assumed to roughly occupy the volume of a 7.5nm-diameter sphere (Williams et al., 2012). For a monolayer of adjacent probes, the average center-to-center distance between two molecules corresponds to their size. If the spot is saturated with probe molecules, the probes will form a monolayer; however, we also considered the situation when the probes are more sparse, given that in our experiments the initial spotting concentration was sometimes very low. Then, we predicted the biomass accumulation for target molecules of different sizes. The resulting simulated results are shown in Figure 4·4, and the two labels indicate the expected biomass accumulation for Fumonisin B1 ($\approx$ 27pg/mm^2) and for biotin ($\approx$23pg/mm^2) on a monolayer of immobilized probes.

As expected, the binding mass density decreases exponentially decrease with increasing distance between probes. This poses two issues: bigger probes will take up more space on the spot and therefore their average number will decrease, leading to a lower binding signal. Additionally, if the probes are sparse due to low spotting concentration, the binding density will be even less, becoming potentially undetectable. The results in Figure 4·4 stress the fact that having a high density of probes on the surface is fundamental, and therefore spotting optimization procedures need to be considered when the concentration of the spotting solution is very low. This might also be a potential explanation for the lack of detected binding on low-concentrated antibody spots. The scarcity of probes could have affected the instrument's ability to detect binding: even if fumonisin had saturated the surface, the density could have been below the LOD.

To compare theoretical and experimental values, we can consider for example the mean binding density of fumonisin across all the eighteen antibodies, which is 20.9±7 pg/mm^2. The huge standard error reflects the fact that fumonisin bound with a different affinity to each antibody, as well as the impact of probe concentration on the surface. On the other hand, the experimental result for biotin is 40.3±1.5 pg/mm^2,

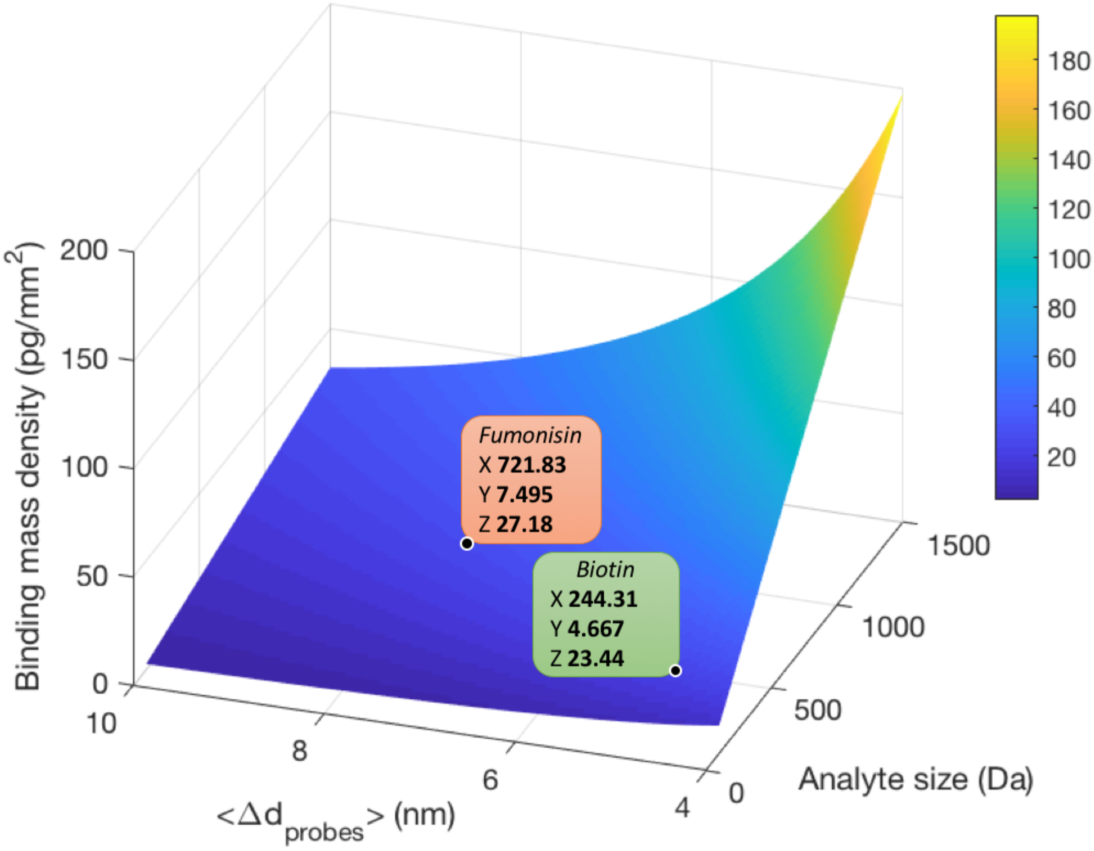

Figure 4·4: Calculated values for binding mass density for a range of analyte sizes (100-1500Da) and center-to-center average distance between probes (4-10nm). The labels indicate the theoretical values for Fumonisin B1 (red label) and biotin (green label) assuming a monolayer of adjacent probes on a 100μm-sized spot. Reproduced with permission from the supplementary materials of (Chiodi et al., 2020a).

which is almost double the expected value ($\approx$ 23pg/mm^2, Figure 4·4). However, the simulations consider a 1:1 probe-analyte interaction. This is certainly realistic for the case of fumonisin, since the capture antibody possesses only two binding sites for the toxin, one of which could be inaccessible because involved in the immobilization (Figure 4·5b). However, in the case of biotin, every streptavidin molecule has four binding sites, uniformly distributed around the molecule. Therefore, the probability that - on average - two binding sites might be available is higher, thus doubling the predicted biomass accumulation from $\approx 23\text{pg}/\text{mm}^2$ to $\approx 46\text{pg}/\text{mm}^2$, which is closer to the experimental value (Figure 4·5a). Therefore, the fact that two biotin molecules are still smaller than one molecule of fumonisin does not necessarily imply that detecting biotin requires more sensitivity than the toxin, because the accumulated mass will be similar or even higher, in accordance with experimental data.

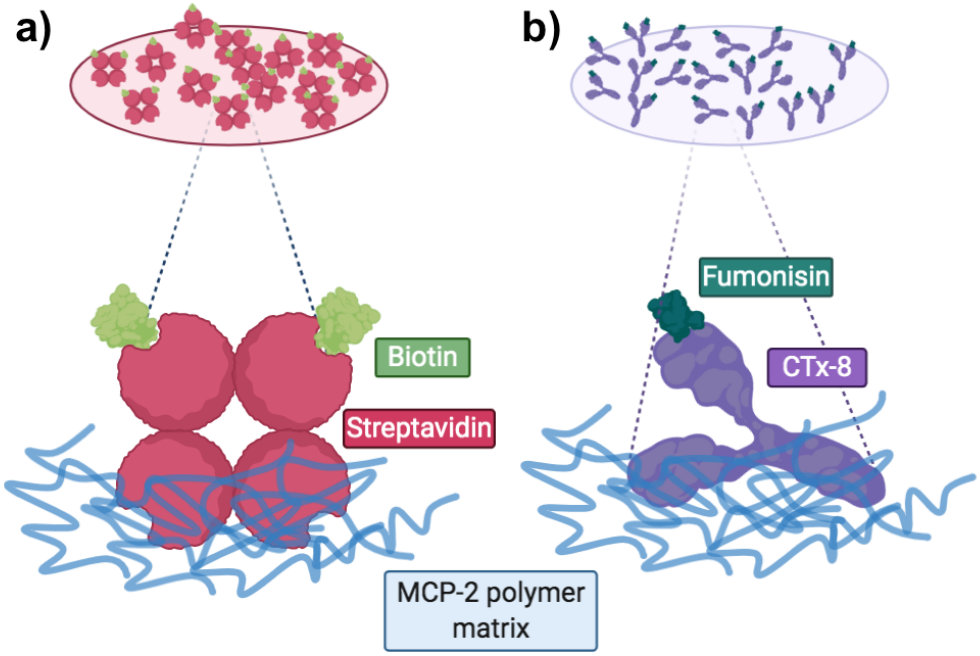

Figure 4·5: Schematic representation of immobilized streptavidin (a) and fumonisin antibody (b) molecules. Considering the disposition of the binding sites of the molecules, on average, two molecules of biotin will bind to each molecule of streptavidin, while only one molecule of fumonisin will bind to each antibody.

4.2 Real-time detection and imaging of extracellular vesicles

Extracellular Vesicles (EVs) are cell-secreted biological nanoparticles that contain genetic material and protein fragments. Recently, they have attracted significant attention as novel biomarkers for early diagnosis of cancer and degenerative diseases, since their properties are closely related to specific clinical conditions, as we have discussed in Section 1.2.2. Here, we would like to demonstrate complete characterization of EVs both at the analog and digital level. We have performed binding kinetic measurements of cell-culture purified EVs on multiplexed chips in order to optimize measurement conditions such as flow rate, probe concentration and type. Then, we have analyzed human EVs samples from both healthy individuals and lung cancer patients, to investigate the possibility to use these BNPs as lung cancer biomarkers.

4.2.1 Analog real-time characterization

Developing experiments that involve EVs phenotyping is usually highly challenging and time-consuming, due to laborious optimization steps. First, the samples must be purified by from cell culture supernatant or human plasma by ultracentrifugation or other purification methods; then, the vesicles need to be captured on the sensor surface, where capture probes have been immobilized. In order to perform end-point measurements, the capture reaction needs to saturate, that is, the vesicles must have occupied all the available binding sites on the surface. This step often requires in an extremely long incubation time. A typical phenotyping experiment involves a 12h- or overnight incubation of the sensor chips with the EVs sample, thus causing a significant delay in data acquisition.

To address the need for faster and more high-throughput EVs characterization methods, we have demonstrated real-time, kinetic analysis of EVs binding to the surface of a chip where we had previously prepared 18 different probe conditions, on the analog IRIS system. The results of this work are reported in (Chiodi et al., 2021a). Surface probe conditions were varied by immobilizing three different antibodies, each spotted at six different concentrations, on the same substrate. Since probe density and spot homogeneity plays a huge role in EVs analysis, the first control experiment was performed as an optimization of the spotting conditions.

For this work, three tetraspanin-specific antibodies (aCD9, aCD63, aCD81) were used as EVs capture agents. In order to maintain a good spot conformation, the density of the active antibodies was tuned by diluting them with a solution of a different antibody, a generic Mouse IgG$_{2a}$, at different ratios. This allowed for keeping the same molecular concentration of the spotting solution (3 mg/mL) while varying the percentage of the active molecules. Ideally, by using this method, the percentage of tetraspanin specific antibody within each spot should change linearly depending on their ratio with respect to the negative molecule. The idea behind this technique is to maintain a constant surface biomass density for all spots, therefore controlling the spot conformation and uniformity, while creating multiple concentration conditions. An initial IRIS image of the spotted chip is shown in Figure 4·6a. It can be noticed that the spots look similar in terms of initial intensity, since the immobilized biomass is comparable for all of them.

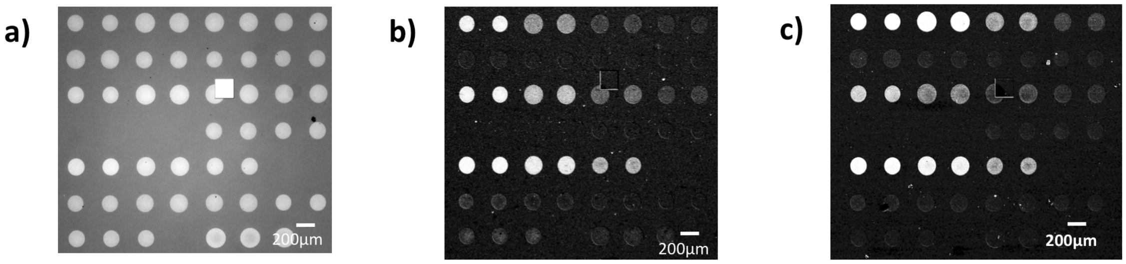

Figure 4·6: IRIS images of the chips utilized for the experiment a) before incubation, and differential images after incubation with b) antibodies and c) small EVs. To be noted that a similar level of signal doesn't necessarily correspond to the same increase in thickness, since a different wavelength is used for each experiment. Reported with permission from (Chiodi et al., 2021a).

Theoretically, the six concentrations of each antibody (in terms of active molecule percentage) were 100%, 50%, 25%, 12%, 6%, 3%. As a negative control, two spots of 100% Mouse IgG$_{2a}$ were also printed. Since the yield of the immobilization process is not ideal, though, the actual amount of active probe within each spot was measured by running a simple control experiment on the IRIS system. For this experiment, a generic IgG$_1$ antibody was flowed across the surface of a chip that was functionalized as described above. Since the utilized anti-tetraspanin probes are immunoglobulins, and particularly belong to the family of IgG$_1$, the positive control aIgG$_1$ could bind to all of them, and control binding curves were generated. A differential image of the IRIS chip after the control experiment can be observed in Figure 4·6b, while the binding curves are depicted in Figure 4·7. For this experiment, blue LED wavelength was used, since it is a standard analog antibody-antibody interaction.

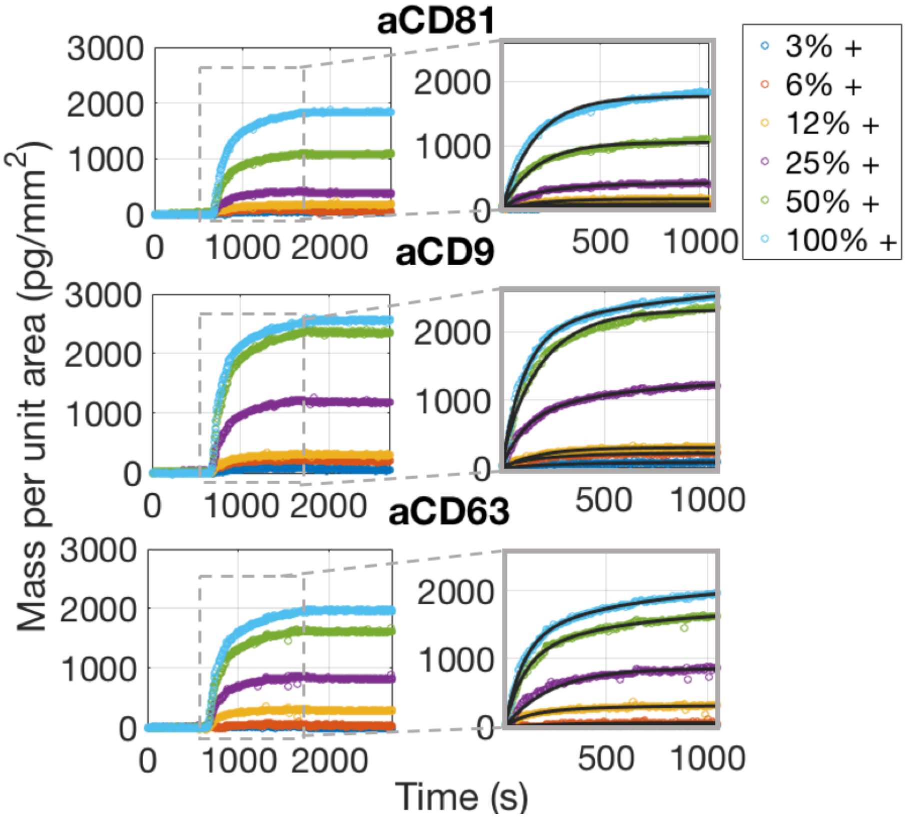

Figure 4·7: Binding curves of a generic IgG1 to one of the antibody chips used for the experiments. The insets focus on the association phase of the curves, which are fitted with a bivalent model. Reported with permission from (Chiodi et al., 2021a).

In order to characterize the antibodies, we utilized a bivalent interaction model ($A + A + B \underset{k_{OFF,1}}{\overset{k_{ON,1}}{\rightleftharpoons}} AB + A \underset{k_{OFF,2}}{\overset{k_{ON,2}}{\rightleftharpoons}} AAB$) which was solved numerically in MATLAB. The dissociation constant was measured for all of them to be in the order of $K_D \approx$

$10^{-9} M$, which is consistent with values found in the literature for similar antibodies (Bakhshpour et al., 2022).

From the equilibrium values reached by the binding curves, as well as from the initial slopes, the amount of immobilized probe can be estimated, and compared with the theoretical value. A comparison of the expected and experimental values for the initial concentration of the probes is reported in Figure 4·8. As expected, both the initial slope and the equilibrium binding signal measured for the antibodies increase proportionally to the spotted ratio of active to inactive molecules. This is therefore an effective method to tune the probe density by maintaining a uniform spot conformation.

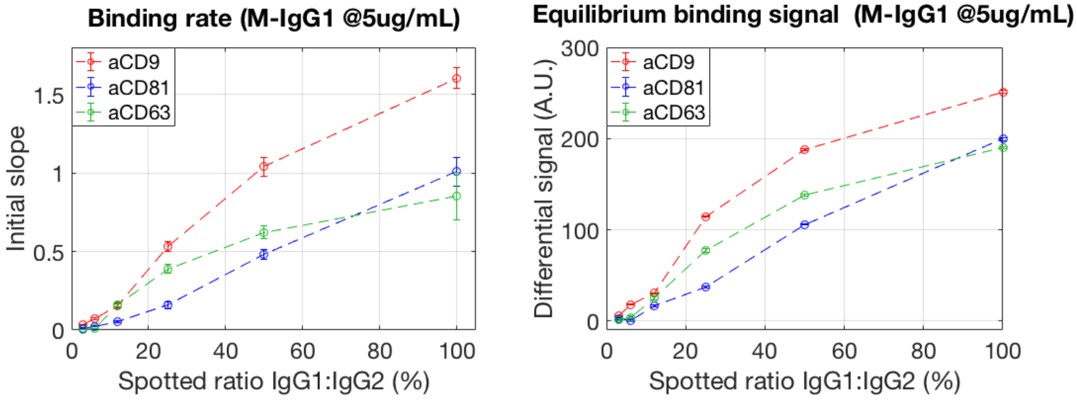

Figure 4·8: Verification of the amount of active antibody on the surface. The spotted percentage of active probe versus a) the initial slope of the binding curves in Figure 4·7 and b) the maximum signal obtained on the same dataset. Reported with permission from (Chiodi et al., 2021a)

For the EVs characterization experiment, a sample of HEK cell culture purified EVs was utilized. The EVs were purified by ultracentrifugation, and the sample was utilized fresh. The size distribution of the vesicles was analyzed on the ExoView system, a commercial EVs characterization platform which utilizes the SP-IRIS technology. The resulting size histogram is reported in Figure 4·9, along with a label free image of the particles captured on three anti-tetraspanin spots. As expected, all vesicles range in size between 30-70nm.

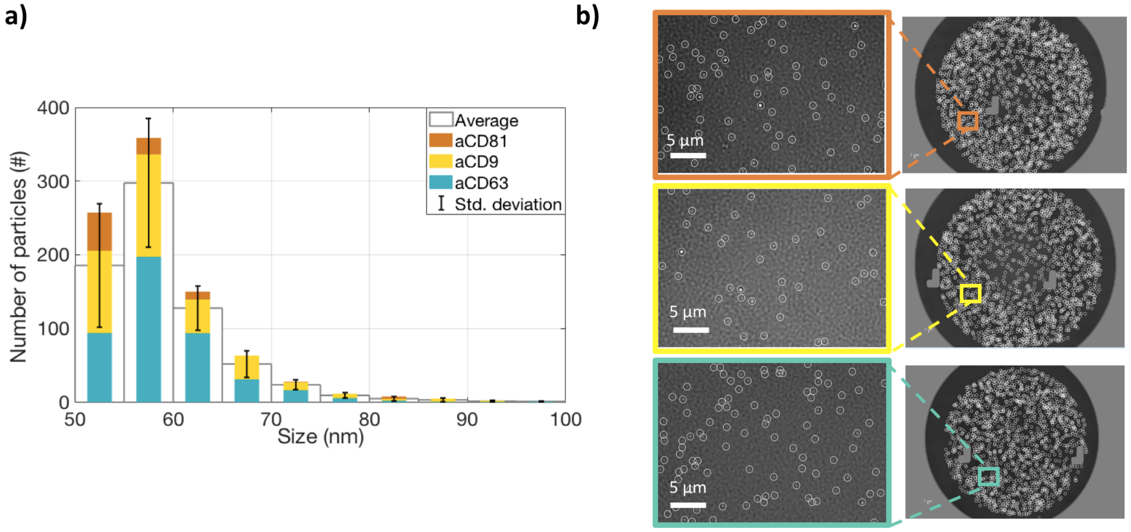

Figure 4·9: a) The size distribution of EVs captured on CD9, CD81, CD63 spots and b) label-free images of the particles on one of the spots. Reported with permission from (Chiodi et al., 2021a).

Prior to the EVs real-time binding experiment, the sample was centrifuged once more, at 60’000 rpm for 10 minutes, in order to remove large aggregates. The supernatant was then collected and diluted (2X), then flowed across the surface of the IRIS chip. The experiment included 10 minutes of surface stabilization under PBS flow, then the EVs sample was flowed for 20 minutes, and finally PBS was flowed again as a washing step for 10 minutes. The binding curves obtained for EVs accumulation are shown in Figure 4·10. For this experiment, we utilized green LED illumination in order to have a better signal-thickness correlation for large analytes, as explained in detail in Section 3.2.2.

Results shown in Figure 4·10 demonstrate the ability of the IRIS system to detect EVs accumulation in an analog fashion. Moreover, under high flow conditions (200μL/min) the surface was nearly saturated after only 20 minutes of sample flow. We attempted to run stop-flow measurements, with the intent to measure a difference

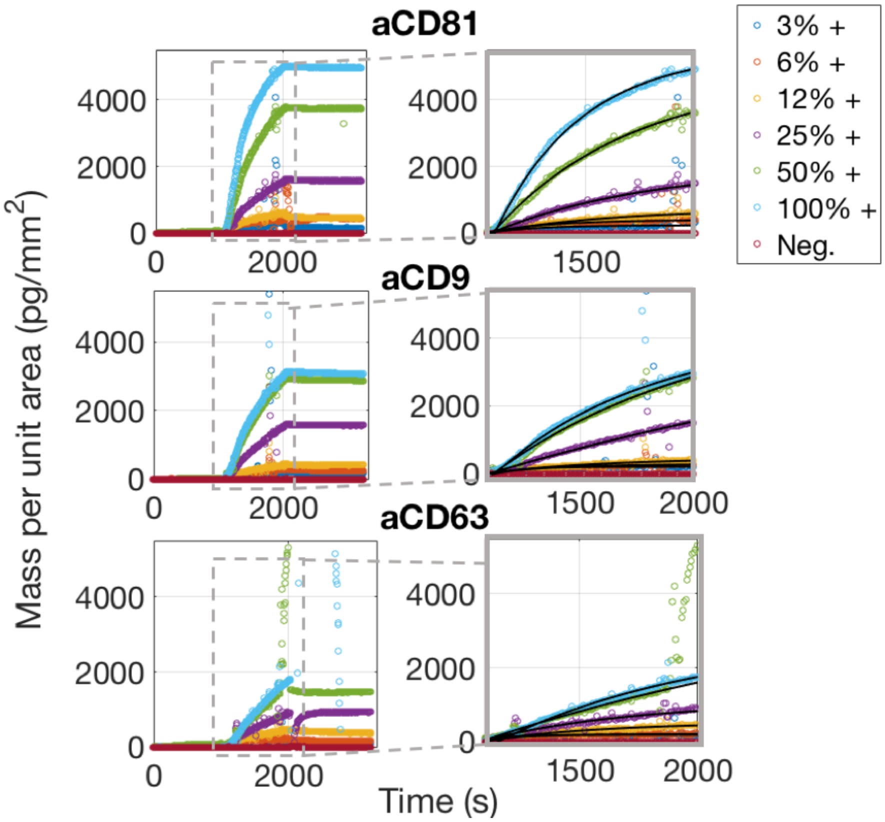

Figure 4·10: Real-time binding curves of EVs accumulating onto three different probes, each at six different concentrations. The insets focus on the association phase of the curves, which was fitted with a multivalent model that separates an initial, fast association rate $k_{on,fast}$ from a slower, subsequent rate $k_{on,slow}$. Reported with permission from (Chiodi et al., 2021a).

in accumulation rate when the incubation is static versus kinetic, however the flow variations caused debris accumulation on the surface of the chip, making the measurement impossible. Nonetheless, with these measurements we could demonstrate that aCD81 is the best capture probe under the tested conditions, and that a constant flow improves EVs capture - the reaction reached saturation after less than half an hour, while most static methods require overnight incubations. The reason for this behavior can be found in the diffusion mechanisms that govern the capture reaction in a static system versus a dynamic one: in absence of flow, brownian motion is the only factor that contributes to the particles diffusing and exploring configurations close to the surface that will eventually lead them to bind. On the other hand, when in-flow recirculation is involved, the number of configurations per unit time that the particles are allowed to explore is much higher, leading to a much faster reaction with a shorter saturation time.

For what concerns the fitting model utilized to determine the kinetic parameters of EVs binding, we utilized a model proposed by Li et al. (Li et al., 2014) which describes the kinetics of NP binding considering the effect of probe avidity. Avidity effects occur when an object expressing more than one receptor molecules binds to a surface that is functionalized with a capture probe targeting that receptor. When the capture reaction takes place, a multivalent interaction occurs, and the particle occupies a large number of probe binding sites. This reduces the probability of other particles binding in its vicinity. The mechanism is similar to steric hindrance, yet instead of it being caused by the spatial presence of an object, it is related to its probe occupancy. The proposed model considers the target particles as if they were divided between a certain amount of *slow binders* and *fast binders*. The fast binders are particles that bind to the surface at the beginning of the experiments, when all probe molecules are still available, and can therefore occupy as many binding sites as possible without any external interference. The slow binders, on the other hand, reach the surface when it is already partially saturated, and therefore have less space and probe binding sites to interact with, therefore finding it more difficult to reach a stable configuration to bind. This model defines the fast binders binding rate as $k_{ON,fast}$ and that of the slow binders as $k_{ON,slow}$. The same reasoning is applied to the dissociation phase, but in reverse: at this point, fast binders will be more stably anchored to the surface, therefore their dissociation will be slow, while slow binders will be attached to a smaller number of probe molecules, and will therefore be washed away more easily - leading to a faster dissociation rate. To avoid confusion, in this discussion $k_{OFF,fast}$ will still refer to the dissociation rate of fast binders, and $k_{OFF,slow}$ to that of slow binders.

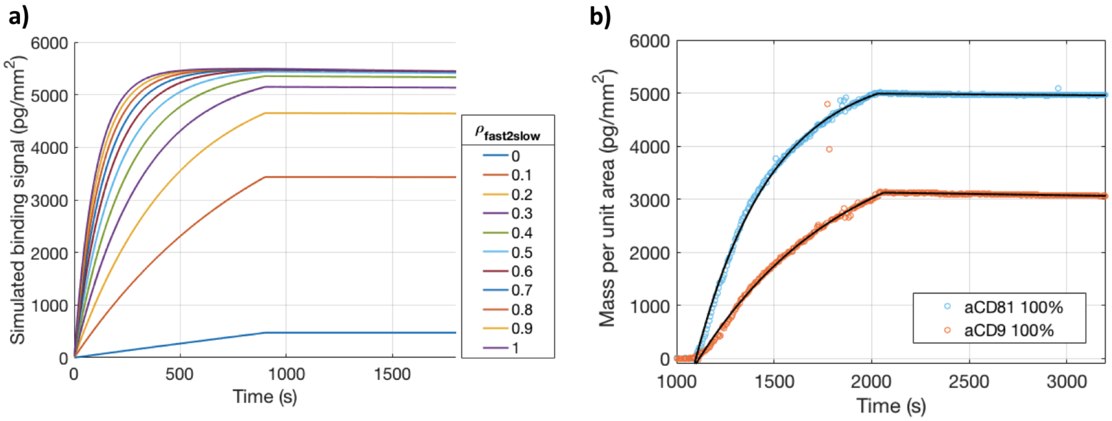

Figure 4·11: Comparison of simulated and real binding curves of EVs. a) Simulated curves, where increasing percentages of fast binders versus slow binders are considered. Here, $k_{ON,fast} = 10^4 M^{-1}s^{-1}$, $k_{OFF,fast} = 10^{-5}s^{-1}$, $k_{ON,slow} = 10^3 M^{-1}s^{-1}$, $k_{OFF,slow} = 10^{-10}s^{-1}$. b) EVs binding curves to aCD9 (orange) and aCD81 (blue). The black line indicates the fit. Reported with permission from (Chiodi et al., 2021a)

In order to fit the data with this model, we first needed to establish the concentration of fast to slow binders in our case. We have then simulated the effect of having varying amounts of fast and slow binders in a solution, by using the parameter $\rho_{fast2slow}$ to indicate the ratio of fast to slow binders. Since this ratio depends on particles' size, probe affinity, the number of multivalent sites on each particle and the concentration of the sample, we decided to simulate the kinetics for values of $\rho_{fast2slow}$ that ranged from 0 (all slow binders) to 1 (all fast binders), looking for the model that best represented our data. The result is shown in Figure 4·11a. The ratio $\rho_{fast2slow}$ that best fits our data is $\rho_{fast2slow}$= 0.4, meaning 40% of fast binders. The fitted data are shown in Figure 4·11b, and $R^2 = 0.998$ for this model. The obtained binding constants are also consistent with the ones which were used as an input for the simulations, resulting as follows: $k_{ON,fast} = 10^4 M^{-1}s^{-1}$, $k_{OFF,fast} = 10^{-5}s^{-1}$, $k_{ON,slow} = 10^3 M^{-1}s^{-1}$, $k_{OFF,slow} = 10^{-10}s^{-1}$.

To summarize, in this Section we have shown analog characterization of EVs on the IRIS platform. These experiments were a proof of concept, to demonstrate that this method can be utilized as an optimization step for more efficient capture and characterization of BNPs. With further optimization, this technique has the potential to accelerate EVs analysis in diagnostics and clinical studies.

4.2.2 Digital imaging: INDEX

While analog-based characterization of EVs is incredibly useful for optimization of probe concentration and affinity, as well as incubation conditions, it does not enable characterization of some specific features of the vesicles, including size population and cancer-specific markers. As a matter of fact, cancer cells-derived EVs often express on their surface a fraction of cancer-specific proteins, although, in most cases, they only constitute a small minority of their cargo and therefore would not enable analog phenotyping, due to the limited amount of signal their accumulation would produce.

Digital imaging of EVs can overcome this difficulty, by enabling single particle characterization in number, size, and protein cargo. Still, label-free imaging of these membranous objects is challenging, as they are composed of a bi-lipidic layer full of liquid, making them very similar in refractive index to the surrounding medium. Fluorescence labeling techniques for specific visualization of single EVs have recently been developed, and are commonly utilized to observe the presence of specific markers on the membrane or in the cargo of the vesicles (Mallick et al., 2020). However, fluorescent markers are subject to a number of issues including non-specific tagging and photobleaching. Another common method for single-particle characterization of EVs is transmission electron microscopy (TEM), which in turn requires specific treatments for fixation of the sample on a glass slide, and that could damage the structure of the vesicle.

In the context of the European Grant Program Horizon 2020 (H-2020), the INDEX project proposed to utilize the IRIS single particle detection technology to characterize single EVs for size, number, and disease-specific surface markers. Particularly, four markers commonly found in lung cell-derived EVs were utilized for characterizing EVs that were purified from the plasma samples belonging to 34 human patients (17 lung cancer patients and 17 healthy controls). The vesicles were either purified through a fluidized bed of magnetic nanoparticles (Pereiro et al., 2017) or by DNA-directed capture and separation (Brambilla et al., 2021). The utilized capture probes were aCD9, aEpCAM, aTS8, aEFGR and aCD151. The first one is an antibody against CD9 tetraspanins which we also used for analog detection of EVs (Section 4.2.1), while the other ones are cancer-specific EVs markers. Specifically, Epithelial Cell Adhesion Molecule (EpCAM) is a glycoprotein mediating cell-cell adhesion in skin cells, and epithelial tumor cells have been shown to secrete EpCAM-presenting EVs (Kahlert and Kalluri, 2013); Epidermal Growth Factor Receptor (EGFR) is a transmembrane receptor tyrosine kinase protein whose overexpression has been associated with the presence of various cancers, including lung cancer (Sorensen et al., 2014); CD151 is a surface glycoprotein that has been shown to promote metastasis formation in cancer cells (Tokuhara et al., 2001); finally, TS8 is a tetraspanin that is also overexpressed in tumor tissues, and it is particularly useful as a biomarker for lung cancer (Sandfeld-Paulsen et al., 2016a).

We spotted IRIS chips with the selected probes, and each probe was immobilized in three replicate spots. To produce the EVs quantification data, we acquired initial images of the spotted chips, then incubated them with the purified EVs samples for three hours recirculating at low speed (2μL/min), followed by a PBS wash at high speed (200μL/min) and finally the chamber was gently dried with nitrogen flow and imaged again to visualize the captured particles. Below, in Figure 4·12, is an image of an area of an aCD9 spot before and after incubation with one of the healthy control samples.

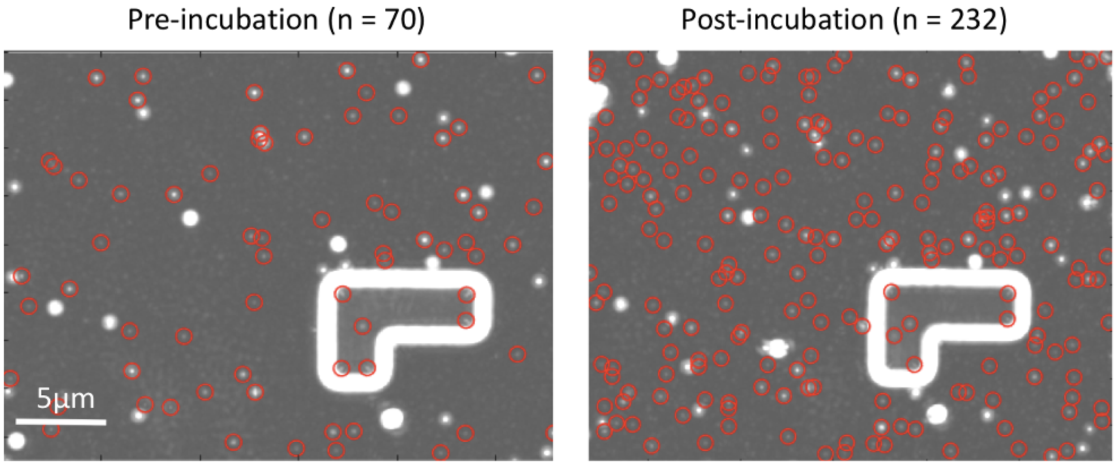

Figure 4·12: Pre- and post-incubation images of an INDEX chip that was incubated with extracellular vesicles purified from healthy donor's plasma.

As expected, cancer patients' samples showed a higher capture rate on cancer specific biomarkers with respect to the healthy marker, as shown in Figure 4·13. However, the difference was not significant enough to be considered relevant, especially due to the large standard deviation measured in the case of cancer patients' samples. These experiments should therefore be repeated and the statistics should be improved. More averaging would certainly help in terms of reducing the error on event counting, moreover, the visibility of the vesicles should be improved in order to allow for in-liquid, real time detection. For example, EVs could be conjugated with a metallic nanoparticle, which would dramatically increase their refractive index. This could be an interesting application of the hybrid IRIS platform, as discussed in the Future work Section.

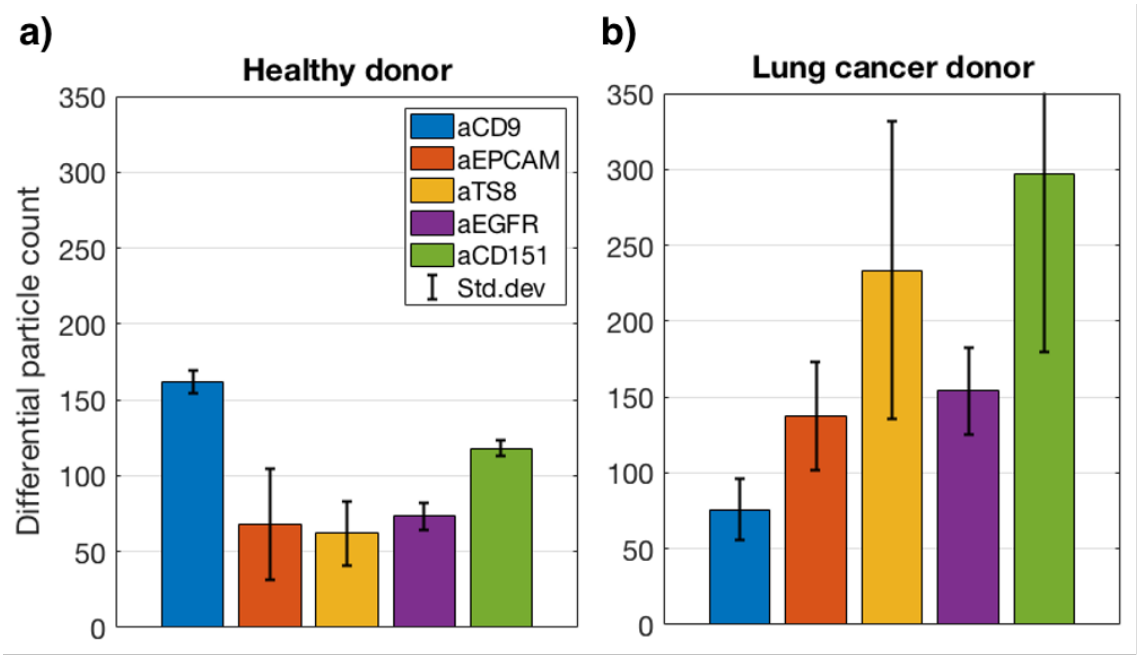

Figure 4·13: Two examples of differential EVs count on each antibody marker for a) plasma from a healthy donor and b) from a lung cancer patient.

4.3 Study of gold nanoparticle-conjugated analytes

4.3.1 Proof of concept: Human aIgG-IgG

In this Section, we will present the kinetic analysis of complexes of gold nanoparticles and antibodies (mAb-GNPs), which complete the collection of multi-sized analytes discussed in this dissertation. In order to demonstrate parallel analog and digital detection of NPs, we started from a proof of concept experiment where we utilized IgG-spotted chips and captured aIgG-functionalized GNPs. The experiment was performed on the h-IRIS system, with green LED as an illumination source. The utilized chips had an oxide thickness of 110nm, which, in combination with green wavelength, provides decent reflectance signal for both analog and digital measurements, as discussed in Section 3.2.3.

The IgG spotted chips were incubated with PBS for 5 minutes prior to the injection of the nanoparticle sample. Then, the particles were flowed at $200\mu L/min$ for 15 minutes, followed by PBS again, as a washing buffer, for 5 minutes. Below, in Figure 4·14 is reported the binding curve of the NPs to the antibody surface. Here, BSA has been used as a negative control.

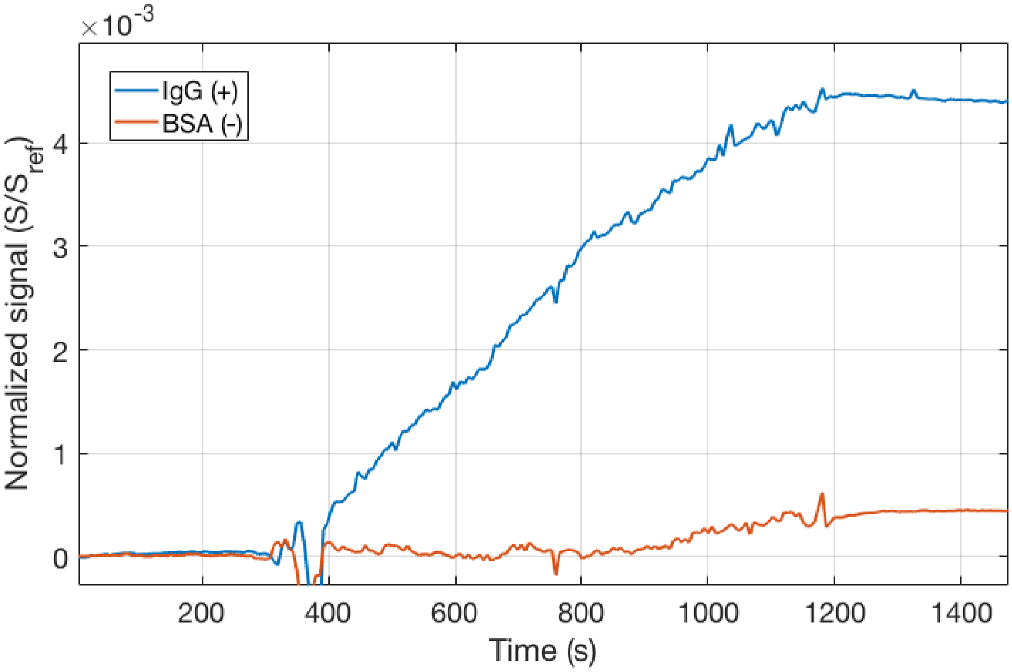

Figure 4·14: Binding of 80nm aIgG-GNS complexes to an IgG surface, at a concentration of $10^1$0particles/mL. The negative control is a BSA spot.

Digital defocus scans were acquired before and after incubation with the particle sample, in order to perform differential imaging. Pre- and post- digital images are reported in Figure 4·15.

The concentration of the nanoparticles injected was 10^{10}particles/mL. The sample was recirculated in the chamber for the duration of the experiment, in order to reduce sample volume. The amount of signal obtained is comparable with what predicted by simulations, as it will be better discussed below in Section 4.3.3.

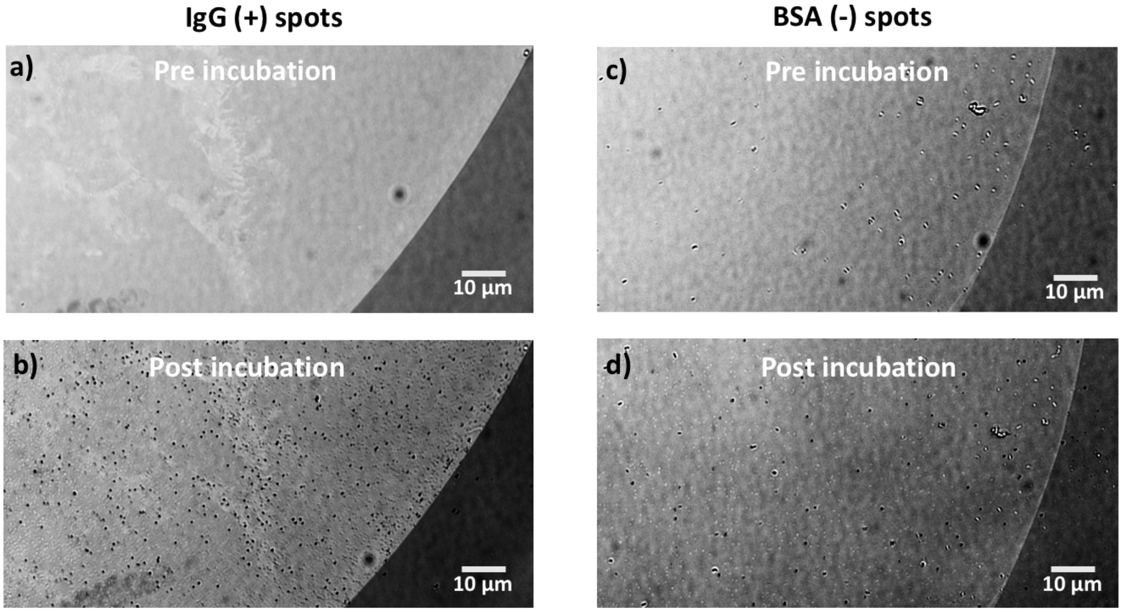

Figure 4·15: Pre (a-c) and post (b-d) images of of 80nm aIgG-GNS complexes bound to an IgG surface (+) as well as a BSA spot (-) at a concentration of 10^10particles/mL.

4.3.2 Hepatitis B antibody sandwich assay

Hepathitis B viral infection (HBV) affects more than 300 million people worldwide every year, and is a common cause of liver cancer. In some patients, HBV can develop into a chronic infection, leading to a lifelong disease. As of today, chronic HBV can be controlled with medications, but cannot be cured (Liang, 2009; Peters, 2019). The probability to develop a chronic version of the infection is particularly high in patients with chronic liver conditions such as cirrhosis. As for any viral infection, early stage detection of HBV is essential to prevent transmission. It has been recently demonstrated that gold nanoparticle-based Lateral Flow Assays (LFAs) can be utilized to detect the genetic material within the virus (Lin et al., 2021). Here, we propose to demonstrate a real-time gold nanoparticle-based assay to simulate a HBV detection LFA at the single molecule level.

For these experiments, we performed a sandwich assay by capturing, then labeling

HBV core antigen. We utilized an antibody pair targeting two different domains on the protein, one for capturing and one for labeling. This method has the potential to be impactful in diagnostics, where it could lead to single molecule detection of pathogen markers at low concentration in purified patients' plasma samples. At this stage, though, the main purpose of this method is to allow lateral flow assay developers to optimize capture conditions for the chosen sandwich antibodies, recreating exactly the same conditions as in the LFA device.

We immobilized two different HBVp-targeting antibodies on the surface of the chip, at a concentration of 1mg/mL. The chip was incubated in PBS prior to the sample run, and digital initial defocus scans were acquired. The first sample to be flowed was the HPV core protein (HBVp), at a concentration of 10μg/mL, for 10 minutes at 200μL/min, followed by PBS for five minutes, and finally the nanoparticle sample, constituted by aHBVp-functionalized 80nm GNPs. The binding curves for this sandwich assay are reported in Figure 4·16, while the digital pre- and post- images are reported in Figure 4·17.

Clearly, the HBVp target has a different kinetic behavior with respect to the nanoparticles. Diffusion and avidity affect binding of larger analytes, as discussed in Section 3.5.3. The signal drop measured when the nanoparticles reach the sample chamber can be attributed to the scattering from the free NPs solution, as well as accumulation of particles on the glass window that seals the sample cell. Both here and in Figure 4·14, the measured values are displayed as normalized signal, without converting to mass per unit area. The reason for this choice is consistency with the BEM simulated data, where the measured quantity is the signal from the particles divided by the reference signal. Moreover, since the measured signal can not be attributed to a uniform increase in thickness, the mass density approach would lack accuracy.

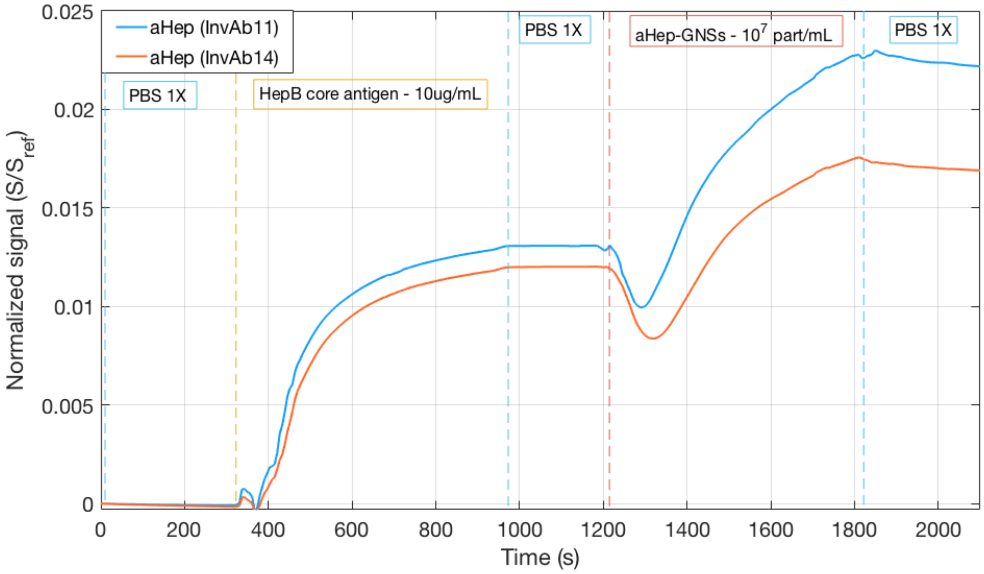

Figure 4·16: Sandwich assay for detection of hepatitis B core protein (HBVp) with gold-nanoparticle labeling. Two different surface probes were utilized, which target two different epitopes on the HPVp molecule.

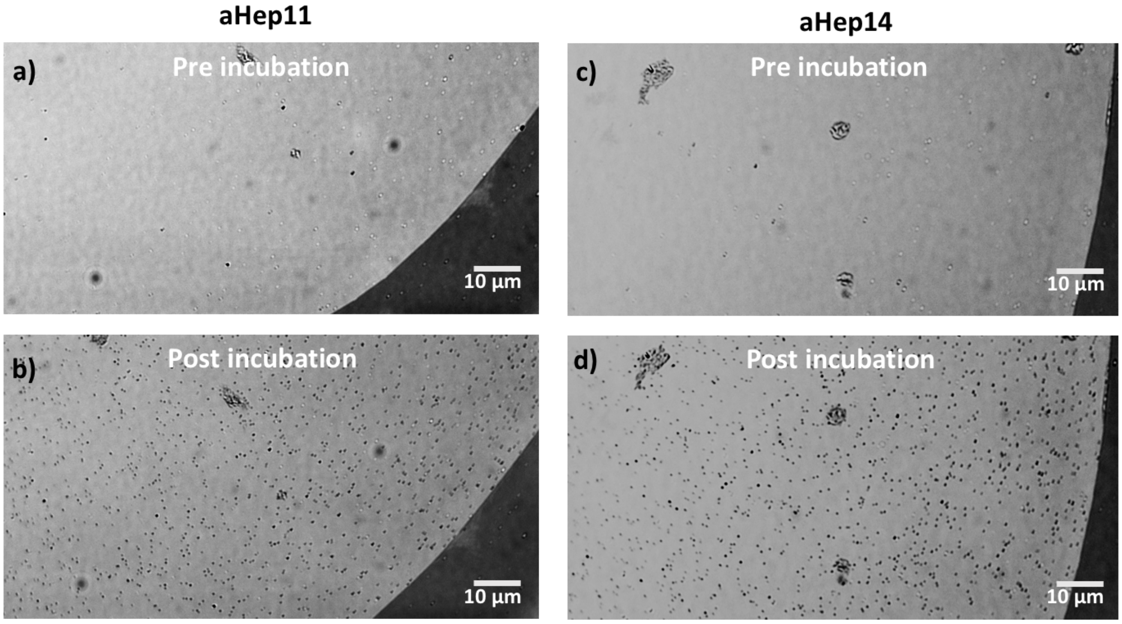

Figure 4·17: Pre (a-c) and post (b-d) images of 80nm aHBVp-GNS complexes bound to a HBV antigen-antibody sandwich.

4.3.3 Comparison with simulated data

In order to determine the feasibility of analog measurements of GNPs accumulation, we ran some simulations using the BEM software, a MATLAB tool that enables visualization of the scattering signal emitted by metallic nanoparticles under various conditions. The results of such simulations are presented in Section 3.2.3. Here, we would like to verify the consistency of those results with the analyzed experimental data.

We will start by comparing the measured analog signal from Figures 4·14 and 4·16 with the average low NA signal obtained when simulating a similar density of NPs on the surface. In order to determine which density of NPs corresponds to the largest measured analog signal, we have compared the acquired digital post-images with simulated digital images at different values of number of particles/mm^2, and we have determined that the situation that best represents the experimental data is when the simulated particle density is around $3{\times}10^4$ particles/mm^2, as represented in Figure 4·18.

To validate this hypothesis, we measured the average particle-to-particle distance on the acquired images on a cropped sample area on the digital image shown in Figure 4·17 of 1600μm^2. Particle-to-particle distance was measured by tracing 50 segments connecting the particles and calculating the average length. The average particle-to-particle distance was estimated to be 4.2$\pm$1.4μm. On the simulated image, for a particle density of $3{\times}10^4$ particles/mm^2, the average particle-to-particle distance is 4.9$\pm$1.8μm. An example of simulated image where the measured particle-to-particle distances have been labeled is shown in Figure 4·19.

Once determined what particle density is the most similar to that obtained experimentally, we then compared the average simulated signal from Figure 3·10. We calculated the normalized signal by dividing by the reference field, and the obtained

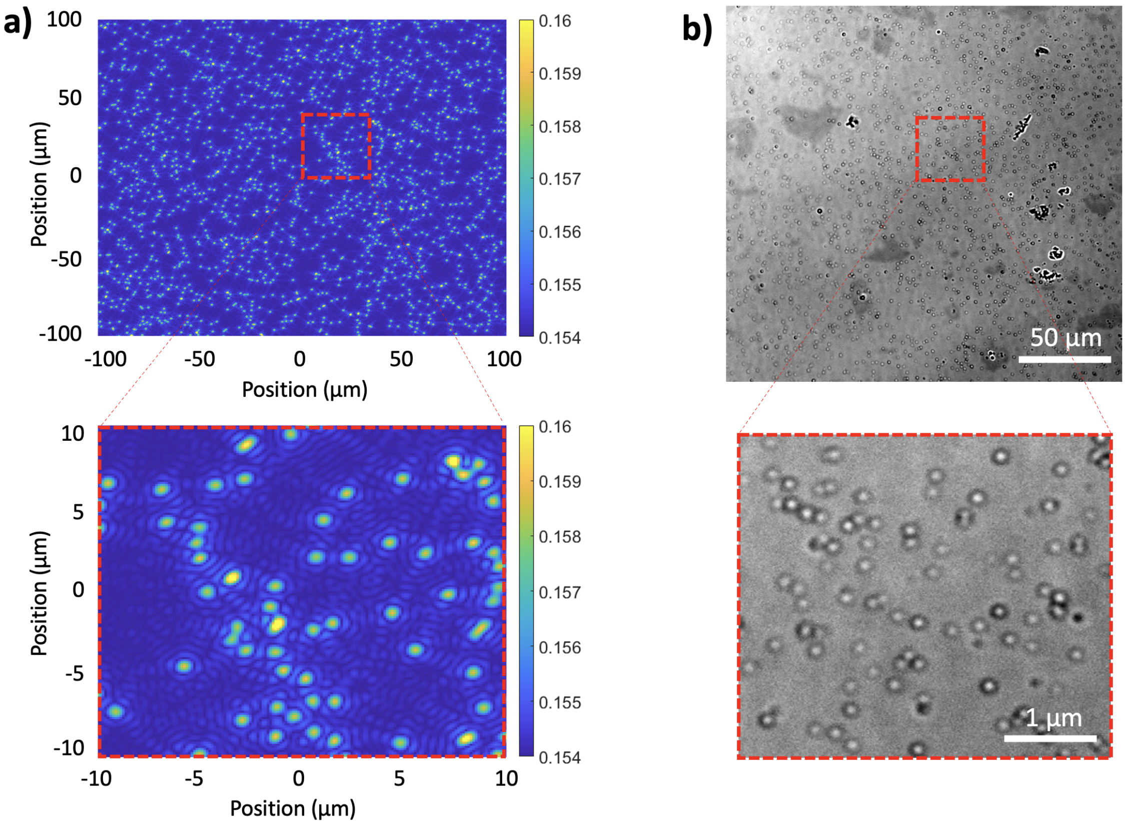

Figure 4·18: Comparison of a) simulated images at a particle density of 3×10^4 particles/mm^2 with b) the experimental data from Figure 4·17. The color axis indicates the total scattered signal ($S_{scat} + S_{ref}$). The two compared areas are identical.

mean value at 3×10^4 particles/mm^2 was around 2×10^{-4}. Experimentally, we obtained a higher measured value for the normalized signal ($\approx 5 \times 10^{-3}$) by calculating the difference from the equilibrium point reached by the antibody in Figure 4·16 (orange line).

The reason for this discrepancy between simulations and experimental data can depend on several factors. On the experimental side, for example, free protein in the sample can lead to an increase in mass density that can not be discriminated with respect to the scattering signal. On the simulations' side, when simulating a large number of particles we consider a 400μm^2 area surrounding the particle, but

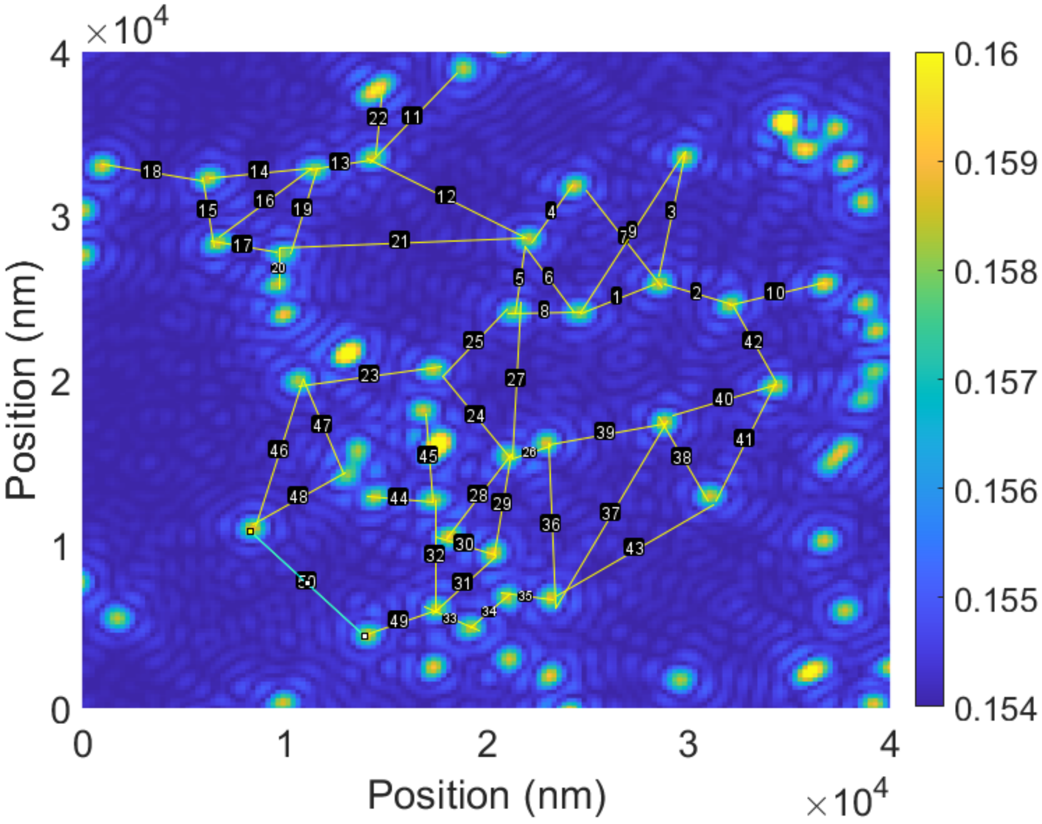

Figure 4·19: Simulated image at a particle density of 3×10^4 particles/mm^2, where the measured particle-to-particle distances have been labeled and numbered. The color axis indicates the total scattered signal ($S_{scat} + S_{ref}$).

the produced scattering field might extend further, leading to an underestimation of the simulated signal.

Nevertheless, this method is dramatically improving the sensitivity of the IRIS: in standard analog configuration, for antibody molecules to be detected, they need to form a continuous film on the surface. This signifies that the average distance between two captured antibody molecules needs to be less than 10nm, as antibodies can be modeled as a 7.5nm-diameter sphere (Williams et al., 2012). Here, the average distance between captured particles in the HBV sandwich assay is 4.2±1.4μm, three orders of magnitude larger, and an analog signal is still produced. Moreover, measurements at the single molecule level can be carried out, thanks to the possibility to switch to digital imaging. Thus, the increase in sensitivity achieved on the h-IRIS is key in order to establish the IRIS technology as breakthrough for diagnostic applications.

Chapter 5

Conclusions

5.1 Summary of the dissertation

The goal of this work was to introduce an improved version of the Interferometric Reflectance Imaging Sensor (IRIS), which has been optimized to perform the kinetic characterization of a wide range of analytes. The molecular weight of the analytes ranges from low molecular weight (*small*) molecules (MW<1kDa) to biological and synthetic nanoparticles (MW>1MDa). The IRIS platform has been developed in over a decade of research, and has been widely applied to kinetic characterization of proteins and oligonucleotides. In its digital - or single-particle counting - configuration, it has been shown to successfully perform counting and phenotyping of biological particles such as viruses and extracellular vesicles.

Here, the IRIS system has been further engineered by addressing a multidimensional optimization problem, where we considered each instrumental and experimental parameter and precisely tuned them in order to achieve the highest possible sensitivity, as well as the largest possible dynamic range in terms of analyte size. We combined simulations with the results of proof of concept experiments in order to generate an instrument that can virtually intake any target analyte and produce kinetic constants, as well as digital data down to the single molecule level.

After proving that the system is shot noise-limited, we optimized the level of averaging required to obtain small molecule sensitivity. We demonstrated the square root trend of the averaged number of electrons, and compared various camera sensors in order to select one that could combine high sensitivity, fast analog measurements with good resolution digital measurements. All optical parameters, including the illumination configuration and the numerical aperture of the objectives, have been analyzed and refined to allow for performing measurements in both configurations. Furthermore, simulations have been carried out in order to choose the proper thickness of the silicon oxide layer and illumination wavelength for analog measurements of biomass accumulation from large analytes.

Another crucial parameter for label-free measurements is surface chemistry, which has been shown to play a fundamental role in performing accurate kinetic measurements. After presenting the theory behind diffusion-limited measurements, a newly developed method is introduced which allows to study multiple surface chemistries at once on the same substrate thanks to localized polymer functionalization. As an additional advantage, this technique enables direct comparison of molecular probes that would generally not be allowed to be immobilized on the same chip, such as peptides and proteins.

For the first time, experimental results are presented for small molecule kinetic characterization on the IRIS, particularly biotin (MW = 243 Da) which has been studied as a proof of concept for determining the sensitivity of the system, and fumonisin toxin (MW = 721Da), as a demonstration of a relevant biotechnological application. Additionally, fumonisin has been successfully characterized across a multiplexed array of twenty antibodies, achieving the highest level of multiplexing ever demonstrated on the IRIS system.

Characterization of extracellular vesicles (EVs) is shown both at the analog and digital level, on two separate platforms - the standard analog and digital versions of the IRIS. On the other hand, antibody-conjugated gold nanoparticle samples (mAb-GNPs) have been characterized both at the analog and digital level on the same platform, the hybrid IRIS (h-IRIS) instrument, with minimal hardware adjustments to switch from one configuration to the other. We showed the consistency between simulated and experimental data for the analog and digital signal produced by GNPs, and we showed how using GNPs as a mass label for sandwich assays crucially increases the sensitivity of the IRIS system, improving the limit of detection by three orders of magnitude.

5.2 Future work

Additional optimization steps that would further improve the performances of the h-IRIS platform include: new integrating sphere designs that would improve illumination uniformity and reduce losses; the addition of an objective turret to allow for seamless transition between analog and digital detection; and multi-channel fluidic chamber designs that would increase the instrument throughput for drug development applications. The first two ideas are currently being implemented and tested, while the latter is still at the design stage.

For what concerns the software, we are working towards the development of an integrated software capable of handling both analog and digital acquisition, as we currently utilize custom-developed Python software that is distinct for each application. Automated particle tracking and counting is also under way.

One potential emerging application of the h-IRIS system could be the detection of even more complex biomarkers, such as metal-labeled biological nanoparticles (Draz et al., 2020). In this work, Draz et al. describe a method for labeling single viral particles with nm-sized platinum NPs. If a similar technique were to be applied to extracellular vesicles, for example, that would dramatically increase their refractive index and allow for analog detection of a much lower density of particles on the h-IRIS, improving the LOD. Digital imaging would then be performed, which - thanks to the increase in refractive index - could potentially be performed in liquid.

Overall, the h-IRIS is a highly versatile biosensing platform, that has been thoroughly optimized to achieve state-of-the-art performances on a wide dynamic range of targets. Further optimization could lead to a broader impact in the development of new, emerging biotechnological applications.

Appendix A

Supplementary material

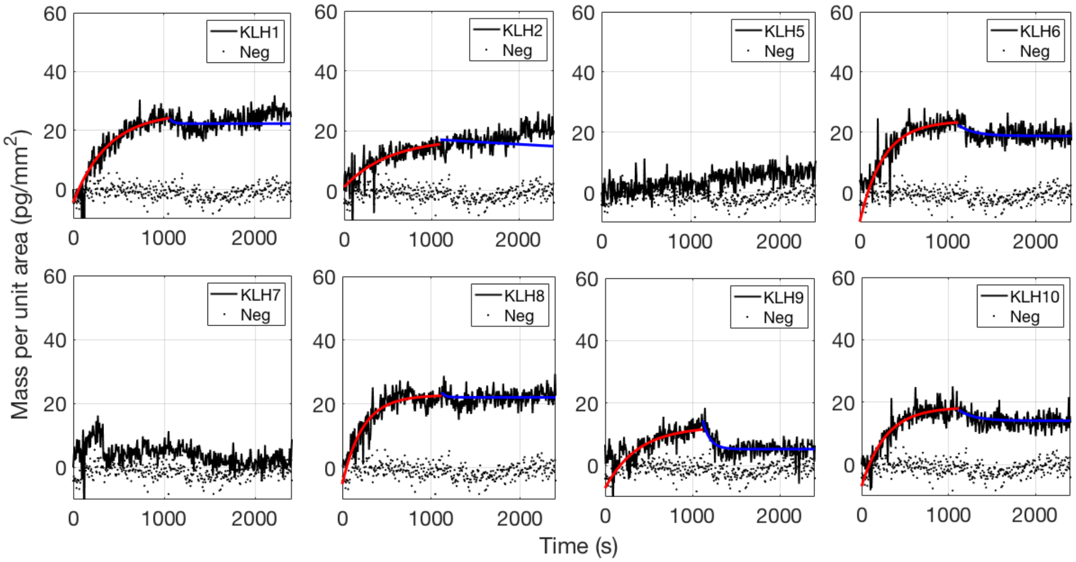

Figure A·1: Binding and debinding curves of the fumonisin toxin at a concentration of $100 \mu M$ to eight different antibodies generated by immunizing mice with Fumonisin B1 conjugated to Keyhole limpet hemocyanin (KLH); The solid red line indicates the 1:1 fitted association curve, while the solid blue line indicates the fitted dissociation curve. The dotted line represents the control spots' trend.

Table A.1: Association, dissociation and equilibrium constants calculated for eighteen antibodies against Fumonisin B1, as calculated with a simple 1:1 Langmuir model from the fitted curves of figures 4·3,A·1,A·2.

Antibody	$k_{on}(M^{-1}s^{-1})$	$k_{off}(10^{-4}s^{-1})$	$K_D(\mu M)$
CTx-1	15.6 ± 2.2	6.8 ± 3.2	44 ± 22
CTx-2	11.0 ± 2.2	8.8 ± 4.4	80 ± 43
CTx-3	13.1 ± 3.0	9.5 ± 4.3	73 ± 37
CTx-4	27.4 ± 4.6	15.9 ± 4.6	58 ± 19
CTx-5	30.8 ± 2.7	5.1 ± 1.9	17 ± 6
CTx-6	1.1 ± 0.2	53.7 ± 11.8	4986 ± 1461
CTx-7	12.5 ± 4.8	41.1 ± 18.7	329 ± 196
CTx-8	20.0 ± 2.1	5.3 ± 2.1	27 ± 11
CTx-9	31.0 ± 33.4	106 ± 118	341 ± 530
CTx-10	13.6 ± 2.7	3.9 ± 3.2	28 ± 24
KLH-1	8.2 ± 1.5	17.9 ± 4.7	219 ± 70
KLH-2	4.0 ± 0.7	15.2 ± 3.3	377 ± 103
KLH-3	9.3 ± 1.1	14.1 ± 3.0	151 ± 37
KLH-4	31.9 ± 5.7	21.5 ± 5.3	67 ± 22
KLH-5	N/A	N/A	N/A
KLH-6	6.6 ± 0.9	3.0 ± 27.6	46 ± 415
KLH-7	N/A	N/A	N/A
KLH-8	11.9 ± 2.2	31.6 ± 7.5	266 ± 81
KLH-9	10.0 ± 2.8	16.6 ± 7.2	166 ± 85
KLH-10	20.0 ± 3.5	16.1 ± 4.8	81 ± 28

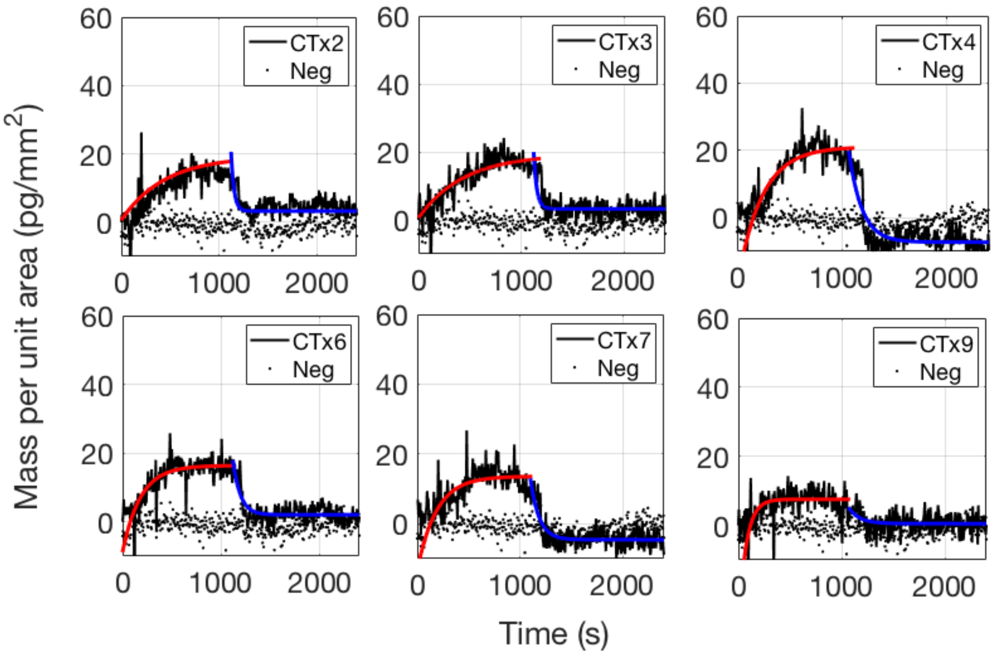

Figure A·2: Binding and debinding curves of the fumonisin toxin at a concentration of $100\mu M$ to seven different antibodies generated by immunizing mice with Fumonisin B1 conjugated to Cholera toxin B subunit (CTx-B); The solid red line indicates the 1:1 fitted association curve, while the solid blue line indicates the fitted dissociation curve. The dotted line represents the control spots' trend.

References

Avci, O., Campana, M. I., Yurdakul, C., and Ünlü, M. S. (2017). Pupil function engineering for enhanced nanoparticle visibility in wide-field interferometric microscopy. *Optica*, 4(2):247–254.

Bakhshpour, M., Chiodi, E., Celebi, I., Saylan, Y., Ünlü, N. L., Ünlü, M. S., and Denizli, A. (2022). Sensitive and real-time detection of igg using interferometric reflecting imaging sensor system. *Biosensors and Bioelectronics*, 201:113961.

Bakhshpour, M. and Denizli, A. (2020). Highly sensitive detection of cd(ii) ions using ion-imprinted surface plasmon resonance sensors. *Microchemical Journal*, 159:105572.

Brambilla, D., Sola, L., Ferretti, A. M., Chiodi, E., Zarovni, N., Fortunato, D., Criscuoli, M., Dolo, V., Giusti, I., Murdica, V., Kluszczyńska, K., Czernek, L., Düchler, M., Vago, R., and Chiari, M. (2021). Ev separation: Release of intact extracellular vesicles immunocaptured on magnetic particles. *Analytical Chemistry*, 93(13):5476–5483.

Camarca, A., Varriale, A., Capo, A., Pennacchio, A., Calabrese, A., Giannattasio, C., Murillo Almuzara, C., D'Auria, S., and Staiano, M. (2021). Emergent biosensing technologies based on fluorescence spectroscopy and surface plasmon resonance. *Sensors*, 21(3).

Cao, Y., Griffith, B., Bhomkar, P., Wishart, D. S., and McDermott, M. T. (2018). Functionalized gold nanoparticle-enhanced competitive assay for sensitive small-molecule metabolite detection using surface plasmon resonance. *Analyst*, 143:289–296.

Celebi, I., Geib, M. T., Chiodi, E., Lortlar Ünlü, N., Ekiz Kanik, F., and Ünlü, S. (2020). Instrument-free protein microarray fabrication for accurate affinity measurements. *Biosensors*, 10(11).

Chiodi, E., Daaboul, G. G., Marn, A. M., and Ünlü, M. S. (2021a). Multiplexed affinity measurements of extracellular vesicles binding kinetics. *Sensors*, 21(8).

Chiodi, E., Damin, F., Sola, L., Ferraro, L., Brambilla, D., Ünlü, M. S., and Chiari, M. (2021b). A reliable, label free quality control method for the production of dna microarrays with clinical applications. *Polymers*, 13(3).

Chiodi, E., Marn, A. M., Bakhshpour, M., Lortlar Ünlü, N., and Ünlü, M. S. (2022). The effects of three-dimensional ligand immobilization on kinetic measurements in biosensors. *Polymers*, 14(2).

Chiodi, E., Marn, A. M., Geib, M., Ekiz Kanik, F., Rejman, J., AnKrapp, D., and Unlu, M. (2020a). Highly multiplexed label-free imaging sensor for accurate quantification of small-molecule binding kinetics. *ACS Omega*, 5:25358–25364.

Chiodi, E., Marn, A. M., Geib, M. T., and Ünlü, M. S. (2021c). The role of surface chemistry in the efficacy of protein and dna microarrays for label-free detection: An overview. *Polymers*, 13(7).

Chiodi, E., Sola, L., Brambilla, D., Cretich, M., Marn, A. M., Ünlü, M. S., and Chiari, M. (2020b). Simultaneous evaluation of multiple microarray surface chemistries through real-time interferometric imaging. *Analytical and Bioanalytical Chemistry*, 412(14):3477–3487.

Chu, F. S. and Li, G. Y. (1994). Simultaneous occurrence of fumonisin b1 and other mycotoxins in moldy corn collected from the peoples republic of china in regions with high incidences of esophageal cancer. *Applied Environmental Microbiology*, 60(3):847–852.

Clerc, I., Sagar, A., Barducci, A., Sibille, N., Bernadó, P., and Cortés, J. (2021). The diversity of molecular interactions involving intrinsically disordered proteins: A molecular modeling perspective. *Computational and Structural Biotechnology Journal*, 19:3817–3828.

Cretich, M., Reddington, A., Monroe, M., Bagnati, M., Damin, F., Sola, L., Unlu, M. S., and Chiari, M. (2011). Silicon biochips for dual label-free and fluorescence detection: Application to protein microarray development. *Biosensors and Bioelectronics*, 26(9):3938–3943.

De Lean, A. and Rodbard, D. (1979). *Kinetics of Cooperative Binding*, pages 143–192. Springer US, Boston, MA.

Della Corte, F. G., Pangallo, G., Carotenuto, R., Iero, D., Marra, G., Merenda, M., and Rao, S. (2020). Temperature sensing characteristics and long term stability of power leds used for voltage vs. junction temperature measurements and related procedure. *IEEE Access*, 8:43057–43066.

Drake, A. W., Tang, M. L., Papalia, G. A., Landes, G., Haak-Frendscho, M., and Klakamp, S. L. (2012). Biacore surface matrix effects on the binding kinetics and affinity of an antigen/antibody complex. *Analytical Biochemistry*, 429(1):58–69.

Draz, M. S., Vasan, A., Muthupandian, A., Kanakasabapathy, M. K., Thirumalaraju, P., Sreeram, A., Krishnakumar, S., Yogesh, V., Lin, W., Yu, X. G., Chung, R. T., and Shafiee, H. (2020). Virus detection using nanoparticles and deep neural network–enabled smartphone system. *Science Advances*, 6(51):eabd5354.

Elber, R. (2005). Long-timescale simulation methods. *Current Opinion in Structural Biology*, 15(2):151–156. Theory and simulation/Macromolecular assemblages.

Epstein, J. R., Biran, I., and Walt, D. R. (2002). Fluorescence-based nucleic acid detection and microarrays. *Analytica Chimica Acta*, 469(1):3–36.

Eyal, S., Hsiao, P., and Unadkat, J. D. (2009). Drug interactions at the blood-brain barrier: Fact or fantasy? *Pharmacology and Therapeutics*, 123(1):80–104.

Faccio, G. (2018). From protein features to sensing surfaces. *Sensors*, 18(4).

Fechner, P., Bleher, O., Ewald, M., Freudenberger, K., Furin, D., Hilbig, U., Kolarov, F., Krieg, K., Leidner, L., Markovic, G., and et al. (2014). Size does matter! label-free detection of small molecule-protein interaction. *Analytical and Bioanalytical Chemistry*, 406(17):4033–4051.

Friedl, P., den Boer, A. T., and Gunzer, M. (2005). Tuning immune responses: diversity and adaptation of the immunological synapse. *Nature Reviews Immunology*, 5(7):532–545.

Gagni, P., Cretich, M., Benussi, L., Tonoli, E., Ciani, M., Ghidoni, R., Santini, B., Galbiati, E., Prosperi, D., and Chiari, M. (2016). Combined mass quantitation and phenotyping of intact extracellular vesicles by a microarray platform. *Analytica Chimica Acta*, 902:160–167.

General Electrics Company (2012). Biacore assay handbook. https://shared-resources.dhvi.duke.edu/sites/shared-resources.dhvi.duke.edu/files/Biacore

Granados-Chinchilla, F., Redondo-Solano, M., and Jaikel-Víquez, D. (2018). Mycotoxin contamination of beverages obtained from tropical crops. *Beverages*, 4(4).

Joubert, J., Dyk, S. V., and Malan, S. F. (2013). Small molecule fluorescent ligands as central nervous system imaging probes. *Mini Reviews in Medical Chemistry*, 13(5):682–696.

Kahlert, C. and Kalluri, R. (2013). Exosomes in tumor microenvironment influence cancer progression and metastasis. *Journal of Molecular Medicine*, 91(4):431–437.

Kairdolf, B. A., Qian, X., and Nie, S. (2017). Bioconjugated nanoparticles for biosensing, in vivo imaging, and medical diagnostics. *Analytical Chemistry*, 89(2):1015–1031.

Karanicolas, J. and Brooks, Charles L, r. (2004). Integrating folding kinetics and protein function: biphasic kinetics and dual binding specificity in a ww domain. *Proceedings of the National Academy of Sciences of the United States of America*, 101(10):3432–3437.

Karlsson, R. (2016). Biosensor binding data and its applicability to the determination of active concentration. *Biophysical Reviews*, 8(4):347–358.

Khranovskyy, V., Ekblad, T., Yakimova, R., and Hultman, L. (2012). Surface morphology effects on the light-controlled wettability of zno nanostructures. *Applied Surface Science*, 258:8146–8152.

Kim, D.-K., Kerman, K., Hiep, H. M., Saito, M., Yamamura, S., Takamura, Y., Kwon, Y.-S., and Tamiya, E. (2008). Label-free optical detection of aptamer–protein interactions using gold-capped oxide nanostructures. *Analytical Biochemistry*, 379(1):1–7.

Kurihara, K. and Suzuki, K. (2002). Theoretical understanding of an absorption-based surface plasmon resonance sensor based on kretchmann's theory. *Analytical Chemistry*, 74(3):696–701.

Li, M.-H., Choi, S. K., Leroueil, P. R., and Baker, J. R. (2014). Evaluating binding avidities of populations of heterogeneous multivalent ligand-functionalized nanoparticles. *ACS Nano*, 8(6):5600–5609. PMID: 24810868.

Li, S., Yang, M., Zhou, W., Johnston, T., Wang, R., and Zhu, J. (2015). Dextran hydrogel coated surface plasmon resonance imaging (spri) sensor for sensitive and label-free detection of small molecule drugs. *Applied Surface Science*, 355:570–576.

Liang, T. J. (2009). Hepatitis b: the virus and disease. *Hepatology (Baltimore, Md.)*, 49(5 Suppl):S13–S21.

Lin, L., Guo, J., Liu, H., and Jiang, X. (2021). Rapid detection of hepatitis b virus in blood samples using a combination of polymerase spiral reaction with nanoparticles lateral-flow biosensor. *Frontiers in Molecular Biosciences*, 7.

Lin, P.-C., Tseng, M.-C., Su, A.-K., Chen, Y.-J., and Lin, C.-C. (2007). Functionalized magnetic nanoparticles for small-molecule isolation, identification, and quantification. *Analytical Chemistry*, 79(9):3401–3408. PMID: 17402709.

Liu, Y., Zhan, L., Qin, Z., Sackrison, J., and Bischof, J. C. (2021). Ultrasensitive and highly specific lateral flow assays for point-of-care diagnosis. *ACS Nano*, 15(3):3593–3611. PMID: 33607867.

Lötvall, J., Hill, A. F., Hochberg, F., Buzás, E. I., Di Vizio, D., Gardiner, C., Gho, Y. S., Kurochkin, I. V., Mathivanan, S., Quesenberry, P., Sahoo, S., Tahara, H., Wauben, M. H., Witwer, K. W., and Théry, C. (2014). Minimal experimental requirements for definition of extracellular vesicles and their functions: a position statement from the international society for extracellular vesicles. *Journal of Extracellular Vesicles*, 3:26913–26913.

Loveday, S. M. (2016). Beta-lactoglobulin heat denaturation: A critical assessment of kinetic modelling. *International Dairy Journal*, 52:92–100.

Mallick, E. R., Arab, T., Huang, Y., Dong, L., Liao, Z., Zhao, Z., Smith, B., Haughey, N. J., Pienta, K. J., Slusher, B. S., Tarwater, P. M., Tosar, J. P., Zivkovic, A. M., Vreeland, W. N., Paulaitis, M. E., and Witwer, K. W. (2020). Characterization of extracellular vesicles and artificial nanoparticles with four orthogonal single-particle analysis platforms. *bioRxiv*.

Marn, A. M. (2021). Interferometric imaging for high sensitivity multiplexed molecular measurements. Doctoral dissertation, Boston University. https://open.bu.edu/handle/2144/43089.

Marn, A. M., Chiodi, E., and Ünlü, M. S. (2021a). Bulk-effect-free method for binding kinetic measurements enabling small-molecule affinity characterization. *ACS Omega*, 6(10):6836–6841.

Marn, A. M., Needham, J., Chiodi, E., and Ünlü, M. S. (2021b). Multiplexed, high-sensitivity measurements of antibody affinity using interferometric reflectance imaging sensor. *Biosensors*, 11(12).

Mizukami, S., Hori, Y., and Kikuchi, K. (2014). Small-molecule-based protein-labeling technology in live cell studies: Probe-design concepts and applications. *Accounts of Chemical Research*, 47(1):247–256. PMID: 23927788.

Mullard, A. (2020). 2019 fda drug approvals. *Nature Reviews in Drug Discovery*, 19:79–84.

Nawaz, M., Camussi, G., Valadi, H., Nazarenko, I., Ekström, K., Wang, X., Principe, S., Shah, N., Ashraf, N. M., Fatima, F., Neder, L., and Kislinger, T. (2014). The emerging role of extracellular vesicles as biomarkers for urogenital cancers. *Nature Reviews Urology*, 11(12):688–701.

Needham, J. W. (2019). Multiplexed antibody kinetics using the interferometric reflectance imaging sensor. Doctoral dissertation, Boston University. https://open.bu.edu/handle/2144/36604.

Nikolovska-Coleska, Z. (2015). Studying protein-protein interactions using surface plasmon resonance. *Methods in Molecular Biology*, 1278:109–138.

Nimse, S., Song, K., Sonawane, M., Sayyed, D., and Kim, T. (2014). Immobilization techniques for microarray: Challenges and applications. *Sensors*, 14(12):22208–22229.

Novotny, L. and Hecht, B. (2006). *Principles of Nano-Optics*. Cambridge University Press, Cambridge.

Peltomaa, R., Glahn-Martínez, B., Benito-Peña, E., and Moreno-Bondi, M. C. (2018). Optical biosensors for label-free detection of small molecules. *Sensors*, 18(12).

Pereiro, I., Tabnaoui, S., Fermigier, M., du Roure, O., Descroix, S., Viovy, J.-L., and Malaquin, L. (2017). Magnetic fluidized bed for solid phase extraction in microfluidic systems. *Lab on a Chip*, 17:1603–1615.

Peters, M. G. (2019). Hepatitis b virus infection: What is current and new. *Topics in antiviral medicine*, 26(4):112–116.

Petsko, G. A. and Yates, J. R. r. (2011). Analyzing molecular interactions. *Current Protocols in Bioinformatics*, Chapter 8:Unit 8.1.

Picciolini, S., Gualerzi, A., Vanna, R., Sguassero, A., Gramatica, F., Bedoni, M., Masserini, M., and Morasso, C. (2018). Detection and characterization of different brain-derived subpopulations of plasma exosomes by surface plasmon resonance imaging. *Analytical Chemistry*, 90(15):8873–8880.

Piehler, J., Brecht, A., and Gauglitz, G. (1996). Affinity detection of low molecular weight analytes. *Analytical Chemistry*, 68:139–143.

Pirri, G., Damin, F., Chiari, M., Bontempi, E., and Depero, L. E. (2004). Characterization of a polymeric adsorbed coating for dna microarray glass slides. *Analytical Chemistry*, 76(5):1352–1358. PMID: 14987092.

Pohanka, M. (2018). Overview of piezoelectric biosensors, immunosensors and dna sensors and their applications. *Materials*, 11(3):448.

Reth, M. (2013). Matching cellular dimensions with molecular sizes. *Nature Immunology*, 14(8):765–767.

Sandfeld-Paulsen, B., Aggerholm-Pedersen, N., Bæk, R., Jakobsen, K. R., Meldgaard, P., Folkersen, B. H., Rasmussen, T. R., Varming, K., Jørgensen, M. M., and Sorensen, B. S. (2016a). Exosomal proteins as prognostic biomarkers in non-small cell lung cancer. *Molecular Oncology*, 10(10):1595–1602.

Sandfeld-Paulsen, B., Jakobsen, K. R., Bæk, R., Folkersen, B. H., Rasmussen, T. R., Meldgaard, P., Varming, K., Jørgensen, M. M., and Sorensen, B. S. (2016b). Exosomal proteins as diagnostic biomarkers in lung cancer. *Journal of Thoracic Oncology*, 11(10):1701–1710.

Saylan, Y., Akgönüllü, S., Yavuz, H., Ünal, S., and Denizli, A. (2019). Molecularly imprinted polymer based sensors for medical applications. *Sensors*, 19(6).

Schasfoort, R. B. M. (2017). *Handbook of Surface Plasmon Resonance.* Royal Society of Chemistry (RSC).

Schuck, P. and Zhao, H. (2010). The role of mass transport limitation and surface heterogeneity in the biophysical characterization of macromolecular binding processes by spr biosensing. *Methods in molecular biology*, 627:15–54.

Seurynck-Servoss, S. L., White, A. M., Baird, C. L., Rodland, K. D., and Zangar, R. C. (2007). Evaluation of surface chemistries for antibody microarrays. *Analytical Biochemistry*, 371(1):105–115.

Sevenler, D. and Ünlü, M. S. (2016). Numerical techniques for high-throughput reflectance interference biosensing. *Journal of Modern Optics*, 63(11):1115–1120.

Sorensen, B. S., Wu, L., Wei, W., Tsai, J., Weber, B., Nexo, E., and Meldgaard, P. (2014). Monitoring of epidermal growth factor receptor tyrosine kinase inhibitor-sensitizing and resistance mutations in the plasma dna of patients with advanced non-small cell lung cancer during treatment with erlotinib. *Cancer*, 120(24):3896–3901.

Squires, T. M., Messinger, R. J., and Manalis, S. R. (2008). Making it stick: convection, reaction and diffusion in surface-based biosensors. *Nature Biotechnology*, 26(4):417–426.

Svitel, J., Balbo, A., Mariuzza, R. A., Gonzales, N. R., and Schuck, P. (2003). Combined affinity and rate constant distributions of ligand populations from experimental surface binding kinetics and equilibria. *Biophysical Journal*, 84(6):4062–4077.

Svitel, J., Boukari, H., Van Ryk, D., Willson, R. C., and Schuck, P. (2007). Probing the functional heterogeneity of surface binding sites by analysis of experimental binding traces and the effect of mass transport limitation. *Biophysical Journal*, 92(5):1742–1758.

Syahir, A., Usui, K., Tomizaki, K.-y., Kajikawa, K., and Mihara, H. (2015). Label and label-free detection techniques for protein microarrays. *Microarrays*, 4(2):228–244.

Sydenham, E. W., Thiel, P. G., Marasas, W. F. O., Shephard, G. S., Van Schalkwyk, D. J., and Koch, K. R. (1990). Natural occurrence of some fusarium mycotoxins in corn from low and high esophageal cancer prevalence areas of the transkei, southern africa. *Journal of Agricultural and Food Chemistry*, 38(10):1900–1903.

Tang, Y., Zeng, X., and Liang, J. (2010). Surface plasmon resonance: An introduction to a surface spectroscopy technique. *Journal of Chemical Education*, 87(7):742–746.

Tokuhara, T., Hasegawa, H., Hattori, N., Ishida, H., Taki, T., Tachibana, S., Sasaki, S., and Miyake, M. (2001). Clinical significance of cd151 gene expression in non-small cell lung cancer. *Clinical Cancer Research*, 7(12):4109–4114.

Trilling, A. K., Harmsen, M. M., Ruigrok, V. J. B., Zuilhof, H., and Beekwilder, J. (2013). The effect of uniform capture molecule orientation on biosensor sensitivity: dependence on analyte properties. *Biosensors and Bioelectronics*, 40(1):219–226.

Tsougeni, K., Ellinas, K., Koukouvinos, G., Petrou, P. S., Tserepi, A., Kakabakos, S. E., and Gogolides, E. (2018). Three-dimensional (3d) plasma micro-nanotextured slides for high performance biomolecule microarrays: Comparison with epoxy-silane coated glass slides. *Colloids and Surfaces B: Biointerfaces*, 165:270 – 277.

van de Hulst, H. (1958). Light scattering by small particles. *Quarterly Journal of the Royal Meteorological Society*, 84(360):198–199.

Wang, S., Khan, A., Huang, R., Ye, S., Di, K., Xiong, T., and Li, Z. (2020). Recent advances in single extracellular vesicle detection methods. *Biosensors and Bioelectronics*, 154:112056.

Williams, E. H., Davydov, A. V., Motayed, A., Sundaresan, S. G., Bocchini, P., Richter, L. J., Stan, G., Steffens, K., Zangmeister, R., Schreifels, J. A., and et al. (2012). Immobilization of streptavidin on 4h–sic for biosensor development. *Applied Surface Science*, 258(16):6056–6063.

Wishart, D., Arndt, D., Pon, A., Sajed, T., Guo, A. C., Djoumbou, Y., Knox, C., Wilson, M., Liang, Y., Grant, J., Liu, Y., Goldansaz, S. A., and Rappaport, S. M. (2015). T3db: the toxic exposome database. *Nucleic Acids Research*, 43(Database issue):D928–34.

Wong, A., Ye, M., Levy, A., Rothstein, J., Bergles, D., and Searson, P. (2013). The blood-brain barrier: an engineering perspective. *Frontiers in Neuroengineering*, 6:7.

Wong, J., Chilkoti, A., and Moy, V. T. (1999). Direct force measurements of the streptavidin–biotin interaction. *Biomolecular Engineering*, 16(1):45 – 55.

Wu, S., Wu, L., Ho, H., and Lin, C. (2003). A differential measurement approach for improving surface plasmon resonance phase sensing performance. In *Proceedings of the Sixth Chinese Optoelectronics Symposium*, pages 128–131.

Yalçın, A., Damin, F., Özkumur, E., di Carlo, G., Goldberg, B. B., Chiari, M., and Ünlü, M. S. (2009). Direct observation of conformation of a polymeric coating with implications in microarray applications. *Analytical Chemistry*, 81(2):625–630.

Yurdakul, C. (2021). Interferometric reflectance microscopy for physical and chemical characterization of biological nanoparticles. Doctoral dissertation, Boston University. https://open.bu.edu/handle/2144/43096.

Zhang, F., Jing, W., Hunt, A., Yu, H., Yang, Y., Wang, S., Chen, H.-Y., and Tao, N. (2018). Label-free quantification of small-molecule binding to membrane proteins on single cells by tracking nanometer-scale cellular membrane deformation. *ACS Nano*, 12(2):2056–2064.

Curriculum Vitae

[redacted]

[redacted]

[redacted]

[redacted]

[redacted]